Experimental Investigation of the Trigger Problem in Magnetic Reconnection

by

Noam Karasov Katz

A.B., Princeton University (2004)

Submitted to the Department of Physics
in partial fulfillment of the requirements for the degree of

Doctor of Philosophy

at the

MASSACHUSETTS INSTITUTE OF TECHNOLOGY

June 2010

Author . . . .
Department of Physics
May 14, 2010

Certified by . . . .
Jan Egedal
Assistant Professor
Thesis Supervisor

Accepted by . . . .
Krishna Rajagopal
Professor of Physics
Associate Department Head for Education

Experimental Investigation of the Trigger Problem in Magnetic Reconnection

by

Noam Karasov Katz

Submitted to the Department of Physics
on May 14, 2010, in partial fulfillment of the
requirements for the degree of
Doctor of Philosophy

Abstract

Magnetic reconnection is a fundamental process in plasma physics, which involves the often explosive release of magnetically stored energy in both space and laboratory plasmas. In order for this sudden release of energy to occur, there must be a period of slow reconnection, in which magnetic stress accumulates in the system, followed by a quick transition to fast reconnection. The question of what causes this transition is known as the 'trigger problem' and is not well understood.

We address the trigger problem using the Versatile Toroidal Facility (VTF) at MIT, which we operate in the strong magnetic guide field regime. The resulting reconnection occurs in spontaneous events, in which there is a transition to fast reconnection. The reconnection in these events is asymmetric: it begins at one toroidal location and propagates toroidally in both directions. The spontaneous onset is facilitated by an interaction between the x-line current channel and a global mode, which breaks axisymmetry. We model the onset using an empirical Ohm's law and current continuity, which is maintained by ion polarization currents associated with the mode. The model reproduces the exponential growth of the reconnection electric field, and the model growth rate agrees well with the experimentally measured growth rate.

We begin, however, by discussing reconnection in the collisional regime and the effect of neutral gas on plasma flows. We perform experiments which are relevant to plasmas at the edge of tokamaks, but may also be applicable to reconnection in the solar photosphere and the interstellar medium, where the ionization fraction is low. In these experiments, a plasma filament propagates across a magnetic field in a background of neutral atoms. The filament motion is driven by charge separation in an inhomogeneous magnetic field, and this drive is balanced by collisional damping. The filament propagation and internal structure are described in detail.

Thesis Supervisor: Jan Egedal
Title: Assistant Professor

Acknowledgments

I am very grateful to my thesis advisor, Prof. Jan Egedal, for taking me on as a graduate student, and for his guidance and support over the years. I really admire Jan's keen physical insight and I could not have asked for a better advisor. MIT, you'd better give him tenure.

Thanks also to Prof. Miklos Porkolab and Dr. Richard Temkin for serving on my thesis committee, and for their detailed and helpful feedback. In addition, thanks to Miklos for his valuable involvement in the VTF experiment during my first few years as a graduate student.

I am grateful to the VTF group, especially to Will Fox for his eagerness to discuss science and his willingness to share his thoughts and insights regarding plasma physics and experimental methods. Thanks also to Ari Le and Arturs Vrublevskis for physics discussions, and collaboration. Thanks to Jeff Bonde for his tireless work at building some of the probe arrays used in this thesis. Specific thanks to Will for the initial code for spherical ABR probe theory, to Ari for reading portions of this thesis, and to Arturs for the data on neutral resistivity (Fig. 4-3). Being a member of the VTF group made graduate school much more enjoyable.

Thanks to the engineering staff at the Plasma Science and Fusion Center, especially Tommy Toland and Rick Lations.

This work was partly funded by a Graduate Fellowship in Fusion Energy Sciences, through the Department of Energy. I am grateful to Walter Gekelman and Pat Pribyl at UCLA for their hospitality during the summer practicum that was part of this fellowship.

Thanks also to Hantao Ji for the opportunity to work at the Princeton Plasma Physics Lab as an undergraduate, an exciting experience which solidified my interest in experimental plasma physics.

Finally, I am very grateful to my family: Jon, Sally, Eli, and Jenny, and to Ariel for their love and support. I love you all. In addition, thank you to my grandparents who encouraged my intellectual pursuits throughout my life.

תודה למשפחתי היקרה, להורי סלי ויונתן, לאחי אלי ולאחותי ג׳ני שחוו איתי את המעבר למדינה חדשה ותמכו בי לאורך שנות הלימודים הרבות. אני אוהב אתכם.

And, lastly, thank you to the Eyjafjallajökull volcano for only causing a minor delay in my defense date.

Contents

List of Figures

List of Tables

Chapter 1

Introduction

1.1 The Prevalence of Magnetic Reconnection

Magnetic reconnection [1] is the often explosive release of magnetically stored energy in the presence of a plasma. This phenomenon, which involves a change in magnetic field topology, is thought to occur for example in solar flares [2], magnetospheric substorms [3], and tokamak sawteeth [4].

In solar flares, a sudden brightening of plasma on the sun signifies the energy release of as much as 10^{32} ergs (=10^{25} J) [5]. The only feasible source for the energy is the magnetic field associated with the flaring structures; the annihilation of these fields causes plasma heating and large-scale flows associated with coronal mass ejections [6] (see Fig. 1-1(b)). There are two phases used to describe solar flares [7]. During the *preflare phase*, a flux tube of plasma known as a prominence, rises slowly above active regions, which are bright areas surrounding sunspots. This rising structure stretches the magnetic field lines, which surround the prominence and tether it to the photosphere (see Fig. 1-1(a)). At the flare onset, the tension in the magnetic fields is released as the field lines break and reconnect. This process accelerates during the *main phase* and the magnetic energy released is observed in loops of hot, x-ray emitting plasma and at the prominence foot points, where Hα luminosity increases.

Magnetic reconnection is also important in the interaction of the solar wind with the Earth's magnetic field, and it allows the solar wind plasma to enter Earth's

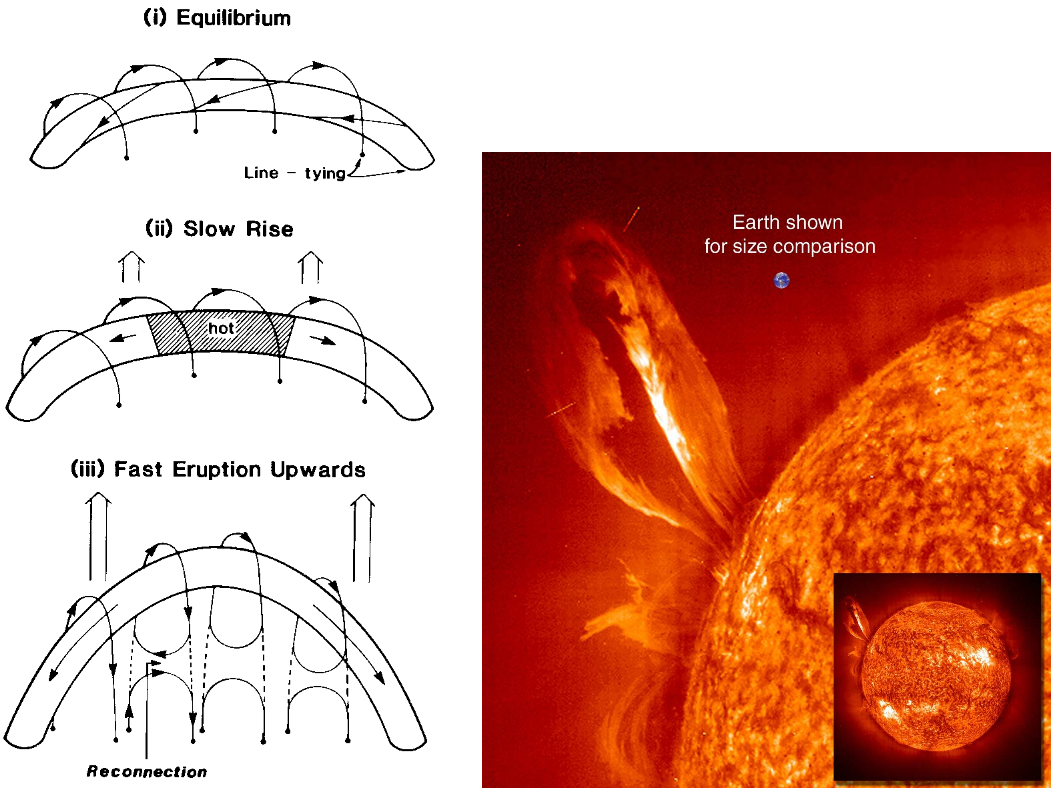

(a) (b)

Figure 1-1: (a) Solar flare cartoon showing the role of magnetic reconnection. Reproduced from Ref. [7]. (b) Eruptive solar prominence in He II from 24 July 1999, with an image of the Earth added for scale. Courtesy of SOHO/EIT consortium. SOHO is a project of international cooperation between ESA and NASA.

magnetosphere. The role of magnetic reconnection in magnetospheric flow patterns was first discussed by Dungey [1], as shown in Fig. 1-2. In the figure, a southward-oriented interplanetary magnetic field (IMF) reconnects with the dipole field of the Earth and is dragged by the solar wind to produce the polar cap flow patterns, whose observation motivated Dungey's idea. A second reconnection occurs in the magnetotail—the drawn-out magnetic field behind the Earth—as indicated by the field lines marked by 6 and 6' in the figure. The field lines proceed through stages marked by 6 to 9, corresponding to a sunward flow at lower latitudes. Although Dungey's idea is fundamental to the subsequent work on magnetospheric dynamics, Fig. 1-2 is oversimplified [7]. Complications include the strong time-dependence of the flow patterns, and the variation in IMF orientation.

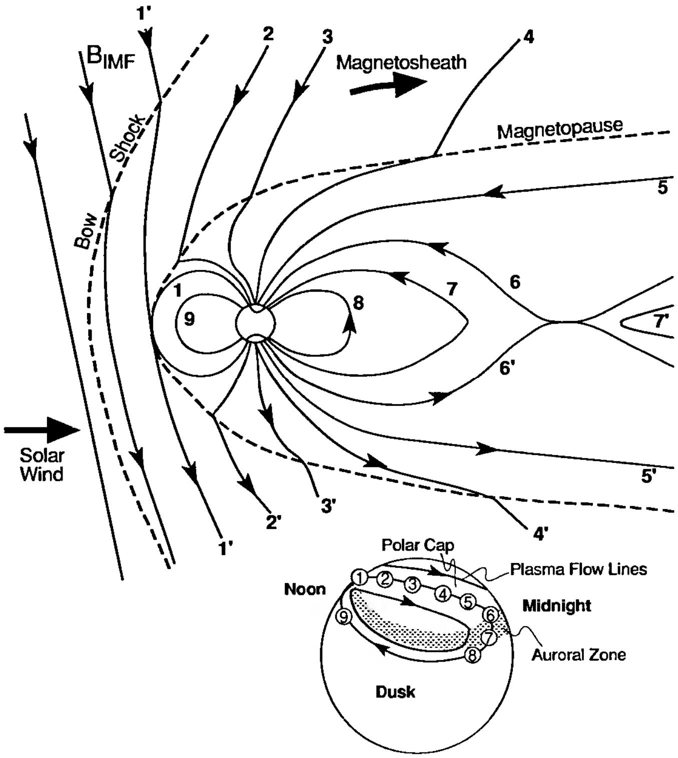

Figure 1-2: Dungey's proposed explanation for the observed plasma flow in the magnetosphere. The interplanetary magnetic field (here pointing southward) marked by 1' reconnects with the magnetospheric field line marked by 1. Successive numbers show the field being dragged across the Earth by the solar wind, only to undergo further reconnection as shown by the field lines marked by 6 and 6'. The corresponding flow pattern, which is stationary in the frame of the sun, is shown below. Reproduced from Ref. [7].

In the Earth's magnetosphere, magnetic reconnection is highly dynamic, giving rise to magnetospheric substorms [8, 5]. During these events, the IMF turns southward and day-side reconnection sends extra magnetic flux towards the magnetotail, stretching the tail out. During this expansion phase, the tail current increases and kinetic energy from the solar wind is converted through reconnection into stored magnetic energy. At substorm onset, the tail current reaches a critical threshold and decreases suddenly, releasing the stored magnetic energy. This energy is converted into flow energy, as a tail plasmoid is ejected, and into particle heating. Fast electrons stream along field lines towards the Earth's pole, producing the aurora by exciting neutral atoms in the ionosphere. During the recovery phase, the magnetotail shortens again, reflecting the reduced magnetic stress.

Magnetic reconnection in space plasmas is diagnosed either by optical based methods, for reconnection on the sun [9, 10, 11], or by in-situ satellite measurements, for reconnection in the Earth's magnetosphere [12, 13, 14, 15] and the solar wind [16]. Optical observations suffer from a limited resolution, while satellites provide localized point measurements and cannot capture the global reconnection dynamics. In laboratory experiments, it is possible in theory to observe both the global reconnection dynamics and the detailed local plasma behavior.

An important laboratory manifestation of magnetic reconnection is the sawtooth instability in tokamak plasmas. Von Goeler *et al.* [4] first characterized the sawtooth using x-ray fluctuations, observing that the core plasma temperature slowly increases and sharply decreases in a repeating cycle (see Fig. 1-3(a)). Farther out from the core, the opposite behavior occurs and the temperature suddenly increases as the core energy is released. The sawtooth instability is internal to the plasma, but in some cases reconnection can lead to major disruptions, in which complete loss of confinement occurs [5].

A schematic of the model proposed by Kadomtsev [17] to explain the sawtooth instability is shown in Fig. 1-3(b). In, Kadomtsev's model, as the core is externally heated, magnetic reconnection forms a cold island, which then grows and replaces the hot core. More specifically, ohmic heating reduces the Spitzer resistivity in the core.

Assuming a steady toroidal electric field, the toroidal current density, and hence the poloidal magnetic field, must increase as well. Inside the $q = 1$ region—where field lines close on themselves in one toroidal circuit—an internal kink mode expels the plasma, and the cycle repeats [5]. Kadomtsev's model is useful to frame the sawtooth problem, but it is incorrect. The poloidal magnetic field does not change as much as the model predicts, and the resistivity during the sawtooth is not given by Spitzer resistivity. These factors contribute to a faster observed rate of reconnection than predicted by Kadomtsev [5].

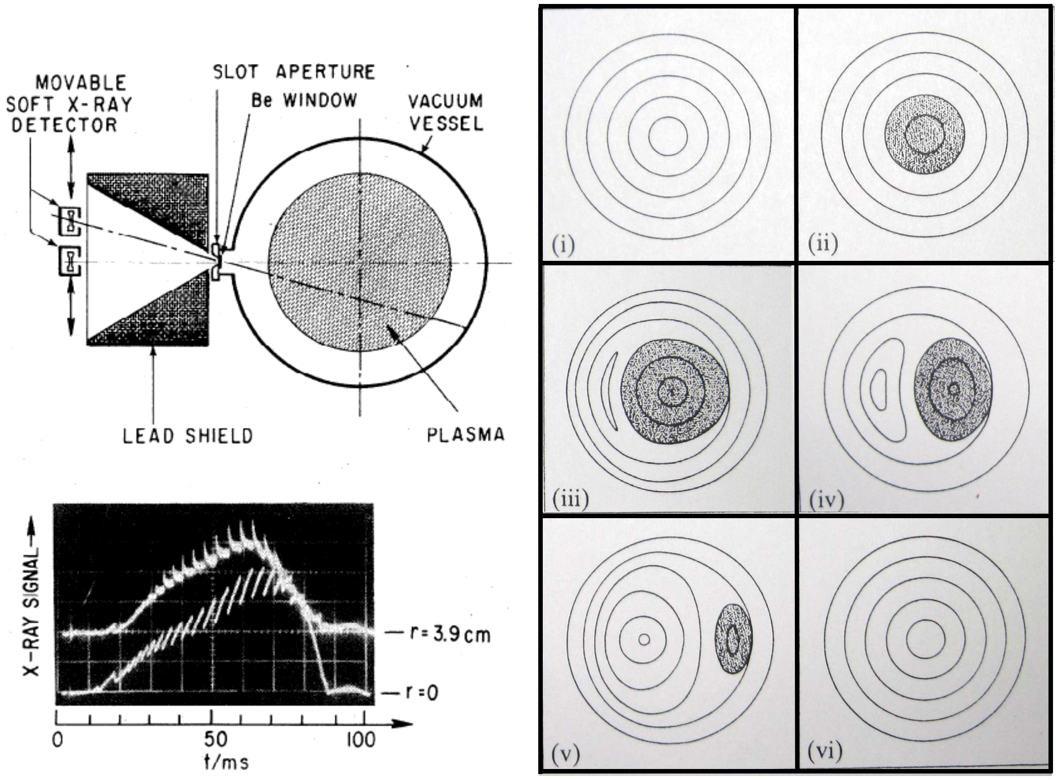

(a) (b)

Figure 1-3: (a) Detection of sawtooth oscillations in core (r=0) and inverted farther out (r=3.9 cm). Reproduced from Ref. [4]. (b) Kadomtsev's mechanism for the tokamak sawtooth, shown with poloidal flux surfaces: (i-ii) heating raises core temperature (shaded region) of nested flux surfaces; (iii-iv) reconnection forms cold magnetic island, which grows to become new cold core (v-vi). Adapted from Ref. [18].

Other laboratory experiments in which magnetic reconnection is observed include reversed-field pinch experiments [19], colliding high-energy-density laser-produced plasmas [20], and spheromak plasmas, where reconnection it is essential for the spheromak formation [21]. Other astrophysical examples in which reconnection is thought to occur include magnetars [22], and disconnection events in tail plasmas of comets [23]

1.2 Magnetic Reconnection Concepts

Magnetic reconnection involves not only an explosive release of magnetically stored energy, but also a change in magnetic field topology in the presence of a plasma. The prevalence of reconnection in space plasmas is at first surprising, since the high conductivity of these plasmas prevents topological changes to the magnetic field. This observation is based on the ideal (infinite conductivity) Ohm's law, which is given by

$$\mathbf{E} + \mathbf{v} \times \mathbf{B} = 0. \tag{1.1}$$

In combination with Faraday's law,

$$\frac{\partial \mathbf{B}}{\partial t} = -\nabla \times \mathbf{E}, \tag{1.2}$$

we arrive at

$$\frac{\partial \mathbf{B}}{\partial t} = \nabla \times (\mathbf{v} \times \mathbf{B}). \tag{1.3}$$

Alfvén's theorem (e.g. Ref. [24], p. 341) states that for a plasma described by Eq. 1.3, the flux through any closed loop ($\mathcal{S}$) moving with the plasma is constant in time:

$$\frac{d}{dt} \int_{\mathcal{S}} \mathbf{B} \cdot d\mathbf{a} = 0. \tag{1.4}$$

This is also referred to as "flux freezing", and it results in the magnetic field topology being fixed. From Eq. 1.1 it follows that $E_{\parallel} = \mathbf{E} \cdot \mathbf{B}/B = 0$. In order for magnetic reconnection to occur, there must be a non-zero parallel electric field, and Eq. 1.1 cannot hold everywhere.

The simplest non-ideal behavior can be introduced via finite resistivity η, yielding

$$\mathbf{E} + \mathbf{v} \times \mathbf{B} = \eta \mathbf{J}. \tag{1.5}$$

In combination with Faraday's law (Eq. 1.2), we arrive at

$$\frac{\partial \mathbf{B}}{\partial t} = \nabla \times (\mathbf{v} \times \mathbf{B}) + \frac{\eta}{\mu_0} \nabla^2 \mathbf{B}. \tag{1.6}$$

If the scale of variation of magnetic field is small enough, the last term will dominate over the middle convective term and the magnetic field will undergo diffusive decay. Such variation is typically found near current sheets, and the resistive timescale τ_{R} for magnetic field lines to convect into the layer will be given by $\tau_{\mathrm{R}} \sim \mu_0 L^2/\eta$, where L is the macroscopic size of the current sheet.

1.2.1 Sweet-Parker Reconnection

A faster rate of magnetic field annihilation was found by Peter Sweet and Eugene Parker [25, 26] in 1958. Their mechanism is shown schematically in Fig. 1-4. They assume 2D, steady-state, resistive magnetohydrodynamics (MHD), where the plasma is only non-ideal at the current sheet, marked by $2\delta \times 2L$ in the figure. The magnetic field is purely in the x-y plane, and is oppositely oriented above and below the current channel (gray region). The field is convected at velocity vv_{in} into the current sheet, where reconnection occurs, and then the field convects out the sides at v_{out}. The field line above and the field line below become connected in the outflow region. This is the topological change referred to previously, and it allows the solar wind plasma, for example, to enter the Earth's magnetosphere along field lines. The basic x-like geometry of Fig. 1-4 forms the basis of much work on magnetic reconnection. At the middle of the current sheet, there is the x-line, which extends into the page, and where the in-plane magnetic field vanishes.

To find the time-scale associated with Sweet-Parker reconnection, we start by

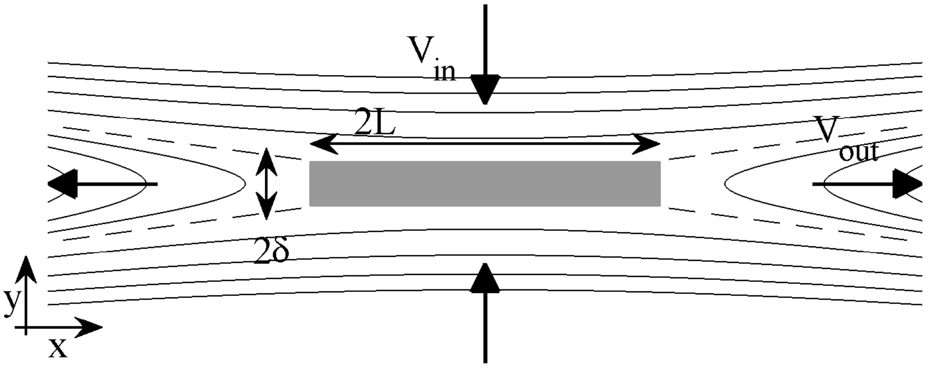

Figure 1-4: Sweet-Parker reconnection geometry. Dashed line represents separatrix, which separates the inflow and outflow regions. In the central diffusion region (gray), the reconnection electric field is balanced by the resistive term in Ohm's law.

requiring pressure balance across the layer, namely

$$\frac{B_{\text{in}}^2}{2\mu_0} + p_{\text{in}} + \frac{m_i n v_{\text{in}}^2}{2} = \frac{B_{\text{out}}^2}{2\mu_0} + p_{\text{out}} + \frac{m_i n v_{\text{out}}^2}{2}. \tag{1.7}$$

If we assume that the plasma $\beta = 2\mu_0/B^2$ is small, that the inflow speed is small relative to the Alfvén speed, and that all the magnetic energy from the inflow gets annihilated and converted to kinetic energy, we have

$$\frac{B_{\text{in}}^2}{2\mu_0} = \frac{m_i n v_{\text{out}}^2}{2} \rightarrow v_{\text{out}} = v_A \tag{1.8}$$

where $v_A = B/\sqrt{\mu_0 m_i n}$ is the Alfvén speed computed with the inflow magnetic field just above the current channel. Next we distinguish between the current channel, where B is negligible and

$$E_z = \eta J, \tag{1.9}$$

and the inflow, where the current is negligible and the plasma is ideal:

$$v_{\text{in}} = E_z/B_{\text{in}}. \tag{1.10}$$

Eliminating the reconnection electric field E_z, we find $v_{\text{in}} = \eta J/B_{\text{in}}$. Meanwhile, applying Ampère's law to the current channel gives $4LB_{\text{in}} = (2L)(2\delta)\mu_0 J$, so $v_{\text{in}} =$

$\eta/(\mu_0\delta)$. v_{in} can also be found from mass conservation,

$$v_{\text{in}} L = v_{\text{out}}\delta, \tag{1.11}$$

and using these two equations for v_{in} to eliminate δ, we find

$$v_{\text{in}} = \sqrt{\frac{\eta}{\mu_0 v_A L}} v_A = v_A/\sqrt{S}, \tag{1.12}$$

where the Lundquist number is defined as $S \equiv \mu_0 v_A L/\eta$. The Lundquist number represents the ratio of the convective term in Eq. 1.6 to the resistive term, with the characteristic velocity given by the Alfvén speed. The Sweet-Parker time-scale for reconnection is then $\tau_{\text{SP}} \sim L/v_{\text{in}} \sim \sqrt{S}L/v_A$. Recall that the resistive time-scale is $\tau_{\text{R}} \sim \mu_0 L^2/\eta \sim SL/v_A$. For a highly conductive plasma, $S \gg 1$, and the Sweet-Parker time-scale is much shorter than the resistive time-scale. Nevertheless, Sweet-Parker theory fails to reproduce the short time-scales associated with actual reconnection observations. For example, in the solar corona, we take $L \sim 10^7$ m, $v_A \sim 10^6$ m/s, and $T \sim 100$ eV [7, 5], so $\eta \sim m_e/(2ne^2\tau_{\text{ei}}) \sim 10^{-6}$ Ωm, where τ_{ei} is the electron-ion collision time [27]. Then $S \sim 10^{13}$, and $\tau_{\text{SP}} \sim 10$ months. In comparison, solar flares release stored magnetic energy in time-scales of the order of 100 s. Sweet-Parker reconnection is therefore too slow to describe solar flares.

1.2.2 Hall Reconnection

Fast reconnection—fast enough to account for observations—is possible, however, if extra terms in Ohm's law are taken into account. Ohm's law, which is based on the electron momentum equation, is then given by

$$\mathbf{E} + \mathbf{v} \times \mathbf{B} = \eta\mathbf{J} + \frac{\mathbf{J} \times \mathbf{B}}{ne} - \frac{\nabla \cdot \mathbf{P}_e}{ne} \tag{1.13}$$

where the electron inertia is still neglected. The inclusion of the new terms, the hall term and the pressure term, introduces a new scale length, the ion inertial length $d_i = c/\omega_{pi}$. For example, taking the ratio of the $\mathbf{J} \times \mathbf{B}$ term to the $\mathbf{v} \times \mathbf{B}$ term gives

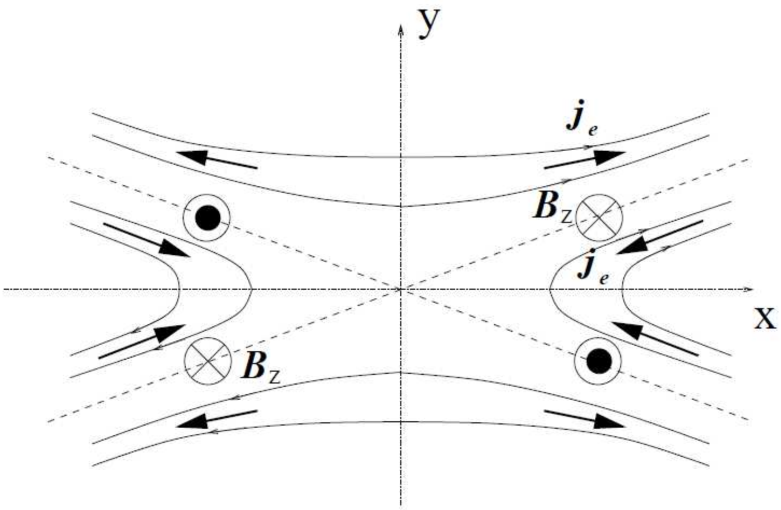

Figure 1-5: Hall reconnection: ions and electrons decouple on scales below the ion inertial length. The resulting electron current gives out-of-plane quadrupolar magnetic field. From Ref. [30].

$B^2/(\mu_0 neL)/(v_A B) \sim \sqrt{\mu_0 m_i n}/(neL) \sim c\sqrt{\epsilon_0 m_i/(ne^2)}/L \sim d_i/L$. When the current sheet size is on the order of the ion inertial length, the ions become unmagnetized, and the outflow region opens up to allow faster plasma flow through the central region [28, 29]. Since the electrons are still magnetized on this scale, they must flow along field lines (see Fig. 1-5) in order to catch up to the ions and preserve quasineutrality. This electron motion gives in-plane hall currents, and, as a result, a quadrupolar out-of-plane magnetic field. The quadrupolar magnetic field is a signature of hall reconnection, and it has been observed in simulations [31], the magnetopause [32], and laboratory experiments [33, 34].

The importance of the hall term in Ohm's law was revealed through a comparison of multiple simulation codes, including a fully kinetic particle-in-cell (PIC) code, a hall MHD code, and a resistive MHD code. All codes except the resistive MHD simulation included the physics of the hall effect. This multi-code comparison is known as the Geospace Environmental Modeling (GEM) Reconnection Challenge, and its goal was to identify the essential physics necessary to model collisionless reconnection [35]. The different codes all started with an initial Harris equilibrium in which $B_x(z) = B_0 \tanh(z/\lambda)$ and the results showed that all models which include

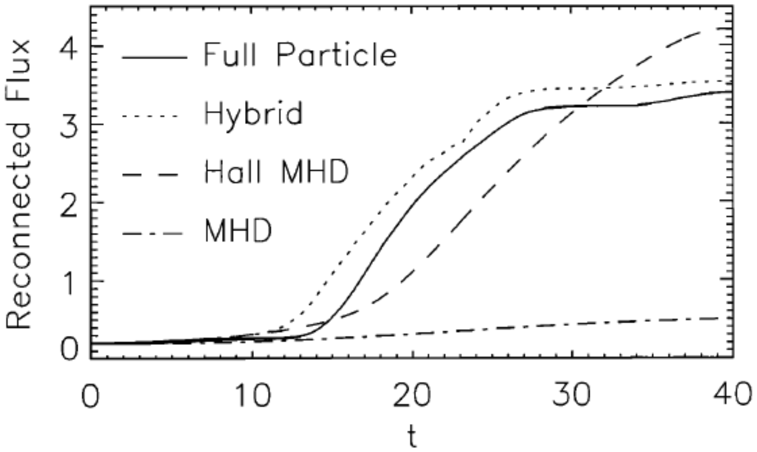

Figure 1-6: GEM Reconnection Challenge: the reconnected magnetic flux versus time for a variety of simulation codes. The reconnection rate is fast ($\sim v_A/10$) for all models which include the hall effect. Reproduced from Ref. [35].

the hall effect had a universal reconnection rate on the order of $v_{\rm in} \sim v_A/10$. Here the inflow velocity is taken as a measure of the reconnection rate, and the Alfvén velocity is computed with the upstream value of the magnetic field B_0. The results are summarized in Fig. 1-6.

1.2.3 Magnetic Reconnection with a Guide Magnetic Field

So far the magnetic field on either side of the magnetic x-line has been assumed to be purely anti-parallel. However, more generally, the magnetic field may have a component pointing into the page. This field is called the guide field and the associated reconnection process is called component reconnection, or guide-field reconnection. With purely resistive MHD, where Ohm's law is given by Eq. 1.5, the reconnection rate is 'slow'. However, as in anti-parallel reconnection, the addition of the hall and pressure terms in Ohm's law can give fast reconnection.

This increase in the rate of guide-field reconnection was first seen in reduced MHD simulations by Aydemir [36], but the physical mechanism was clarified by Kleva *et al.* [28]. The component of Ohm's law (Eq. 1.13) along the magnetic field may be written as

$$E_\parallel = \eta J_\parallel - \frac{T_e}{ne}\nabla_\parallel n \tag{1.14}$$

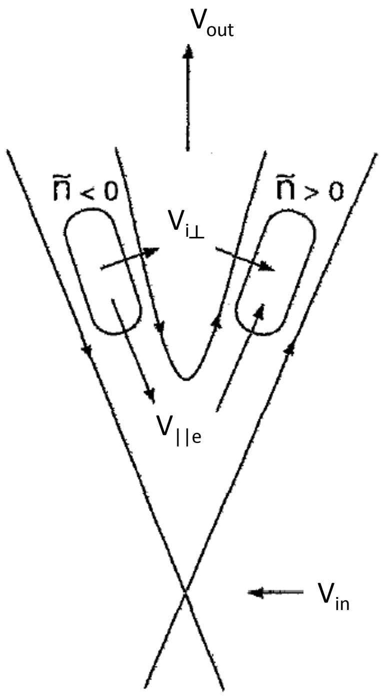

Figure 1-7: Mechanism by which pressure force balances parallel electric field in guide-field reconnection. From Ref. [28].

where uniform electron temperature is assumed. A non-zero parallel electric field, which violates Alfvén's theorem and enables reconnection, can now exist even in regions where the current density is negligible. Figure 1-7 shows the mechanism by which Eq. 1.14 is satisfied. The parallel (magnetic field aligned) electric field drives parallel current at the x-line. This electron current flows along field lines which bend into the outflow region, creating regions of local enhancement and depletion in the electron density. To maintain charge neutrality, the slower ions respond by moving not along the field, but across it through ion polarization currents. The ion displacements create a field aligned pressure gradient, which can balance a parallel electric field farther away from the x-line.

The consequence of this larger region of non-zero parallel electric field is that the outflow region becomes broader, yielding faster reconnection than in purely resistive MHD. The outflow no longer serves as a nozzle that limits the inflow velocity. The inclusion of a guide magnetic field breaks the up-down symmetry of the reconnection dynamics. A distinctive feature of guide-field reconnection is the quadrupolar

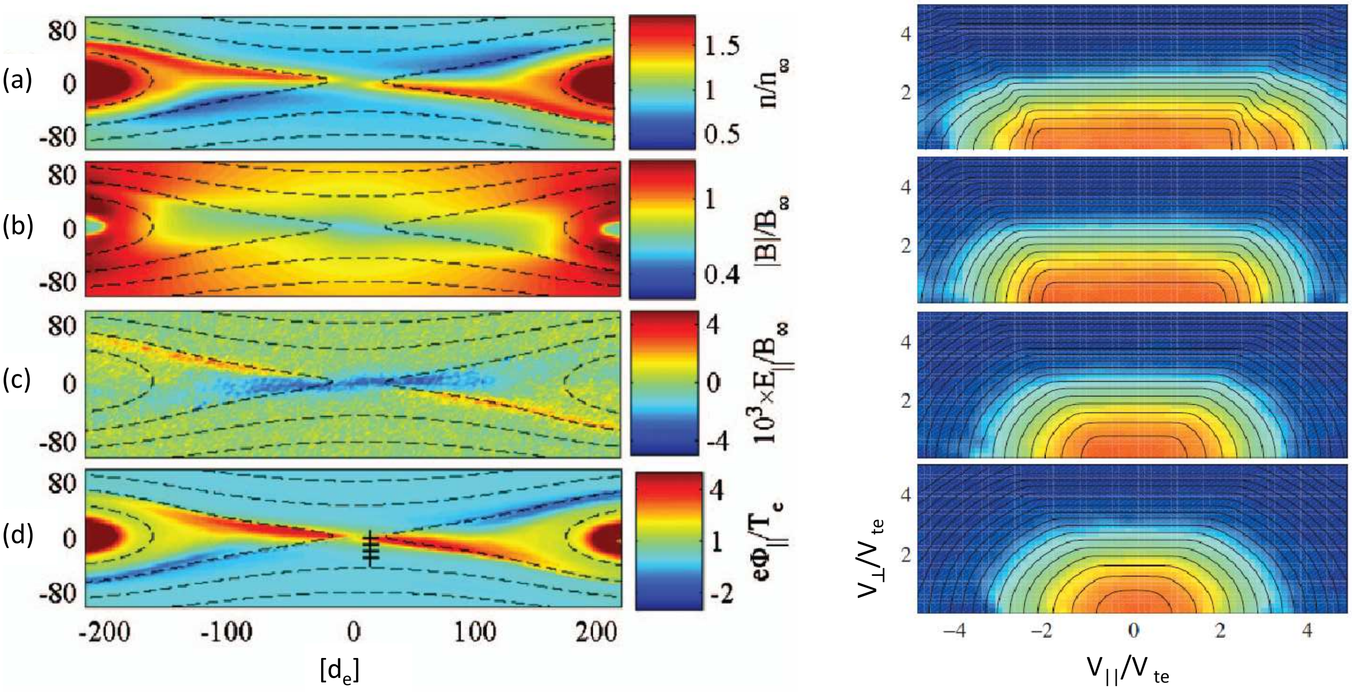

Figure 1-8: PIC simulation of guide-field reconnection. (a) Density normalized to density far from the x-line; (b) magnetic field magnitude; (c) parallel electric field; (d) acceleration potential. At right: increasingly anisotropic electron distribution functions at the locations marked in (d). From Ref. [37].

structure in the density (in contrast to the quadrupolar out-of-plane magnetic field in anti-parallel hall reconnection). This feature is shown in Fig. 1-8a, for a PIC simulation with a guide-field [37].

An important length scale in collisionless guide-field reconnection is the ion sound gyroradius, $\rho_s \equiv c_s/\omega_{ci}$. This scale arises naturally from the fact that ion polarization currents—whose ion velocity is $v_i = -\nabla_\perp^2\phi/(B\omega_{ci})$—balance the field-aligned electron current [28]. To see this, consider the ion density

$$\frac{dn_i}{dt} = -n_i \nabla \cdot v_i = \frac{n}{B\omega_{ci}}\frac{d}{dt}\nabla_\perp^2\phi. \tag{1.15}$$

Integrating, and applying quasineutrality, we find

$$\log n_e = \log n_i = \frac{1}{B\omega_{ci}}\nabla_\perp^2\phi \tag{1.16}$$

Substituting n_e into Eq. 1.14 yields

$$E_\parallel - \eta J_\parallel = -\frac{T_e}{e}\nabla_\parallel \log n = \frac{T_e}{m_i}\frac{m_i}{eB\omega_{ci}}\nabla_\parallel \nabla_\perp^2 \phi = \rho_s^2 \nabla_\parallel \nabla_\perp^2 \phi, \tag{1.17}$$

which introduces the scale ρ_s. For length-scales of the order of ρ_s, the right-hand side of this equation can balance the parallel electric field even where the resistive term is small.

Although fast reconnection results from Kleva's mechanism, the addition of a guide field in reconnection simulations generally slows the reconnection rate. For example, in a PIC simulation [38] the reconnection rate decreased by a factor of 2-3 compared to anti-parallel reconnection.

Kleva *et al.* assume a scalar pressure, but in general the pressure is a tensor, and this fact can alter Ohm's law in important ways. This is especially true when anisotropies exists in the particle distributions. These anisotropies may readily develop in collisionless plasmas, and they have been observed in the electron distribution function by in situ measurements in the magnetotail [14, 13]. The mechanism for the development of the anisotropy has been clarified Egedal *et al.* [39, 40, 41], who derived an adiabatic solution for the electron distribution function. Building on this work, Le *et al.* [42, 29, 37] used this distribution to obtain the appropriate equations of state, which represent a new closure for the fluid equations. In accompanying collisionless particle-in-cell (PIC) simulations—both with and without a guide field—Egedal and Le *et al.* demonstrated the development of an effective acceleration potential, which arises to maintain quasineutrality near the x-line. Figure 1-8 shows the results of such a simulation with a guide-field. Although the parallel electric field (c) is weak, when it is integrated along field lines from the boundary, the resulting acceleration potential $\phi_\parallel$ is several times the electron temperature. This implies that most thermal electrons become trapped. The theory assumes that the electrons bounce many times as they enter the reconnection region ($v_{te} \gg v_A$). The resultant electric—and magnetic—trapping cause strong anisotropy in the electron distribution function (Fig. 1-8 at right). When the pressure is computed from this anisotropic distribution function, it changes Ohm's law. Specifically, the parallel Ohm's law (Eq. 5 in Ref. [37]) becomes

$$-neE_{\|} = -\nabla \cdot \mathbf{P} = -\nabla_{\|} p_{\|} + (p_{\|} - p_{\perp}) \nabla_{\|} \log B. \tag{1.18}$$

The effect of the anisotropy can enhance the magnitude of the pressure term significantly [37], since in the limit of strong trapping, the parallel pressure is found to scale as $p_{\|} \propto n^3/B^2$ (CGL scaling [43]). A doubling in density and a reduction in B by half yield an order of magnitude enhancement in the pressure term compared with the scalar pressure theory ($p = nT$). The enhanced pressure term balances a larger electric field, resulting in faster reconnection. The acceleration potential causes not only particle trapping, but it also heats electrons to many times their ambient temperature. Such heating has been observed near a reconnection region in the magnetotail as well [14].

While questions remain about steady-state magnetic reconnection in 2D, we have seen that there has been much progress on this problem. One of the advances is that the importance of the Hall term has been established in theory and laboratory and space observations. While the effect of boundary conditions on the stability of steady-state Hall reconnection is still unclear [44], Hall reconnection clearly provides a mechanism which gives fast reconnection in 2D.

1.3 The Trigger Problem

Magnetic reconnection is often not steady-state, but rather explosive, involving the sudden release of stored magnetic energy. This explosive nature of magnetic reconnection is not well understood. For example, it is not clear why in the solar wind, reconnection proceeds in a quasi-steady-state in very elongated structures ($>$ 390 Earth radii) [16], while solar flares and magnetospheric substorms have impulsive time-dependent character [6]. Furthermore, impulsive reconnection events usually follow an extended period of steady, slow reconnection in which magnetic stress accumulates in the system. The question is, then, what causes the sudden onset of fast magnetic reconnection?

Much theoretical work has addressed the problem of reconnection onset. In tokamaks, sawtooth triggering has been explored as a transition from a slow tearing mode to a fast m=1 kink-tearing mode [45], while other work pointed to the importance of the hall term in Ohm's law for fast reconnection onset [46]. The onset of reconnection in tokamaks has also been ascribed to magnetic field line stochasticity in both theoretical [47] and experimental [48, 49] investigations; however, in some tokamak sawteeth, stochasticity is clearly not the trigger mechanism [50]. The sawtooth instability is also observed in reversed field pinches, where its onset is characterized either by nonlinear mode coupling, or by linear instability, which results in a spontaneous onset [51].

In addition, simulations—both fluid and kinetic—have been used to tackle the onset problem in geometries simpler than those of tokamaks. For example, in a 2D PIC simulation with a guide magnetic field, spontaneous and explosive reconnection was observed from an initial current sheet, with apparently unconstrained island growth [52]. Other PIC simulations—both 2D and 3D—have shown that the lower-hybrid drift instability may play a role in triggering reconnection [53, 54, 55]. Recent work by Cassak [56, 57, 58], using both two-fluid and PIC simulations in 2D, has shown that reconnection—either with or without a guide-field—displays a transition from a slow Sweet-Parker regime to a fast hall reconnection regime. This transition occurs within a bi-stable parameter space as the width of a resistive current sheet approaches the ion inertial length or ion sound gyroradius. Large-domain fluid simulations have also been carried out for solar reconnection, where coronal mass ejections are thought to be caused by reconnection triggered by emerging flux [59].

1.4 Reconnection in 3D

When the constraint of 2D symmetry is relaxed, the character of magnetic reconnection may change, and new questions arise. In fully 3D reconnection, when there is no magnetic null ($\mathbf{B} \neq 0$), there is a tangle of magnetic field lines and currents. In this case, it is not necessarily clear how to define the separatrix, which demarcates the inflow and outflow regions in 2D. This issue has been addressed in a recent laboratory experiment by Lawrence *et al.* ([60] and references therein) who employs a quasi-separatrix layer [5] to describe the merging of two flux ropes. The situation becomes more difficult in a turbulent plasma, in which reconnection regions may develop on multiple scales [61]. Reconnection in a turbulent plasma has been observed in the magnetosheath by the cluster spacecraft [62]. It has been shown that turbulence can enhance the rate of reconnection beyond the Sweet-Parker rate [63].

An unanswered question is whether 3D effects are important for the onset of reconnection. Recent measurements of the tokamak sawtooth suggest that they are. These measurements, which take advantage of advances in electron cyclotron emission imaging [64, 65, 66], have shown that sawtooth onset is localized both toroidally and poloidally and that the temperature profile flattening is well-organized as opposed to stochastic [67]. The localization is observed even though the magnetic field geometry is mainly 2D. The localized onset of the sawtooth is associated with a global plasma mode, which may break the toroidal symmetry. In less constrained experiments of spheromak merging, 3D reconnection structures are observed, which result in very strong ion heating [34].

Two-fluid and PIC simulations, which have enabled significant progress in 2D reconnection research, are very computationally intensive in 3D. 3D PIC simulations have so far used very small simulation domains (several d_i long) (e.g. [68, 54]), but new PIC simulations by Daughton [69] on the first peta-flop computer at LANL promise to improve on this. Preliminary observations show complicated filamentation, which is related to the formation of new oblique modes that require three dimensions.

Observations of reconnection on the sun also show a 3D nature, and have been interpreted in terms of quasi-separatrix layers [70]. In addition, a comprehensive analysis of flares seen by the TRACE and SoHo satellites shows that a localized brightening can propagate along an arcade of post-flare loops [71, 11]. As the flare propagates, the flare ribbons at the foot of the loops move apart as well (see Fig. 1-9). As we will see, the experiments described in this thesis display very similar behavior.

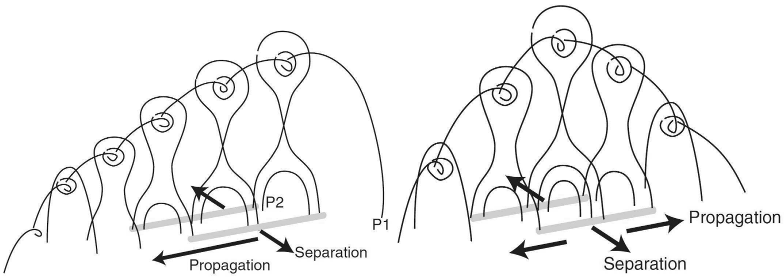

Figure 1-9: Cartoon from Tripathi *et al.* [71] that show how reconnection can propagate along a solar arcade.

1.5 Summary and Outline

Despite the improved measurement techniques applied in tokamaks and solar observations, the internal magnetic and electrical 3D structure of the reconnection region is still unknown. In this dissertation we describe observations of the localized (3D) onset of magnetic reconnection in a well-diagnosed laboratory experiment. The organization is as follows.

In Chapter 2, we discuss reconnection in the fully collisional regime; specifically, we investigate the drag exerted by a neutral gas on flowing plasma structures—such as in a reconnection outflow region. We discuss the importance of the results to the edge of tokamak plasmas, and we suggest a link to reconnection in the solar photosphere. In the remainder of the dissertation, we discuss magnetic reconnection in the collisionless regime.

In Chapter 3, we discuss the experimental setup, plasma production, and reconnection drive which we use for collisionless reconnection experiments. In Chapter 4, we describe the observation of spontaneous reconnection and show that the reconnection rate is not described by a resistive Ohm's law. In Chapter 5, we describe the experimental observation of toroidal localization in the spontaneous onset of magnetic reconnection, by showing detailed 3D measurements of the plasma parameters. We also characterize a global rational q mode, which is necessary for the observation of reconnection. In Chapter 6, we show how this mode, seen in the electrostatic potential, is required for an asymmetric toroidal current. In addition, we compute the growth rate of the spontaneous reconnection using a model relating the potential, current density, and reconnection rate. Relatively good agreement is found with the experimentally measured growth rate. In Chapter 7 we summarize the dissertation and present our conclusions. Appendix A confirms that 2D measurements of the magnetic vector potential provide a valid description of the 3D dynamics of VTF.

Chapter 2

Collisional Reconnection and the Dragging of Plasma Filaments by Neutral Gas

The resistivity in theories of reconnection may be due to electron-ion collisions, anomalous resistivity related to turbulent fluctuations, or electron-neutral collisions. In the presence of a neutral gas, the reconnection may be influenced by ionization and recombination rates [72], as well as by the drag exerted by the neutrals on the plasma flow. Here, we focus on the effect of such neutral drag. The experiments described in this chapter are relevant to plasmas at the edge of tokamaks, but they may also be applicable to reconnection in the solar photosphere and the interstellar medium, where the ionization fraction is low. We describe the coupling of plasma to neutral gas for the case of a plasma filament propagating across a magnetic field through a background of neutrals. This chapter follows Ref. [73].

A plasma filament, also called a 'blob', is a magnetic field-aligned structure in which the density or some other plasma parameter is enhanced [74]. Such structures propagate convectively across the magnetic field for multiple perpendicular scale-lengths while maintaining their shape. The propagation of plasma blobs is important to the overall dynamics in a variety of plasmas, both in space and in fusion laboratory experiments. For example, propagating filaments are observed in the solar photo-

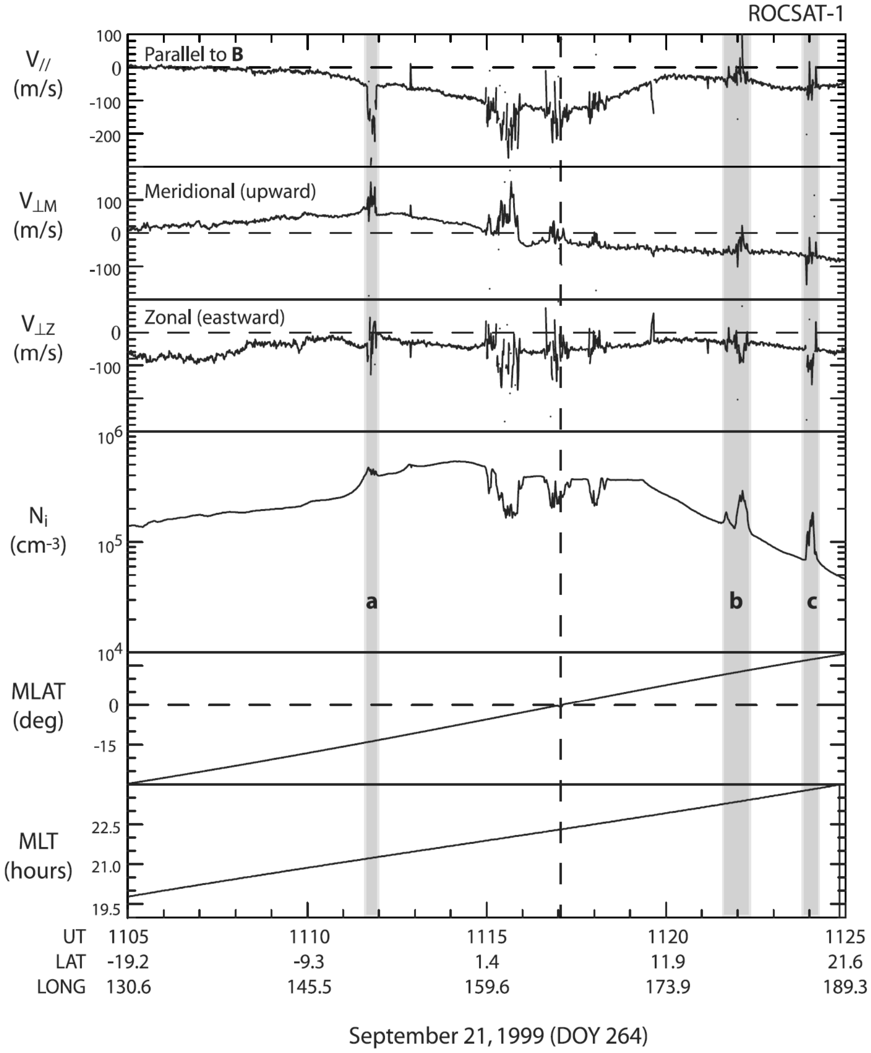

Figure 2-1: Plasma velocity and density in the nightside equatorial ionosphere as observed by ROCSAT-1. Structures with enhanced density (shaded regions) are seen to propagate relative to the background plasma. Reproduced from Ref. [78].

sphere [75], as mentioned above, and in the F layer of the ionosphere [76, 77, 78], where there is non-negligible neutral density. Figure 2-1 shows measurements of field-aligned density enhanced structures in the low-latitude, night-time ionosphere. Typically these blobs are of order 100 km in size and they tend to propagate upward relative to the background plasma.

Blobs are also observed near the edge of many laboratory plasmas, including experiments with linear and toroidal geometries [79, 80, 81, 82]. In tokamaks, for example, density fluctuations tend to be larger near the plasma edge, where the magnetic

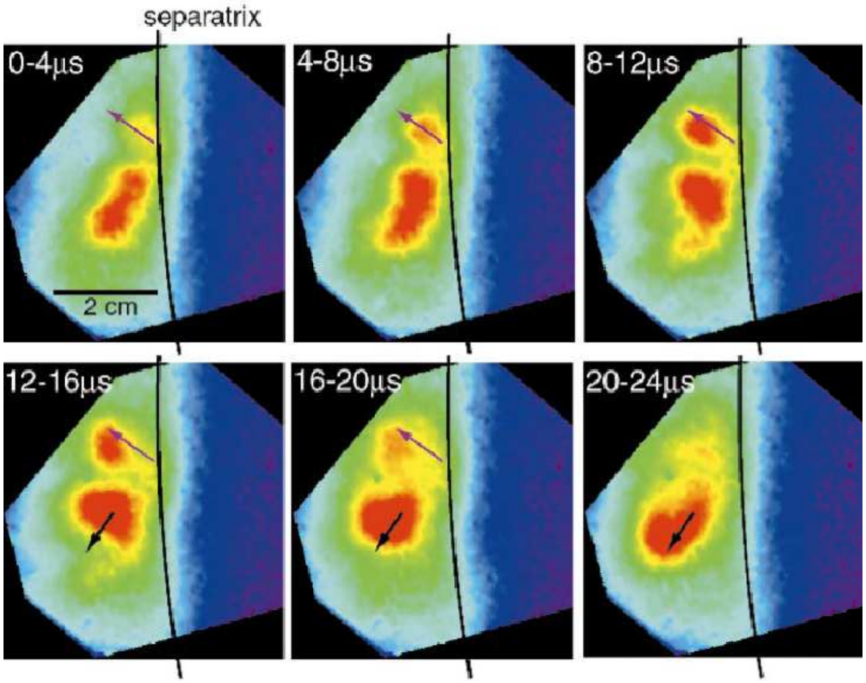

Figure 2-2: Images of edge turbulence in Alcator C-Mod, observed with fast camera. The blobs are imaged using gas puff imaging of D_α radiation, and they are seen to propagate away from the last closed flux surface (the separatrix) towards the chamber wall at left. Reproduced from Ref. [85].

field lines terminate at a metal surface and the neutral density becomes significant [83, 84]. Field-aligned blobs can be identified among these fluctuations, and their convection leads to non-diffusive transport [84]. An example is presented in Fig. 2-2, where a progression of images shows the propagation of density-enhanced structures away from the main plasma. The line indicating the separatrix demarcates the main plasma, where the field lines close on themselves, from the scrape-off layer, where the field lines intersect the divertor or the limiter. The images show D_α radiation from a puff of deuterium gas injected into the plasma. The view is approximately that of a poloidal cross-section, and the density enhancements are aligned with the strong toroidal magnetic field.

Blobs in tokamaks are driven by magnetic field curvature, and this drive–which is proportional to electron temperature–competes with a variety of forces that slow and break up the blobs. The basic picture of blob propagation in a tokamak is described in Fig. 2-3. The electrons and ions experience curvature and ∇B drifts in a $1/R$

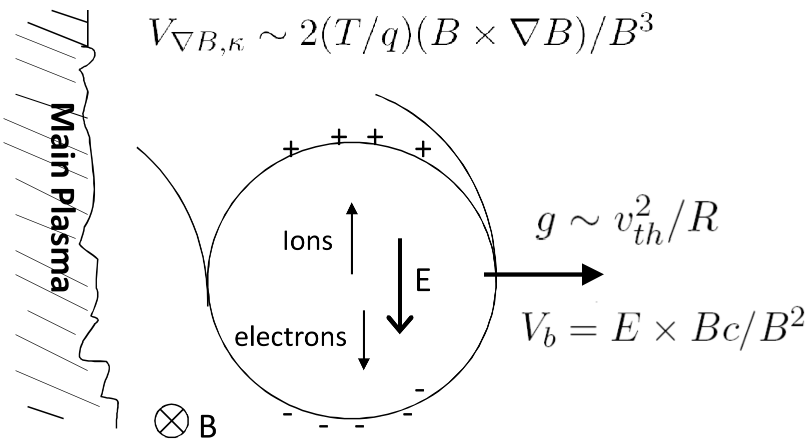

Figure 2-3: ∇B and curvature drifts cause charge separation, resulting in vertical electric field. The resulting $\mathbf{E} \times \mathbf{B}$ velocity sends the filament radially outward, away from the main plasma. Alternatively, this motion can be ascribed to an effective gravity, proportional to the toroidally circulating electrons.

toroidal magnetic field, which cause vertical charge separation. The resulting electric field gives radially outward $\mathbf{E} \times \mathbf{B}$ velocity, which ejects the blob from the plasma. Alternatively, the radial drive can be ascribed to the toroidal motion of the electrons, which results in a effective, centrifugal gravity pointing radially outward. The theory of convective blob transport in tokamaks is relatively well-developed (see for example [74, 86], or for geometry similar to ours [87]). In particular, the scaling of the blob velocity with various parameters has been studied intensively, because this velocity is thought to be important for the plasma confinement [86]. In experiments, however, the plasma conditions often prevent detailed internal probing, and spectroscopic methods are favored (e.g. [80]).

The experiments of this chapter may be relevant as well to reconnection in the solar photosphere, since flowing plasma filaments are expected in the outflow of reconnection regions. These flowing filaments must interact with the neutral gas in the photosphere, which may decelerate the filaments. The applications to photospheric reconnection are further explored in Section 2.6.

2.1 Experimental Setup

The basic experimental setup is shown in Fig. 2-4(b) using a poloidal cross-section of the vacuum vessel. As in the spontaneous reconnection experiments, there is an imposed toroidal magnetic field, which depends on major radius as $\mathbf{B}_{\mathrm{tor}} = (B_0 R_0/R)\mathbf{e}_\varphi$, where $B_0 = 40$ mT and $R_0 = 1$ m. We use only electron cyclotron resonant heating to build up density, as opposed to the reconnection experiments which also use ohmic heating. This limits the plasma density to approximately 2×10^{16} m^{-3}. We use only 60 μs of microwaves (at 15 kW and 2.45 GHz) so that the blob creation time is shorter than the propagation time.

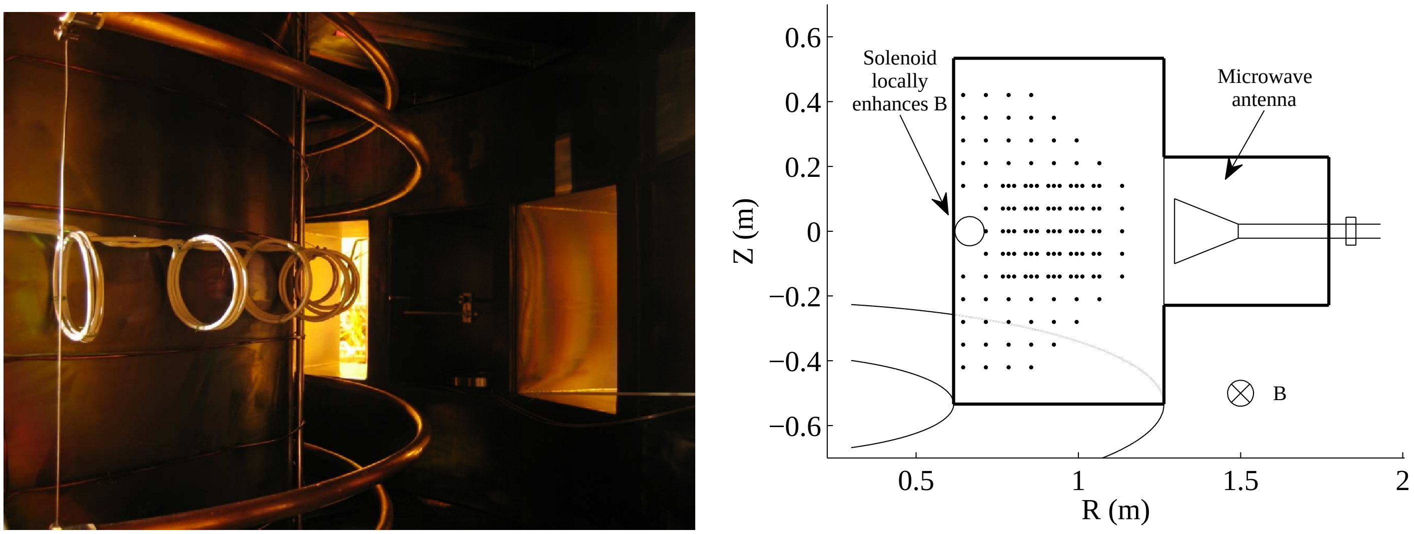

(a)

(b)

Figure 2-4: (a) Photograph of VTF chamber with solenoid at inner wall; (b) experimental setup for filament propagation experiments. The solenoid locally enhances the toroidal magnetic field to provide electron cyclotron resonance at the inner wall. The resulting toroidal plasma filament propagates radially outward, diagnosed the Langmuir probes indicated by dots. Reproduced from Ref. [73].

Since the toroidal magnetic field does not depend on Z, the breakdown would be expected to occur at all heights Z inside the vacuum vessel. To avoid this, we turn down the toroidal field so that the resonance condition does not occur inside the vacuum vessel, and we locally enhance the toroidal field at the inner wall. This is accomplished using a solenoid, shown in Fig. 2-4. Electrons then resonate with the microwaves only near the solenoid, where $|B| = 87$ mT. Even though the RF power is injected by a single horn antenna, the microwave reflections off the chamber walls give axially symmetric breakdown. Since the field is purely toroidal, there are no field lines terminating at the wall and therefore no sheaths to drain current along the field.

The plasma consists mainly of singly-charged argon ions, and is created in a chamber filled with argon gas at 4×10^{-5}–4×10^{-4} Torr, corresponding to 10^{18}–10^{19} m^{-3}. Since the plasma density is typically 2×10^{16} m^{-3}, the ionization fraction is less than 2%, and there is a constant, relatively uniform background of neutrals even after breakdown. Unlike the reconnection discharges, the blobs are very reproducible. Table 2.1 shows some of the plasma parameters for the blob experiments.

Parameter	Symbol	Value
Density	n	$\sim$ 1-2 $\times 10^{16}$ m^{-3}
Neutral argon density	n_0	10^{18}–10^{19} m^{-3}
Electron temperature	T_e	~ 2 eV
Ion temperature	T_i	$\lesssim$ 1eV
Plasma β	$\beta \equiv \frac{2\mu_0 p}{B^2}$	$\sim 10^{-5}$
Toroidal magnetic field	B_{tor}	40 mT
Poloidal magnetic field	B_{pol}	0 mT
Ion cyclotron frequency	ω_{ci}	10^5 s^{-1}
Electron cyclotron frequency	ω_{ce}	10^{10} s^{-1}
Sound speed	c_s	2.2×10^3 m/s
Ion gyroradius	ρ_i	~ 1.5 cm
Electron gyroradius	ρ_e	80 μm
Debye length	λ_{de}	70 μm

Table 2.1: Some of the plasma parameters for the filament propagation experiments

2.2 Diagnostics and ABR Theory for Langmuir Probes

The plasma is tracked by an array of 200 Langmuir probes. The tip spacing is 7 cm horizontally and 7 cm vertically, with triple resolution (horizontally) near the center (see Fig. 2-4(b)). The main Langmuir probe array is located at a single toroidal angle, but other Langmuir probes are used to verify the azimuthal symmetry of the blobs. The other probes (not shown in Fig. 2-4(b)) include 3 vertical lines of stainless-steel cylinders placed at different toroidal angles.

These cylinders were nearly 10 times larger in area (3.3 cm length × 3 mm diameter) than our usual Langmuir probes in order to minimize the sheath resistance. Recall from Section 3.2.1 that the sheath resistance between the plasma and the probe in floating mode is given by $R_p = dV/dI|_{I=0} = T_e/(eI_i)$, where I_i is the ion saturation current. At the edge of the blob, the density—and hence the ion saturation current as well—is low, and this resistance can be large. For example, for $n = 10^{15}$ m^{-3}, $R_p = 20$ kΩ for the large probes. Given a wire capacitance of $C_s \sim 50$ pF, the filter time constant is $R_pC_s \sim 1$ μs, which is on the order of the digitization time resolution. This justifies the need for large probes, since our regular Langmuir probes have R_p about 10 times larger, and the floating potential would be filtered in time.

In addition to the Langmuir array and the large floating potential probes, we use a horizontal line of cylindrically shaped, heated tungsten filaments (Fig. 2-5). These filaments are used to measure the full I-V characteristic, and hence the electron temperature and plasma potential. We heat the filaments to $\sim 1000^\circ$ K for 5 s before each discharge.

Heating the filaments between discharges eliminates important surface contamination effects, and prevents overestimation of the electron temperature (see e.g. [88, 89]). Evidence for this claim is shown in Fig. 2-6, where the I-V Langmuir characteristics are shown for the same probe with and without heating. Each curve represents data from more than 70 discharges, recorded for the same probe with similar plasma conditions. The bias voltage to the Langmuir probe was changed before each discharge, and during the course of this bias scan, the bias was increased and decreased twice, tracing out the black curve as shown by the arrows. The black curve shows evidence of hysteresis, while the red curve does not. Furthermore, the slope of the exponential part of the black curve is much smaller than that for the heated probe. Since the electron temperature is inversely proportional to this slope (see Eq. 3.2), the unheated probe underestimates the electron temperature by an order of magnitude. The elec-

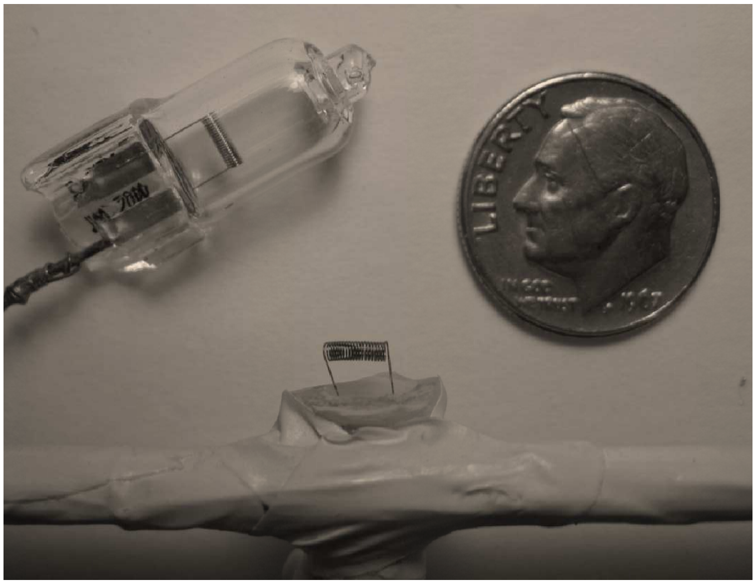

Figure 2-5: Tungsten filament (bottom) used as Langmuir probe to measure full I-V characteristic. We use a halogen light bulb, removing the glass enclosure to retain the tungsten filament. The diameter of the wound cylinder is 1.1 mm, and the spacing between the windings is similar to the electron gyroradius.

tron saturation component of the red curve—at large bias—is not reproducible, but this part of the characteristic is not described by Eq. 3.2 and is not used in the curve fitting.

To analyze the I-V characteristic, we use Allen-Boyd-Reynolds (ABR) theory [90], which accounts for the fact that—especially at the edge of the blob, where the plasma is less dense—the debye length is comparable to the probe dimensions. We neglect electron inertia to find a Boltzmann response for the electrons

$$n_e = n_0 \exp{(e\phi/T_e)}, \tag{2.1}$$

where $\phi = V_{\text{bias}} = V_{\text{plasma}}$, while for the ions, we use energy conservation

$$\frac{1}{2} m_i v_i^2 + e\phi = 0 \tag{2.2}$$

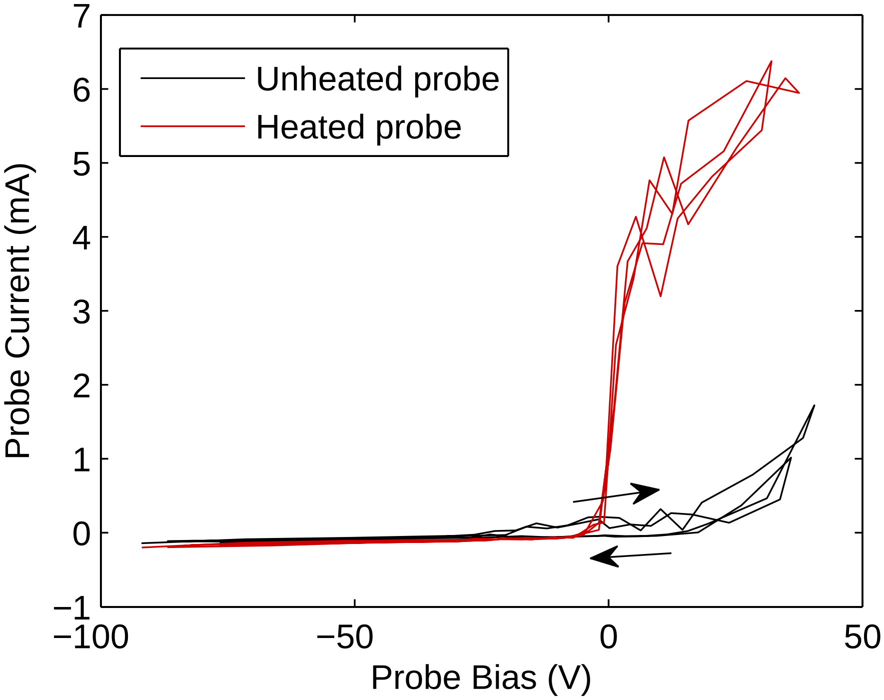

Figure 2-6: I-V characteristics for heated and unheated Langmuir probe. The bias was increased and decreased twice as shots were recorded, tracing out the curves. The unheated probe shows hysteresis and overestimates the electron temperature. Heating was achieved by passing current through tungsten filament probes for 5 s before each discharge.

and mass conservation for cylindrical geometry

$$\frac{I_i}{2\pi rl} = n_i e v_i. \tag{2.3}$$

I_i is the ion current collected by the probe, l is the probe length, and r is the radius. We combine Eqs. 2.2-2.3 to find the ion density as a function of radius

$$n_i = \frac{I_i}{2\pi rle\sqrt{-2e\phi/m_i}}. \tag{2.4}$$

We use Eqs. 2.1-2.4 to find Poisson's equation in dimensionless form, which is given by

$$\frac{y'}{x} + y'' = \frac{I}{x\sqrt{y}} - \exp\left(-y\right) \tag{2.5}$$

where $y \equiv -e\phi/T_e$, $x \equiv r/\lambda_{de}$, $I \equiv I_i/I_1$, and $I_1 \equiv 2\pi\sqrt{2}\lambda_{de} l n_0 e c_s$. For each I, Eq. 2.5 is solved numerically by integrating from large r (large x) up to the probe radius $x_a = a/\lambda_{de}$, where the potential $y_a(x_a, I)$ is evaluated. We then invert this relationship to find $I(x_a, y_a)$. The ion current is then given by

$$I_i(T_e, V_{\text{plasma}}, a/\lambda_{de}, l/a) = I(x_a, y_a) I_1. \tag{2.6}$$

Meanwhile, the electron current to the probe is given by

$$I_e = -eA_{\text{probe}} \int f_e v_z d^3\mathbf{v}, \tag{2.7}$$

where $f_e = (m_e/(2\pi T_e))^{3/2} n_0 \exp\left(-mv^2/(2T_e) + e\phi/T_e\right)$ is the electron distribution function, assumed here to be Maxwellian. The electron current is then given by

$$I_e(T_e, V_{\text{plasma}}, a/\lambda_{de}, l/a) = -\sqrt{\frac{1}{2\pi}} eA_{\text{probe}} n_0 \exp\left(e\phi/T_e\right)\sqrt{\frac{T_e}{m_e}} \tag{2.8}$$

where $A_{\text{probe}} = 2(2rl)$ is the surface area of the probe projected onto the plane. The electrons see the projected area since they are well-magnetized, but the ions impinge on the entire probe surface. Note that the potential ϕ is the bias voltage relative to the plasma potential. Given a measured I-V characteristic, we fit $I_i + I_e$ to find the electron temperature, plasma potential, and density.

2.3 Density and Potential Measurements

To measure just the plasma density or floating potential, it is not necessary to trace out the I-V characteristic throughout the blob. Instead we use unheated probes biased to collect ion polarization current or in floating mode. The Langmuir circuits are similar to those shown in Fig. 3-7. The plasma density and floating potential are shown in Fig. 2-7.

We observe experimentally for the first time the mushroom blob shape, which has been seen in many simulations (e.g. [87, 91]). This is shown at left of Fig. 2-7. The time step between adjacent density plots is 100 μs and the first plot occurs 25 μs after the microwaves are turned off. The blob shape exhibits 'wings', which develop about a blob length away from the creation region. The right-hand part of Fig. 2-7 shows the floating potential with some overlayed density contours. The arrows indicate the $\mathbf{E} \times \mathbf{B}$ velocity, similar to that of a pair of vortices at the top and bottom of the blob. The velocity at the blob center is consistent with the radially outward center of mass motion.

The potential is obtained from the the vertical row of large Langmuir probes. This measurement of $\phi(Z, t)$ is then converted to $\phi(R, Z)$ using the measured blob propagation speed $R = v_{\text{blob}} t$ (see below). We use the floating potential to compute the electric field and the resulting $\mathbf{E} \times \mathbf{B}$ arrows are superimposed on the potential. The use of floating potential instead of plasma potential assumes that the electron temperature is uniform. Figure 2-8 shows that this is a good assumption in the evaluation of vertical electric fields. In the figure, we show two I-V characteristics measured with the heated tungsten filaments. The probes are separated by 25 cm in Z and the difference between their floating potentials (8.1 V) and their plasma potentials (7.7 V) are nearly identical. The use of floating potential to compute E_Z is therefore reliable.

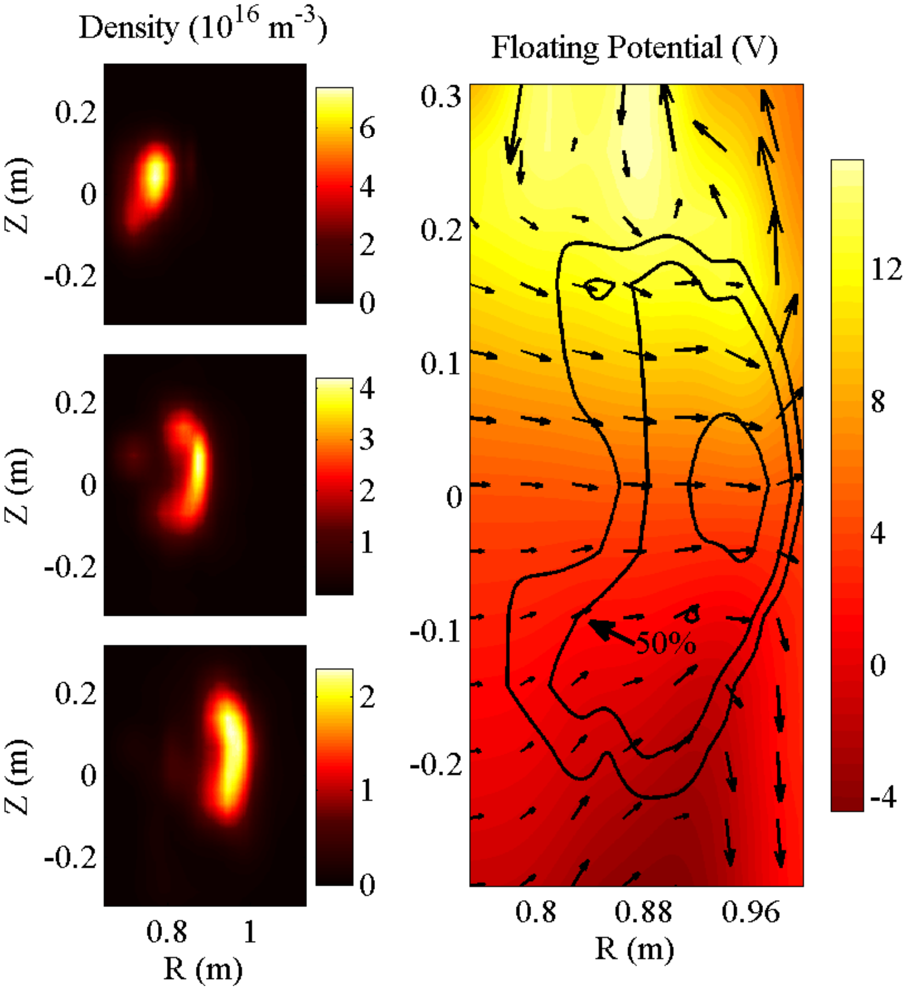

Figure 2-7: Poloidal cross section of typical blob at 3 different times ($\Delta t = 100$ μs), showing characteristic mushroom shape. The density is calculated from the ion saturation current; its decrease is consistent with the expansion of the blob as its diameter increases. The blob propagation is consistent with the vertical electric field, which is reflected in the potential structure at right. The overlaid $\mathbf{E} \times \mathbf{B}$ velocity arrows show the velocity field of a vortex pair. Reproduced from Ref. [73].

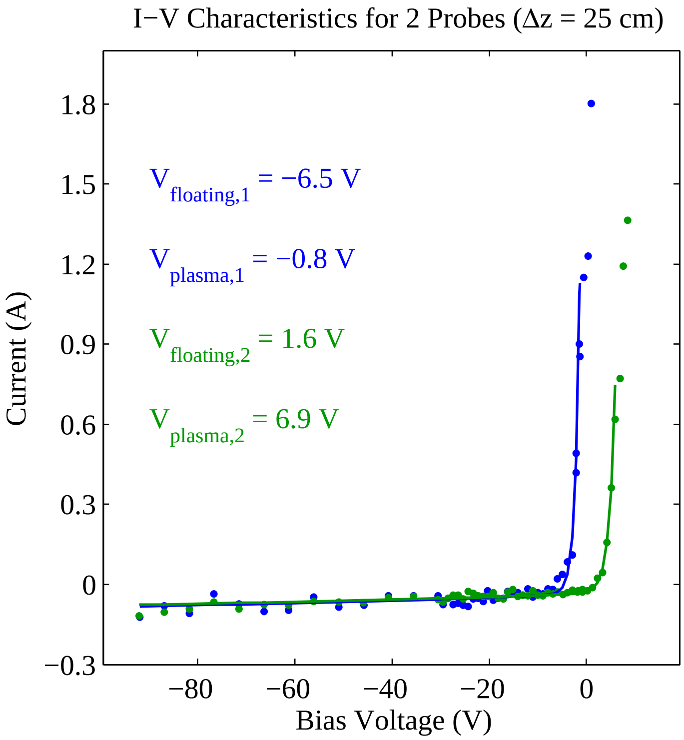

Figure 2-8: I-V Langmuir characteristics for two probes separated by 25 cm in Z. The difference $V_{\text{floating},1} - V_{\text{floating},2}$ and the difference $V_{\text{plasma},1} - V_{\text{plasma},2}$ are nearly identical, thus validating the use of floating potential for calculating E_Z.

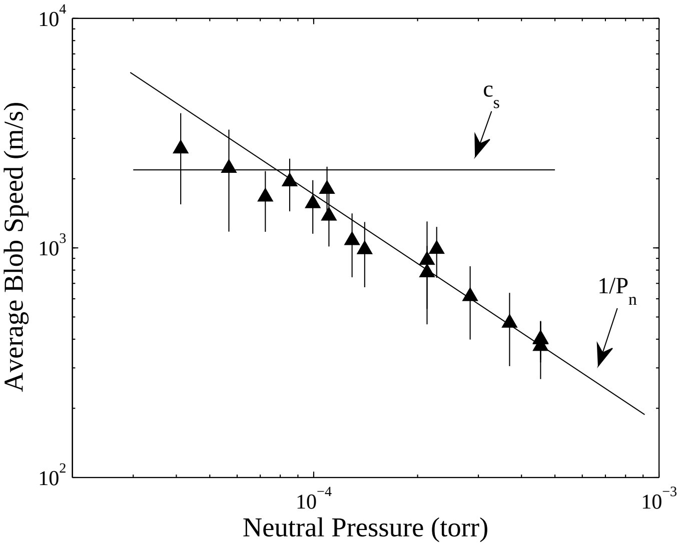

Figure 2-9: Blob center-of-mass speed versus neutral pressure (P_n). The speed scales inversely with the pressure, but this scaling appears to break down at low pressure. The uncertainty in the speed is approximated by the standard deviation of the inferred blob speed as it fluctuates in time. Reproduced from Ref. [73].

2.4 Filament Propagation Speed

2.4.1 Time-of-Flight Measurements and Vorticity Equation

The propagation seen in Fig. 2-7 can be quantified and it is found to depend on the neutral pressure in the chamber. The propagation speed is computed from the blob's center of mass radius (R_{CM}). We compute the average slope of R_{CM} as a function of t. The uncertainty in blob speed is estimated as the standard deviation of the instantaneous blob speed as it varies in time. The propagation speed is measured in multiple discharges with different neutral pressure in the vacuum vessel, and the results for speed are shown in Fig. 2-9. We find that the blob's center-of-mass speed is inversely proportional to the neutral pressure. This is indicated by the fit line with slope $1/P_n$. The second line represents the sound speed ($c_s \equiv \sqrt{T_e/m_i} \approx 2.2 \times 10^3$ m/s), which is an upper bound on the blob velocity. However, the three low-pressure points that give evidence for this bound are from blobs with different shape and very low density.

To describe the blob propagation we derive the MHD vorticity equation including ion-neutral collisions. We start with the momentum equation

$$m_i n \frac{d\mathbf{v}}{dt} = \mathbf{J} \times \mathbf{B} - \nabla p - m_i n \nu \mathbf{v} \tag{2.9}$$

where $d/dt \equiv \partial/\partial t + \mathbf{v} \cdot \nabla$, and ν is the ion-neutral collision frequency. We solve for $\mathbf{J}_\perp$ to find

$$\mathbf{J}_\perp = -\frac{\nabla p \times \mathbf{B}}{B^2} - \frac{m_i n (d\mathbf{v}/dt + \nu \mathbf{v}) \times \mathbf{B}}{B^2}. \tag{2.10}$$

Next, we apply current continuity $\nabla \cdot \mathbf{J} = \nabla_\perp \cdot \mathbf{J}_\perp + \nabla_{||} J_{||} = 0$, assume $\mathbf{B} \sim \mathbf{e}_\varphi / R$, and use the ideal Ohm's law, which can be written as $\mathbf{v} = -\nabla\phi \times \mathbf{B}/B^2$, to find

$$\nabla \cdot \frac{m_i n}{B^2} \frac{d\nabla_\perp \phi}{dt} = \nabla_{||} J_{||} + \frac{2}{B} \mathbf{b} \times \kappa \cdot \nabla p - \nabla \cdot \frac{m_i n}{B^2} \nu \nabla_\perp \phi, \tag{2.11}$$

where $\mathbf{b} = \mathbf{B}/B$, $\kappa = \mathbf{b} \cdot \nabla \mathbf{b}$ is the magnetic curvature. In deriving Eq. 2.11 we have assumed that $v \ll c_s$, and $|B/\nabla B| \gg |n/\nabla n| \sim |v/\nabla v|$. The vorticity is given by $\nabla \times \mathbf{v} \approx \nabla^2 \phi / B$ (where $\mathbf{v} = -\nabla\phi \times \mathbf{B}/B^2$). Equation 2.11 is commonly used in blob theory (see for example Ref. [92]). The concept of vorticity is useful in describing charge separation in a magnetic field. The reason for this is outlined in Fig. 2-10, where in (a) a local buildup of charge Q results in a vortex-like $E \times B$ velocity flow. In the expression for vorticity $\nabla \times \mathbf{v} = \nabla^2 \phi / B$, the quantity ϕ / B^2 is equivalent to the stream function from fluid mechanics. In (b), we see how two such oppositely-oriented vortices—whose velocity arrows are shown in blue—combine to give a propagating blob. This velocity field is similar to the $E \times B$ velocity arrows in Fig. 2-7. The vorticity is proportional to the charge by Poisson's equation $\nabla^2 \phi = -Q/\epsilon_0$.

Eq. 2.11 may be simplified for our experimental geometry. We have purely toroidal magnetic field $\mathbf{B} = B\mathbf{e}_\phi \propto 1/R$, so that $\mathbf{b} = \mathbf{e}_\phi$ and $\kappa = -\mathbf{e}_R / R$. We neglect $\nabla_{||} J_{||}$, since the toroidally symmetric field lines close on themselves, and therefore no charge is lost or gained along the magnetic field. We then obtain

$$\nabla \cdot \frac{m_i n}{B^2} \frac{d\nabla_\perp \phi}{dt} = \frac{2}{BR} \frac{dp}{dZ} - \nabla \cdot \frac{m_i n}{B^2} \nu \nabla_\perp \phi. \tag{2.12}$$

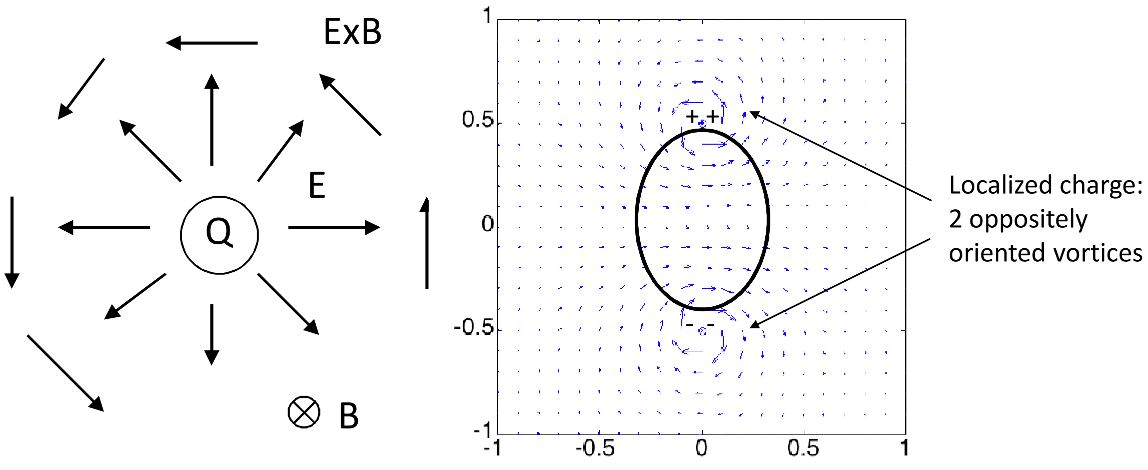

(a) (b)

Figure 2-10: (a) Charge Q in a magnetic field gives vortex-like $E \times B$ velocity arrows; (b) velocity field of two oppositely-oriented point vortices with superimposed blob. The charge accumulation is related to the vorticity.

Recall that this equation is an expression of $\nabla \cdot \mathbf{J} = 0$, which is required for quasineutrality. The terms represent divergence of ion polarization currents (vorticity accumulation), divergence of currents due to curvature and ∇B drifts (outward drive due to centrifugal force on electrons), and divergence of Pedersen currents (collisional damping due to neutrals), respectively. Eq. 2.12 is clearly non-linear, since—together with the density evolution equation ($\partial n/\partial t + \nabla \cdot (n\mathbf{v}) = 0$)—it couples the density and potential fields. Numerical simulations show that the non-linear evolution of the vortex pair that emerges from these arrows is directly related to the formation of the mushroom shape [86, 87]. Meanwhile, the gross features of the vertical electric field (see Fig. 2-7) are maintained directly by the vertical curvature and ∇B currents. The electric field drives Pedersen currents—proportional to both the electric field and the rate of ion-neutral collisions—and adjusts to balance the divergence of the ion and electron currents.

To explain the observation that the blob speed scales inversely with the neutral pressure, we take spatial moments of the density and vorticity equations. The R-moment of the density equation

$$\frac{\partial n}{\partial t} + \nabla \cdot (n\mathbf{v}) = 0 \tag{2.13}$$

gives the center-of-mass motion:

$$\frac{\partial \langle R \rangle}{\partial t} = \langle v_R \rangle, \tag{2.14}$$

where $\langle ... \rangle$ is a spatial-average operator, for example

$$\langle v_R \rangle = \frac{\int n v_R d^3\mathbf{r}}{\int n d^3\mathbf{r}}, \tag{2.15}$$

and the integration volume covers the entire plasma. There is no background plasma, and the blob makes no contact with the chamber walls, so no surface integrals are needed. The evolution of $\langle v_R \rangle$ is computed from the Z-moment of the vorticity equation. We assume steady state propagation and neglect the d/dt term in Eq. 2.12; taking the Z-moment ($\int Z d^3\mathbf{r} \times$) of this equation and integrating by parts gives

$$\nu \left\langle \frac{1}{B} \frac{d\phi}{dZ} \right\rangle = \frac{2\langle T_e \rangle}{m_i R} \tag{2.16}$$

and hence

$$v_{\text{blob}} \equiv \langle v_R \rangle = \frac{2\langle c_s^2 \rangle}{\nu R}. \tag{2.17}$$

where $v_R = -(d\phi/dZ)/B$, $p = nT_e$ (assuming $T_e \gg T_i$), and we have assumed uniform collisionality ν. The ion-neutral collision frequency is $\nu = n_n \sigma \bar{v}_i$, where n_n is the neutral density, σ is the ion-neutral collision cross section, and $\bar{v}_i$ is the mean ion speed. The expression for ν assumes $\bar{v}_i \gtrsim v_{\text{blob}}$, so that the relative velocity between colliding ions and neutrals is $\sim \bar{v}_i$. The scaling of blob speed with neutral density is now apparent:

$$v_{\text{blob}} \sim \frac{1}{n_n}, \tag{2.18}$$

in agreement with Fig. 2-9.

The dominant cross-section for Ar^+ ions impinging on Ar atoms at energies on the order of 1 eV is the symmetric charge transfer cross-section, which we take to be 58×10^{-20} m^2 [93]. Furthermore, we assume an electron temperature $T_e = 2$ eV, leaving T_i as the only unspecified parameter with which to fit the data of Fig. 2-9

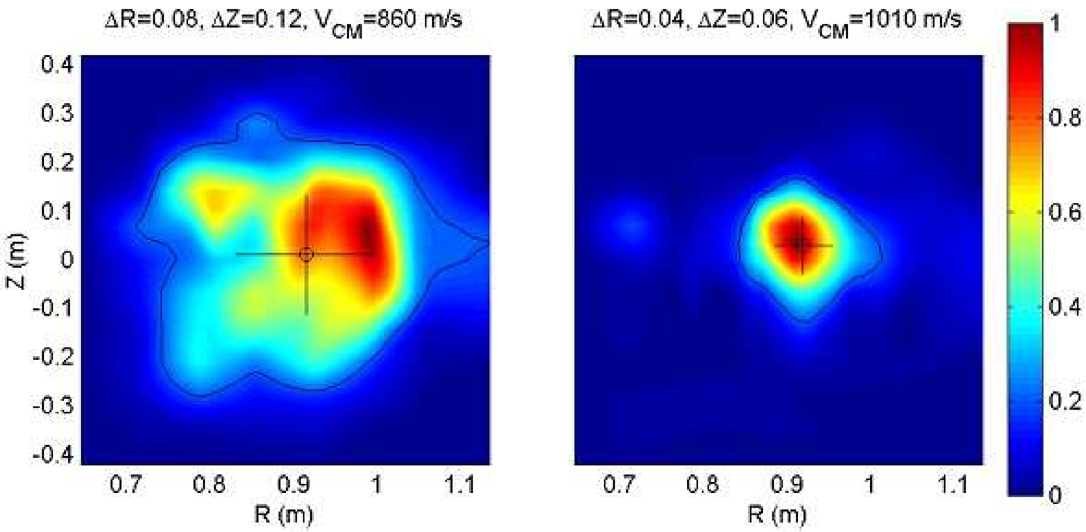
ΔR=0.08, ΔZ=0.12, V$_{CM}$=860 m/s

ΔR=0.04, ΔZ=0.06, V$_{CM}$=1010 m/s

Figure 2-11: Two blob discharges with the same neutral density but different microwave pulse length. The larger blob is approximately twice the size of the smaller one, but their propagation velocity is within 15%, as expected from the scaling of Eq. 2.17.

(since $\bar{v}_i = \sqrt{8T_i/\pi m_i}$). The best fit line in Fig. 2-9 is found for $T_i = 1.1$ eV.

2.4.2 Dependence of Propagation Speed on Blob Size

The scaling of blob speed with blob size depends on which terms are important in the vorticity equation (Eq. 2.11). In our case, the blob speed is independent of its size. Figure 2-11 shows two blobs from different discharges, which have the same neutral pressure (2.1×10^{-4} Torr) but with different RF pulse lengths (10 μs and 150 μs). The longer RF pulse gives a blob about twice the size and with 10 times the density compared to the shorter RF pulse, but the two blob speeds agree within 15%. The blob size is measured as the standard deviation, i.e. $\Delta R = \langle (R - \langle R \rangle)^2 \rangle$. The independence of blob speed on blob size is also consistent with Eq. 2.17, for the regime in which the drive term is completely balanced by the drag term.

2.4.3 Measurement of E×B Velocity

The floating potential structure of Fig. 2-7 is also analyzed quantitatively and the results are consistent with the blob velocity measured by the time-of-flight method.

Fig. 2-12 shows the average E × B velocity (empty symbols) calculated from floating potential measurements using $\langle V_{E\times B}\rangle_c = (\int_c n(E_Z/B_0)RdZdR/\int_c nRdZdR)$, where the contour c includes 50% of the total particles (as measured from ion saturation). This 50% contour (see Fig. 2-7) is chosen to include a significant amount of plasma while maintaining a density high enough to ensure the accuracy of the measurement. Recall that for low density, the floating potential signal is R-C filtered (Section 2.2). The 40% and 60% contours give the error bars displayed in the figure. Assuming T_e has an insignificant dependence on Z, the vertical electric field in the plasma is obtained from the floating potential.

Figure 2-12 also shows blob velocity measurements for comparison (filled symbols). These are calculated from the 3 vertical lines of Langmuir probes shown in the inset; the error bars are calculated assuming 5 mm uncertainty in the line separation. For each pair of vertical lines of Langmuir probes, the velocity is found from the time at which the center-of-mass (of ion saturation current) crossed the line. Velocity measurements at two different radial locations (circles and triangles) show clear evidence for the blob slowing down with increasing radius. The decrease in blob speed is expected due to the decrease in electron temperature (since $v_{\text{blob}} \propto T_e$ from Eq. 2.17). At low fill pressure, the measured electric fields underestimate the blob velocity, probably due to systematic errors associated with measurements at low plasma density. The use of floating potential to infer the electric field is checked by measuring the plasma potential directly from the full I-V characteristics (see Fig. 2-8).

2.4.4 Blob Propagation through Neutral Cloud

We use gas puffing at the inner wall in order to create blobs in the low neutral density regime. At the time of blob birth, the neutral density in the cloud by the inner wall may be high, while the neutral density in the rest of the chamber is low. Without the gas puff, at low fill pressure, the blob density is too low to measure the propagation. Hence, in Fig. 2-9—recorded with no gas puffing—the low pressure blob speeds have large error bars. By using gas puffing at the inner wall, we hoped to create blobs with observable density, which would then propagate away from the gas puff and be

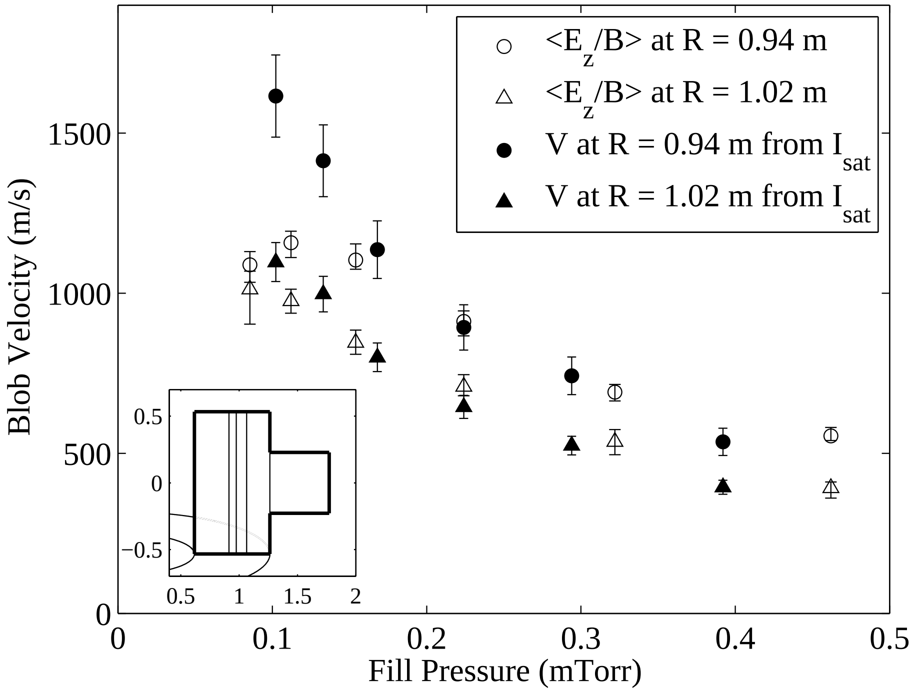

Figure 2-12: $v_{\mathrm{E}\times\mathrm{B}}$ (empty symbols) as a function of neutral pressure in the vacuum vessel. This velocity is evaluated at two values of R using the vertical probe lines shown in the inset. Filled symbols indicate center-of-mass velocity evaluated from time-of-flight method. The blob slows with increasing major radius. Reproduced from Ref. [73].

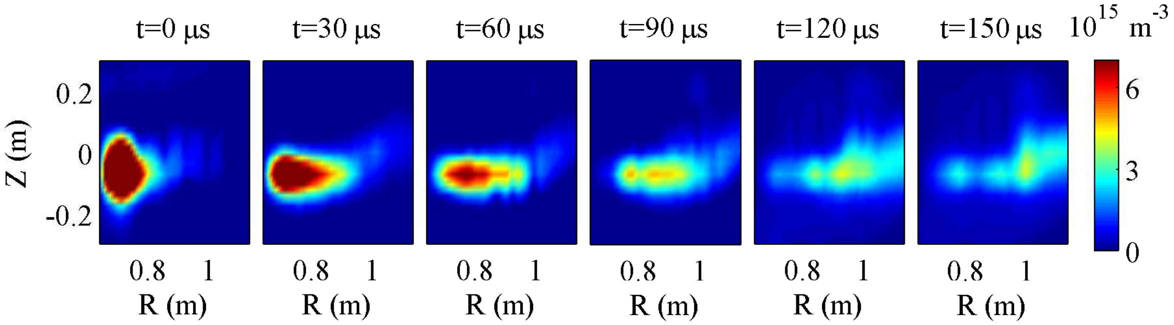

Figure 2-13: Blob entrainment in a cloud of neutrals by the inner wall. Outside the cloud, $P_n = 2 \times 10^{-5}$ Torr, and the front of the blob moves faster than its back, stretching it radially.

influenced only by the background neutral pressure in the vacuum vessel. However, the gas puff affects the blob propagation.

A typical blob in a discharge with gas puffing is shown in Fig. 2-13. The resulting blob is stretched in the radial direction since part of it is entrained in the cloud of neutrals. The background neutral pressure in the chamber is 2×10^{-5} Torr, and the center of mass propagation is approximately 2.2×10^3 m/s. The argon gas puffing occurs at 6 toroidal locations and uses fast piezoelectric valves. The valves are opened 1 ms before the burst of microwaves and the neutral atoms can travel at most 30 cm away from the inner wall during this time. During the short time of the blob propagation, the neutral density profile can be approximated as fixed. It is emphasized that the stretching of the blob is due to its motion along a gradient in neutral density.

2.5 Energy Loss during the Filament Motion

The electron temperature (measured with Langmuir probes) at the peak density decreases by about 50% as the blob propagates across the chamber ($\Delta R \sim 35$ cm). The cooling of the electrons results from their motion against the vertical electric field of the blob. Consider the energy equation for adiabatic electrons, i.e. ignoring heat flux:

$$\frac{d}{dt}\left(\frac{p_e}{n_e^\gamma}\right) \tag{2.19}$$

where $\gamma = 5/3$. Rewriting, we find

$$\frac{3}{2}\frac{\partial p_e}{\partial t} = -p(\nabla \cdot \mathbf{u}_e) - \frac{3}{2}\nabla \cdot (p_e \mathbf{u}_e). \tag{2.20}$$

We integrate over the plasma volume to find

$$\frac{3}{2}\int \frac{\partial p_e}{\partial t} d^3\mathbf{r} = -\int p_e(\nabla \cdot \mathbf{u}_e) d^3\mathbf{r} = \int (\mathbf{u}_e \cdot \nabla) p_e d^3\mathbf{r} = -\int ne\mathbf{u}_e \cdot \mathbf{E} d^3\mathbf{r} \tag{2.21}$$

where the last step relied on the electron momentum equation dotted with $\mathbf{u}_e$ and with electron inertia neglected. Rewriting, we have

$$\frac{3}{2}\frac{\partial \langle T_e \rangle}{\partial t} = -\langle \mathbf{u}_e \cdot \mathbf{E} \rangle \tag{2.22}$$

showing explicitly how the electrons cool by moving against the electric field.

Next, we eliminate $\mathbf{u}_e$ to find how $\langle T_e \rangle$ evolves with radius. From the electron momentum equation, we have the E×B and diamagnetic drifts

$$\mathbf{u}_e = \frac{\mathbf{E} \times \mathbf{B}}{B^2} + \frac{\nabla p_e \times \mathbf{B}}{neB^2}. \tag{2.23}$$

Substituting this into Eq. 2.22, we find

$$\begin{aligned} \frac{3}{2}\int \frac{\partial p_e}{\partial t} d^3\mathbf{r} &= -\int \frac{\nabla p_e \times \mathbf{B}}{B^2} \cdot \mathbf{E} d^3\mathbf{r} \\ &= +\int p_e \nabla \cdot \frac{\nabla \phi \times \mathbf{B}}{B^2} d^3\mathbf{r} \\ &= -\int p_e \nabla \phi \cdot \nabla \times \frac{\mathbf{B}}{B^2} d^3\mathbf{r}. \end{aligned} \tag{2.24}$$

Since $\mathbf{B} = B_0 R_0 \mathbf{e}_\varphi / R$, we have $\nabla \times (\mathbf{B}/B^2) = 2\mathbf{e}_z/(B_0 R_0)$, and hence

$$\frac{3}{2}\frac{\partial \langle T_e \rangle}{\partial t} = \frac{2}{B_0 R_0}\langle T_e E_z \rangle. \tag{2.25}$$

Assuming uniform E_z throughout the blob, this equation gives the scaling of T_e as a

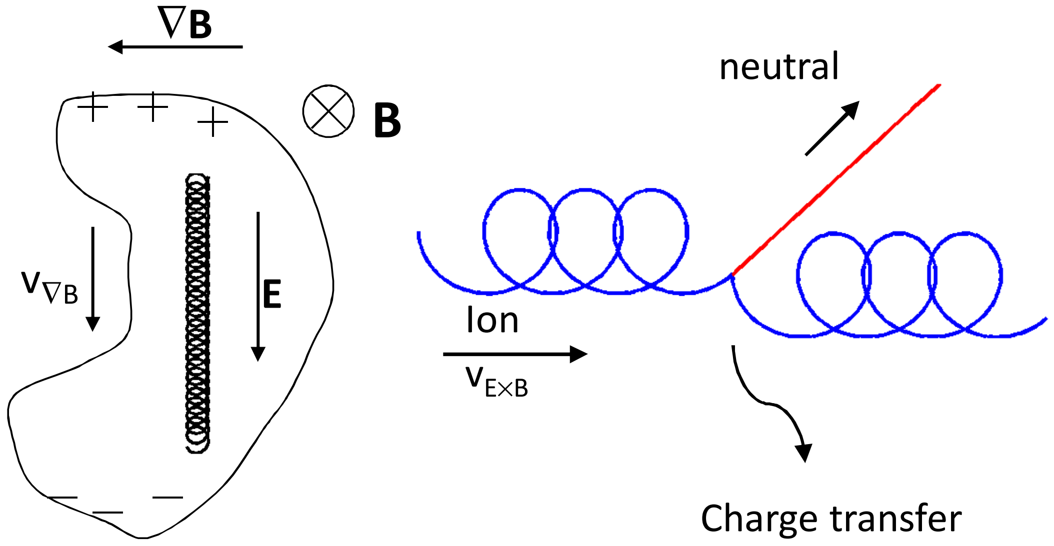

(a) (b)

Figure 2-14: (a) Electron in blob frame moves against the electric field; (b) ion-neutral collision in lab frame. The electrons lose energy to the electric field. The ions lose energy to the neutrals, and are re-accelerated by the electric field. The end result is cooler electrons and faster neutrals. The gyro-radii are not to scale.

The energy lost by the electrons ends up in the neutrals, as outlined in Fig. 2-14. The electrons in (a) lose energy by drifting against the electric field, as discussed above. In (b) an ion-neutral charge transfer collision is presented. The neutral atom is approximately at rest initially, since it is much slower than the ion. When the charge transfer occurs, the ion and neutral switch roles. The fast neutral carries away the energy of the ion, and the 'new' ion is accelerated from rest by the electric field, as it begins its radial E×B drift. The energy lost by the electron is used to re-accelerate the ion. This process is precisely the process of the Pedersen current. In steady state, this Pedersen current of the ions balances the upward electron current. We estimate the energy lost per electron to be $\Delta T_e/\Delta t = \Delta T_e/(\Delta R/v_{\text{blob}}) \simeq 2500$ eV/s, where $v_{\text{blob}} = 880$ m/s and $\Delta T_e \simeq 1$ eV in $\Delta R \simeq 35$ cm. Meanwhile, the energy imparted to the neutrals by ions for a single ion is $\nu m_i v_{\text{blob}}^2/2 \simeq 1800$ eV/s, where we have used

$P_n = 2.1 \times 10^{-4}$ Torr, corresponding to $v_{\text{blob}} = 880$ m/s. Hence, the energy lost by the electrons, is comparable to the energy imparted to the neutrals by the ions.

Other notable results of the T_e measurements show that the front end of the blob is hotter than the back end by about a factor of 2, and that the temperature at high neutral pressure (4.4×10^{-4} Torr) is about 30% lower than at low pressure (1.1×10^{-4} Torr). Overall, the electron temperature for blobs at these pressures is in the range 1-3 eV.

2.6 Applications

The results of this Chapter are applicable to a range of plasmas. In the tokamak edge, the effect of the neutrals will be measurable if the drag is roughly 20% of the drive: $(\nu v_{\text{blob}})/(2c_s^2/R) \gtrsim 0.2$. For $v_{\text{blob}}/c_s \sim 0.05$ [83], $\bar{v}_i \sim c_s$, $R = 1$ m, and $\sigma \sim 4 \times 10^{-19}$ m^2 (for 20 eV deuterons [94]), the neutral drag will be important if $n_n \gtrsim\ 2 \times 10^{19}$ m^{-3}. Some fusion experiments (e.g. Alcator C-Mod) approach this neutral density in the scrape-off layer, and most exceed it in the divertor [84]. The blob speed in VTF (relative to the sound speed) is fast compared to tokamaks, probably because in tokamaks the rotational transform of the magnetic field, among other effects, drains curvature-induced currents; our experiments have only the effect of the neutrals.

The interaction of a propagating filament with a background of neutrals is important also for flux emergence through the photosphere into the corona. Although the propagation mechanism is different—the flux tubes are driven by magnetic buoyancy—the neutrals play an important role in dissipating cross-field currents. This dissipation creates force-free flux tubes, since only field-aligned currents survive the interaction with the neutrals [95]. Previous simulations had ignored the neutrals and missed this effect.

In magnetic reconnection with a guide magnetic field, flowing plasma filaments are ejected in the outflow region of the conventional x-line geometry. Moreover, in the photosphere, the neutral density is ∼3 orders of magnitude greater than the ion density [96]. The ionization fraction is similarly low in the interstellar medium

(ISM), where Zweibel [97] has shown that current sheets are likely to form. The precise mechanism and even the magnetic geometry of reconnection in the ISM, the photosphere and the chromosphere above it are not known, and hence the role of the neutrals is sometimes ignored for simplicity (e.g. [98]). However, as the results of this Chapter suggest, the neutrals are important in regulating the cross-field flow. Specifically, in the context of reconnection, the interaction of ions with a density gradient of neutrals may slow or distort the ejected plasma in the outflow region of reconnection, as it does in Fig. 2-13. If the outflow plasma is sufficiently nozzled, the reconnection rate may be significantly reduced. In addition, Zweibel [99] showed that in the presence of strong ion-neutral coupling—where the neutral and ion flows are identical—reconnection is significantly slowed, since the Alfvén speed is reduced due to the higher effective ion mass.

Chapter 3

Experimental Setup for Collisionless Reconnection Experiments

3.1 The Versatile Toroidal Facility

The experiments are conducted in the Versatile Toroidal Facility (VTF) at MIT. The device consists of a large toroidal vacuum chamber (major radius 1 m), and it has been used over the past 10 years for magnetic reconnection experiments with both 'open' [100] and 'closed' [101] magnetic configurations, as well as for blob propagation experiments [73]. The chamber is pumped by a 450 L/s Leybold turbo pump, with the exhaust of the turbo removed by a scroll pump. The scroll pump is also used directly on the chamber to pump down from atmospheric pressure. The base vacuum in VTF is typically $2{\times}10^{-6}$ Torr. A residual gas analyzer shows that this base pressure is due mainly to water vapor and nitrogen. An ionization gauge is used to monitor the pressure below $\sim 1.5 \times 10^{-4}$ Torr.

A photograph of the device is shown in Fig. 3-1. The orange coils, which close through the hollow center of the torus, provide a toroidal magnetic field, which varies as inverse major radius. This toroidal field is the dominant magnetic field in the ex-

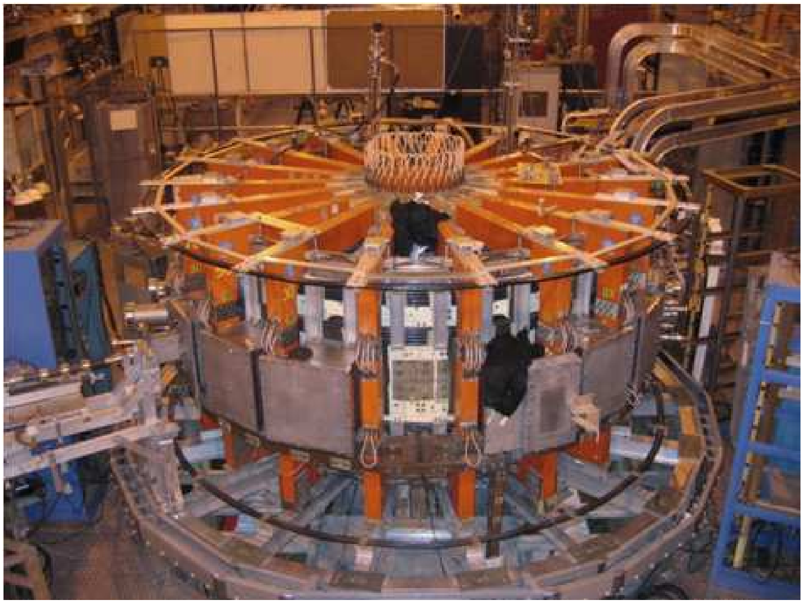

Figure 3-1: A photograph of VTF. The orange coils give a toroidal magnetic field, while the many side ports give excellent diagnostic access.

periment. Also visible in the photograph are many side ports, which provide excellent diagnostic access, as exemplified by the probe at left. Additional ports are located at the top and bottom of the facility. There is an electrical break in the chamber, seen in the middle of the photograph where a port is 'missing'. This break prevents toroidal currents from being induced in the chamber walls.

Fig. 3-2 shows a more detailed schematic of the experiment. The toroidal geometry is characterized by (R,φ,Z). There are 4 toroidal coils inside the vacuum chamber, and these provide the poloidal (R-Z) magnetic field shown at left. At $Z = 0$ there is a magnetic x-line, which is characteristic of magnetic reconnection studies. We use the orange coils mentioned above to apply a toroidal magnetic field $B_\varphi = B_0 R_0/R$ (where $B_0 =$ 50-75 mT and $R_0 = 1$ m), which is much larger than the poloidal field. The dominance of the toroidal field means that we are in the strong guide-field regime of magnetic reconnection.

To create the plasma, we leak into the vacuum chamber neutral argon gas at $P = 6 - 9 \times 10^{-5}$ Torr, corresponding to $n = 2 - 3 \times 10^{18}$ m^{-3} at room temperature. The ionization fraction obtained is roughly 30-50%, though possibly higher [102]. The use of argon, as opposed to lighter hydrogen or helium, slows down the plasma

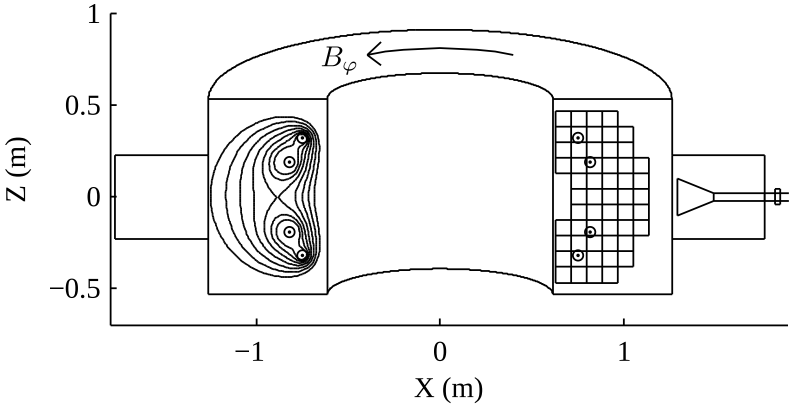

Figure 3-2: Half of the toroidal chamber; the 4 internal co-axial coils create the poloidal magnetic field lines shown at left. At right is one of the Rogowski arrays, and the microwave horn antenna. The magnetic field is dominated by B_φ.

dynamics sufficiently to improve the time resolution of the measurements. We create a seed plasma using 20 kW of 2.45 GHz microwaves amplified by a klystron, and injected through the horn shown in Fig. 3-2. The toroidal field is set to provide electron cyclotron resonance ($\omega_{\text{microwaves}} = eB(R)/m_e$) in the vacuum vessel. For $f = 2.45$ GHz microwaves, the resonant field is 87 mT; the condition that this value occur inside the vacuum chamber limits the range of toroidal fields for the experiment. Specifically, we require that

$$\frac{2\pi f m_e R_{\text{inner}}}{eR_0} < B_0 < \frac{2\pi f m_e R_{\text{outer}}}{eR_0} \tag{3.1}$$

where the inner and outer walls are located at $R_{\text{inner}} = 0.62$ m, and $R_{\text{outer}} = 1.26$ m, respectively. Therefore, the toroidal field is limited to 54 mT$< B_0 <$110 mT. A further constraint on B_0 is imposed by the power supply, which excludes fields above $B_0 \sim 90$ mT. These constraints apply to the first harmonic of electron cyclotron resonance. However, plasma breakdown is also possible using the second harmonic of the cyclotron frequency. This effect allows the breakdown of the seed plasma at fields as low as 27 mT, which explains how in previous experiments plasma was created at $B_0 = 44$ mT [101].

After 200 μs of microwaves, the klystron is switched off, and a central solenoid (see

Fig. 3-3) drives toroidal current in the seed plasma and builds up the plasma density from 10^{16} m^{-3} to 10^{18} m^{-3} levels. The plasma $\beta \equiv 2\mu_0 p/B^2$ is typically 10^{-3}. Table 3.1 summarizes some of the important plasma parameters during the spontaneous reconnection.

Parameter	Symbol	Value
Density	n	$\sim$ 1-2 $\times 10^{18}$ m^{-3}
Neutral argon density	n_0	2-3 $\times 10^{18}$ m^{-3}
Electron temperature	T_e	$\sim$ 10-20 eV
Ion temperature	T_i	$\lesssim$ 1eV
Spitzer resistivity	η_{sp}	$\sim$10-30 $\Omega\mu$m
Plasma β	$\beta \equiv \frac{2\mu_0 p}{B^2}$	$\sim 10^{-3}$
Toroidal magnetic field	B_{tor}	50-75 mT
Poloidal magnetic field	B_{pol}	0-6 mT
Ion cyclotron frequency	ω_{ci}	1.4×10^5 s^{-1}
Electron cyclotron frequency	ω_{ce}	1.1×10^{10} s^{-1}
Sound speed	c_s	6×10^3 m/s
Alfvén speed	$v_A \equiv \frac{B}{\sqrt{m_i n \mu_0}}$	2×10^5 m/s
Ion gyroradius	ρ_i	$\sim$ 1 cm
Electron gyroradius	ρ_e	150 μm
Debye length	λ_{de}	30 μm
Ion inertial length	d_i	1.4 m
Electron inertial length	d_e	5 mm
Ion sound gyroradius	$\rho_s \equiv \frac{c_s}{\omega_{ci}}$	4 cm
Electron-neutral mean free path	λ_{en}	5-10 m
Electron-ion mean free path	λ_{ei}	$\sim$ 3 m

Table 3.1: Some of the plasma parameters during spontaneous reconnection event.

The reconnection drive is shown schematically in Fig. 3-3. The central solenoid drives toroidal current not only in the plasma, but also in the outer shells of the four coaxial in-vessel coils. These shells are connected in series to force them to carry the same current. This toroidal current produces the magnetic geometry illustrated on the left of Fig. 3-2. It is emphasized that the applied reconnection drive is up-down symmetric and toroidally symmetric.

After the central solenoid has been active for 1.2 ms, the switch at the left of Fig. 3-3 is closed and current flows in the internal conductors of the four in-vessel coils. This current enhances the total current in coils 1 and 4, but decreases the

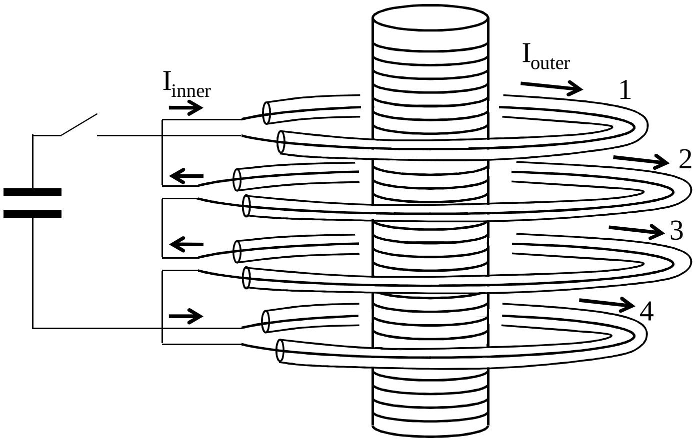

Figure 3-3: Reconnection drive scheme: the central solenoid induces clockwise current in the outer shells of the four co-axial conductors, connected in series (I_{outer}). Then the switch is closed and current is driven in the inner conductors, enhancing or detracting from I_{outer}. Overall, there is a net shift of current from coils 2 and 3 to 1 and 4. Consequently, the drive pulls magnetic flux away from the x-line (see Fig. 3-4).

total current in coils 2 and 3. The net effect is a sudden redistribution of the total coil current away from the midplane. Figure 3-4 shows schematically the response of the poloidal magnetic field lines; plasma is pushed into the x-line from the sides and pulled from the top and bottom. The reconnection drive tears magnetic flux away from the x-line. One might expect that only two in-vessel coils could have been used instead of four to tear flux from the x-line. However, with two coils, the strong guide field would be compressed as flux and frozen-in plasma would be pulled towards the coils. This compression would be energetically unfavorable and would oppose the reconnection drive. With four coils, there is an effective transfer of current from two coils to the other two and the guide field is therefore not compressed.

The current in the in-vessel coils is plotted as a function of time in Fig. 3-5a; the vertical line represents the time at which current is redistributed from the inner two coils to the outer two. (b) shows the total plasma current, integrated over the poloidal cross-section; its magnitude is similar to that of the in-vessel coil currents. In (c) we see the plasma density build up from the seed plasma by ohmic heating due to the growing plasma current, which is induced by the central solenoid. The spontaneous reconnection event occurs around $t = 1.4$ ms.

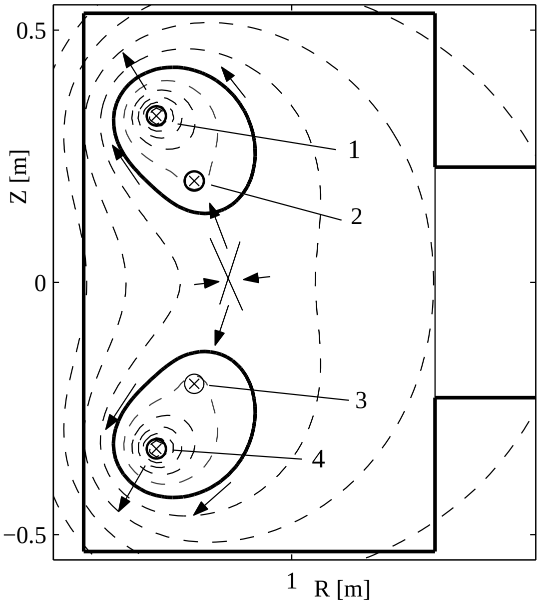

Figure 3-4: Poloidal cross-section of VTF, showing internal coils; the redistribution of current from coils 2 and 3 to coils 1 and 4 causes the poloidal magnetic field lines (dashed) to move into the x-line from the sides and away from the x-line at the top and bottom.

3.2 Diagnostics

We use multiple arrays of magnetic, Langmuir, and Rogowski probes to characterize the full 3D dynamics of the reconnection process. Table 3.2 summarizes the various diagnostics, which are described in detail in this section. Although it is possible that these diagnostics perturb the plasma, we note that as each array is added, the reconnection dynamics remain qualitatively the same.

The materials used in probe construction include Kapton- or HML-coated copper wires, Teflon tubes, aluminum hardware, Torr Seal, G-10 rods, and ceramic rods. These materials have withstood thousands of plasma discharges with no sign of degradation. This is probably due to the short duration of the VTF plasmas, which is only about 10 ms. The Langmuir stainless steel probe tips do get affected by repeated exposure to the plasma, but they can be treated by glow discharge cleaning, as will be described below.

To bring the wires out of the vacuum chamber, we use home-made, specially

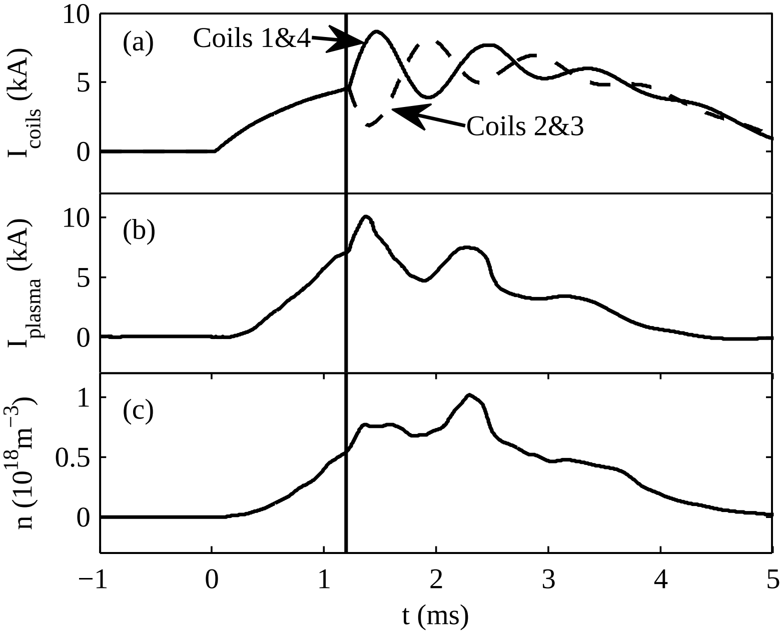

Figure 3-5: (a) Current in the in-vessel coils; when the reconnection drive is switched on, current is transferred from coils 2&3 to 1&4; (b) plasma current integrated over the poloidal cross-section; (c) spatially-averaged plasma density.

designed feedthroughs in order to reduce cost and eliminate magnetic pickup noise at the chamber wall [103]. We drill small holes into a regular Conflat flange and feed bundles of twisted copper wires through. We then use Torr Seal to seal the holes; a heat gun is essential at this step to make the Torr Seal liquefy and wick into the holes. These home-made feedthroughs are able to withstand the base vacuum of VTF, which is typically 10^{-7}–10^{-6} Torr.

To digitize the signals from all of the arrays, we use ICS645B 2MHz single-ended digitizers sold commercially by the Radstone Corporation (now GE) and ACQ196 500kHz digitizers sold by D-tAcq Solutions, Ltd. Altogether, we measure more than 1000 signals during each shot.

3.2.1 Langmuir Arrays

We use Langmuir probe arrays to measure the density and floating potential in the plasma. These include four medium-resolution Langmuir arrays, and one high-resolution array. The arrays are installed around the torus at different toroidal angles.

Diagnostic	Quantity Measured	Where	$\Delta R \times \Delta Z$ (cm^2)
Langmuir arrays	$n(R,Z)$, $V_{\text{floating}}(R,Z)$	4 toroidal angles	7×5
	$n(R,Z)$	1 toroidal angle	1.5×3.5
Magnetic arrays	$A_\varphi(R,Z)$	2 toroidal angles	3×3.5
	$A_\varphi(R,Z=0)$	6 toroidal angles	3×0
	$A_\varphi(R,Z)$	Attached onto the high-resolution Langmuir array	1.5×3.5
Rogowski arrays	$J(R,Z)$	2 toroidal angles	8.5×8.5
Microwave interferometer	$\int n(R_0,Z)dZ$	1 toroidal angle	
16-tip Langmuir probes	T_e	2 toroidal angles, each at 4 locations near x-line	
Fast camera	Visible light	Looking at x-line from side port	

Table 3.2: Summary of diagnostics for VTF plasmas. J: current density; n: plasma density; V_{floating}: floating potential; A: magnetic vector potential; T_e: electron temperature. The final column contains measurement resolution, i.e. probe separation in R and Z.

The probes in each medium-resolution array have a spacing of $\Delta R \times \Delta Z = 7$ cm $\times$ 5 cm, and they are used in a checkerboard fashion, such that half the probes are biased to ion saturation (density) and half are floating (potential). The high resolution Langmuir array has probe spacing of $\Delta R \times \Delta Z = 1.5$ cm $\times$ 3.5 cm.

The Langmuir array design is shown in Fig. 3-6. We use Kapton- and HML-coated 4 mil copper wires (red lines) soldered onto stainless steel cylinders (at blue dot). At left of (a), the wires are run through a Teflon tube, while the newer design (right) uses a mixture of Torr Seal and ethanol to hold the wires together without the bulkier Teflon tube. The diameter of the probe tips is 1.3 mm, and for the glued wires 0.5 mm. The debye length, in comparison, is only 30 μm. A photograph (Fig. 3-6b) shows the newer design.

The Langmuir probes can be operated in biased or floating mode and the plasma is modeled differently in each case. In floating mode, the plasma can be thought of as a voltage source with output impedance R_p. In biased mode, however, the plasma can be modeled as a current source with large output impedance. Both cases can be

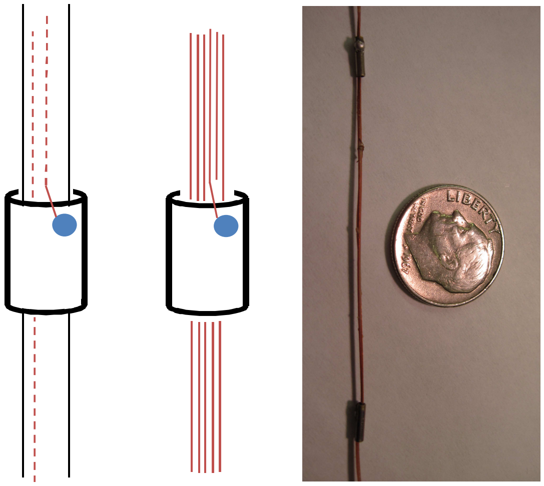

(a) (b)

Figure 3-6: (a) Two versions of Langmuir array design. Left: cylindrical probe on Teflon tube, with wires running through Teflon and soldered onto probe (blue dot). Right: wires glued with Torr Seal reduce the cross-sectional area of Teflon-based array. A 6 mil guide wire provides mechanical strength to the 3-4 mil signal wires. (b) Photograph of two probes without Teflon tube.

described by the I-V characteristic ([104])

$$I(V_{\text{bias}}) = neA_p c_s \left[\frac{1}{2} \left(\frac{m_i}{2\pi m_e} \right)^{1/2} \exp\left(\frac{e(V_{\text{bias}} - V_p)}{T_e} \right) - \exp\left(-\frac{1}{2} \right) \right], \tag{3.2}$$

where $c_s = \sqrt{T_e/m_i}$ is the sound speed, n is the plasma density, A_p is the probe surface area, V_{bias} is the probe voltage, and V_p is the plasma potential. The first term on the right-hand side represents the electron current to the probe, while the second term is the ion current. The electron response can be understood by considering the flux of electrons from the main plasma to the probe. In the main plasma, the electron velocity distribution is assumed to be Maxwellian with temperature T_e. The probe is assumed to be biased negatively relative to the plasma potential, and most electrons are therefore reflected. Only electrons whose velocity in the direction of the probe v_y is larger than the cutoff velocity $v_c = \sqrt{2e(V_p - V_{\text{bias}})/m_e}$ are able to reach the probe. The flux of electrons to the probe Γ can then be written

$$\begin{aligned} \frac{\Gamma}{n} &= \frac{\int dv_x \int dv_z \int_{v_c}^{\infty} dv_y v_y \exp\left(-\frac{mv^2}{2T_e}\right)}{\int dv_x \int dv_z \int_{-\infty}^{\infty} dv_y \exp\left(-\frac{mv^2}{2T_e}\right)} \\ &= \sqrt{\frac{T_e}{2\pi m_e}} \exp\left(\frac{e(V_{\text{bias}} - V_p)}{T_e}\right). \end{aligned} \tag{3.3}$$

This expression is equivalent to $\Gamma = n\bar{v}/4$, which is predicted by kinetic theory [104], multiplied by a Boltzmann factor. The mean velocity for a Maxwellian plasma is given by $\bar{v} \equiv \sqrt{8T_e/(\pi m_e)}$. Given Eq. 3.3, we calculate the electron current to the probe as

$$I_e = e\Gamma \times \text{Area} = n_p e \frac{A_p}{2} \sqrt{\frac{T_e}{2\pi m_e}}, \tag{3.4}$$

which is equivalent to the electron term in Eq. 3.2. The probe area A_p is divided by a factor of 2 because of the small ratio of the electron gyroradius to the probe dimension. The well-magnetized electrons see the projection of the probe onto a 2D plane, which for a cylindrical probe is $A_p/2$.

The second term on the right-hand-side of Eq. 3.2 represents the ion current to the probe. The potential difference between the probe and the plasma is confined to within a few debye lengths ($\lambda_{de} = \sqrt{\epsilon_0 T_e/(ne^2)}$) of the probe. In this region—called the 'sheath'—the ions are accelerated by the potential difference. Outside the sheath, the plasma is quasineutral and $n_e = n_i$. It turns out that the ion velocity for $V_{\text{bias}} < V_p$ does not depend on the bias voltage, and saturates at approximately the sound speed c_s [104]. If the probe is much larger than the debye length, the so called ion-saturation current can be shown to be

$$I_i = -neA_p c_s \exp\left(-\frac{1}{2}\right). \tag{3.5}$$

If the electron temperature is known, the ion saturation current provides a measure of the plasma density. For these experiments, we assume $T_e = 15$ eV and bias the probes to -90 V in order to measure the density.

There are several sources of uncertainty in the density measurement. First, there may be variations in the electron temperature; however, for a typical variation between 10 and 20 eV, the square root dependence on T_e gives a variation in I_i of only 41%. Second, if the debye length is not small enough compared to the probe size, sheath expansion can effectively enhance the probe area. This effective area then depends on the bias voltage of the probe, and the ion saturation current does not saturate. If the $V_{\text{bias}} - V_p$ is fixed, the sheath expansion could be absorbed into A_p, but if the plasma potential changes in time and space, the sheath expansion could affect the measurement of I_i. If the sheath expands, for example, by $2\lambda_{de}$, the ion saturation current would change by $\Delta I_i/I_i \sim \Delta A_p/A_p \sim 2\lambda_{de}/r_{\text{probe}} \sim 2 \times 30\ \mu\text{m}/1\ \text{mm} \sim 6\%$. A more serious problem arises during the spontaneous reconnection, when the plasma potential can swing by up to 80V, causing some electrons to be absorbed by the negatively-biased probe. In extreme cases, the electron current is larger than the ion current, and the plasma density appears to be negative. Caution must be used therefore when the plasma potential (or the floating potential) show large variation.

The floating potential—at which ion and electron currents to the probe balance—can be computed from Eq. 3.2 as

$$V(I = 0) = V_p - \frac{T_e}{2e}\left(1 + \log \frac{m_i}{2\pi m_e}\right) \tag{3.6}$$

which for Argon ($m_i \approx 40 \times m_{\text{proton}}$) is $V_p - 5.2T_e/e$. Here, the sheath area has been assumed equal to the probe area. If the electron temperature is spatially uniform and constant, we can use the floating potential as a proxy for the plasma potential. This is done because the floating potential is much easier to measure.

The output impedance of the plasma when the probes are in floating mode, R_p, can also be calculated from Eq. 3.2. This impedance is given by the differential resistance of the I-V characteristic at $I = 0$: $R_p = dV/dI|_{I=0} = T_e/(eI_i)$. For $n = 10^{18}\ \text{m}^{-3}$, $R_p \sim 500\ \Omega$, while for $n = 10^{17}\ \text{m}^{-3}$, $R_p \sim 5\ \text{k}\Omega$.

Figure 3-7 shows the circuits used for floating and biased probe operation. Subfigure (a) shows the floating potential V_f and output impedance of the plasma R_p, the capacitance of the wires, C_s, which is about 50 pF, and the divider resistors R_1

and R_2. The voltage across R_2 is digitized at 500 kHz or 2 MHz. Several considerations affect the choice of R_1. Since R_p varies depending on the plasma density, it is desirable that $R_1 \gg R_p$ so that R_p can be ignored in the divider ratio. Thus, we choose $R_1 = 330$ kΩ. The capacitance C_s in combination with R_p is a low-pass filter with time constant $R_pC_s \sim 2.5 \times 10^{-7}$ s for $n = 10^{17}$ m^{-3}. This filter is therefore negligible for our digitization rates, except at very low densities where R_p is large.

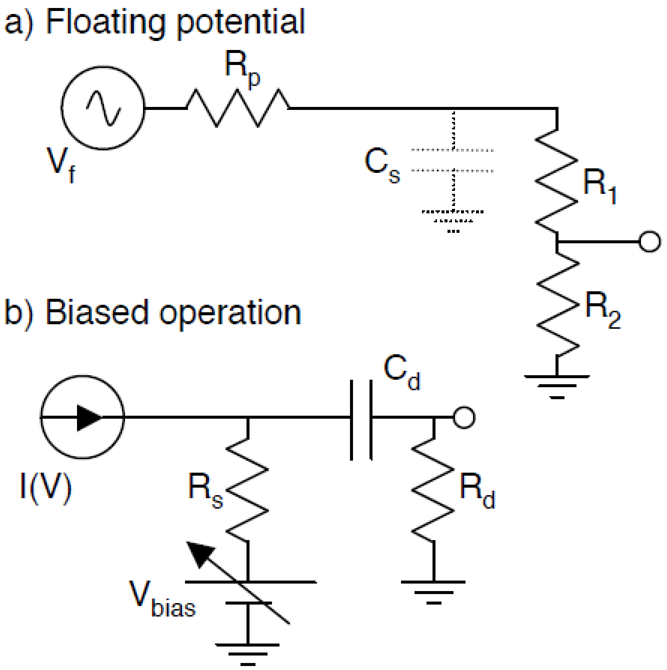

Figure 3-7: Circuits for Langmuir probe measurements. Reproduced from Ref. [102].

In the biased probe operation (Fig. 3-7b), the plasma acts like a current source. This is especially true when the probe is biased to ion saturation, where the differential resistance dV/dI (the output impedance) becomes large. To bias the probe to ion saturation, we apply $V_{\text{bias}} \sim -90$ V and measure the probe current through a small sense resistor R_s, typically 300-600 Ω. The voltage across the resistor is passed through a decoupling capacitor C_d and digitized across R_d. The capacitor serves to protect the digitizers from the large DC bias voltage, while passing through the time-dependent plasma signal. Since the plasma only lasts ~ 10 ms, we require that $R_dC_d \gg 10$ ms, so that this high-pass filter lets through all signals of interest. We choose $C_d = 10$ μF, which is also small enough that R_dC_d is much smaller than the time between discharges, and the capacitor has enough time to charge up to V_{bias}. The decoupling resistor R_d is chosen to be much larger than the sense resistor so that all current goes through the sense resistor.

With the many-channel probe arrays, the bias voltage is supplemented by a large capacitor (5 mF) in parallel, which serves as a repository of charge and effectively decreases the output impedance of the bias power supply. This capacitor prevents the bias voltage from drooping during the shot.

The Langmuir probes suffer from surface contamination. Over several months to a year, the stainless steel surface becomes darker, covered by a brown-tinged layer. The layer effectively adds an extra resistance between the probe and the plasma, and when it is thick enough, ion saturation current decreases sharply. Before this total failure of the probes, signs of contamination emerge from measurements of the I-V characteristic. In normal operation, in order to map out the characteristic in reproducible discharges, the probe bias is scanned as the current is recorded. As the probe surface becomes contaminated, hysteresis is observed depending on whether the bias voltage is incrementally increased or decreased [88, 89]. In Section 2.2, we discuss this problem in more detail.

To clean the contaminated probe surfaces, we use glow discharge cleaning. According to Ref. [105], an dose of 10^{22}–10^{23} ions/m^2 is sufficient to clean stainless steel surfaces. We use 100 mTorr of argon and bias the Langmuir probes to about -160V. We use large metallic tubes for electrodes, and bias these to 200-300V. Since the chamber wall is grounded, the negative bias on the probes ensures that the probes are cleaned instead of the wall. After $\sim$ 10 hours, which is sufficient for the recommended ion dose, the current to the probes increases and the surface layer is eliminated.

3.2.2 Magnetic Arrays

Two magnetic arrays [103] are used to measure the toroidal inductive electric field, $\partial A_\varphi / \partial t$, and the poloidal component of the magnetic field. A schematic of these arrays is shown in Fig. 3-8. The vertical component of the magnetic field is measured in each row, but the radial component is only measured in the central column. In this way, fewer signals have to be digitized simultaneously. $\partial A_\varphi/\partial t$ is computed by integrating

$$\begin{aligned}\Delta_R(R\dot{A}_\varphi) &= \int_{R_2}^{R_1} R\dot{B}_Z dR \\ \Delta_Z(R\dot{A}_\varphi) &= -R\int_{Z_2}^{Z_1} \dot{B}_R dZ,\end{aligned} \tag{3.7}$$

where $\dot{A}_\varphi$ and $\partial A_\varphi/\partial t$ are used interchangeably. The time integration of $\dot{\mathbf{B}}$ is done digitally, after the measurement. The reference point for the integral is taken as $R = 0$, and the contribution to RA_φ from $R = 0$ to the nearest loop on the array is computed using a toroidal loop at the inner wall (the extra flux from the inner wall to the inner-most edge of the array is measured by the nearest single-row magnetic array, mentioned below). The resolution of the magnetic arrays is $\Delta R \times \Delta Z = 3$ cm × 3.5 cm. The high resolution Langmuir array mentioned above also has a small magnetic array lined up with the Langmuir probes. Its resolution is $\Delta R \times \Delta Z = 1.5$ cm × 3.5 cm. While Eq. 3.7 is exact when the plasma is toroidally symmetric, in the more general case of 3D plasma response, the equation is only approximate. However, in Appendix A it is shown that the error in $\partial A_\varphi/\partial t$, which is measured by a magnetic array at one toroidal angle, is at most 2%. The approximation relies on the large aspect ratio of VTF and the strong guide field.

To measure the toroidal asymmetry in the reconnection rate, we use 6 single-row magnetic arrays spread evenly ($\Delta\varphi = 60°$) around the torus at $Z = 0$. Each array consists of one row of loops spanning from the inner wall to the outer wall. By measuring $\dot{B}_z(R) \equiv \partial B_z(R)/\partial t$, the reconnection rate at $Z = 0$ is found from integrating $\dot{A}_\varphi(R) = V_{\text{inner}}/(2\pi R) + (1/R)\int_{R_{\text{inner}}}^{R} R'\dot{B}_z dR'$, where V_{inner} is the induced loop voltage measured at the inner wall. These magnetic arrays are useful for measuring the reconnection rate at the mid-plane ($Z = 0$) throughout the torus, and we will use them in Chapter 5 to determine the onset angle of spontaneous magnetic reconnection.

Before the magnetic signals are digitized, they are passed through differential amplifiers with a gain of 1 (see Fig. 3-9). Since the digitizers are single-ended, the amplifiers are necessary to reduce electrostatic noise from the plasma, which presumably

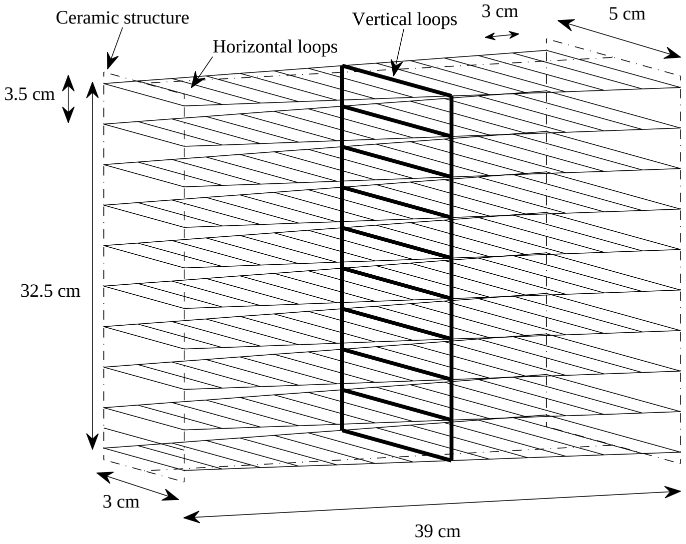

Figure 3-8: Schematic of magnetic array. Reproduced from [103].

affects both wires in the twisted pair equally and is therefore a common-mode signal. The circuit was designed to reduce the common-mode signal by more than 1/100. The good common-mode rejection is due to the resistors R_2 in the figure, which divide down the input to prevent the common-mode from saturating the op-amp. The use of amplifiers allows the use of cheaper single-ended digitizers, as opposed to differential ones, which are more expensive.

Some optimization is required when choosing the input resistance of the amplifiers, R_{in} [103]. The electrostatic noise of the plasma can couple to the wires capacitively through their Kapton/HML coating. A typical value for this capacitance is $C_p \sim 10$ pF, and the noise is filtered by the combination of this capacitance and the input resistance of the amplifier. For electrostatic fluctuations with characteristic angular frequency ω, the noise signal is reduced by a factor of $\sim R_{\text{in}}/(R_{\text{in}} + (i\omega C_p)^{-1})$. For this factor to be small—and the transmitted noise small—we require $\omega R_{\text{in}} C_p \ll 1$.

Another consideration which affects the choice of input resistance involves the self-inductance of the wires, L. This self-inductance, of order $L \sim 10^{-6}$ H, in combination with the input resistance of the amplifiers can filter the probe signal, reducing the signal-to-noise ratio. For electrostatic fluctuations with characteristic angular frequency ω, the probe signal is reduced by a factor of $\sim R_{\text{in}}/(R_{\text{in}} + i\omega L)$. For this

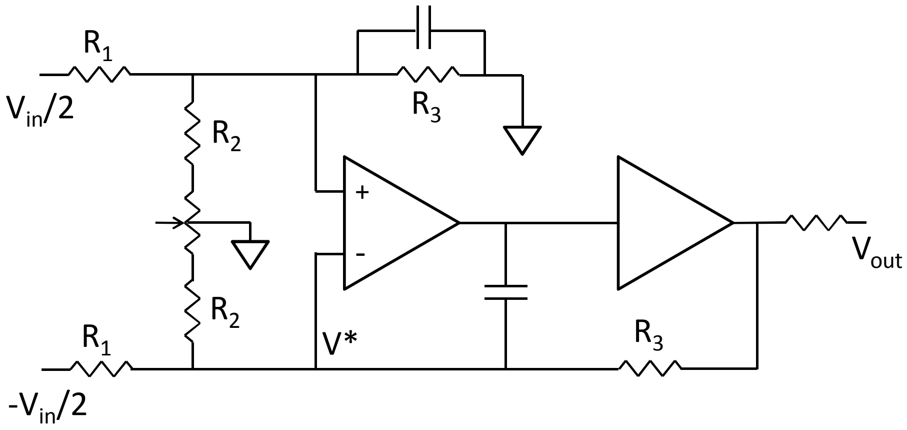

Figure 3-9: Amplifier circuit for magnetic and Rogowski arrays. To get a sense for the circuit, consider current continuity in the upper part of the circuit $(V_{\text{in}}/2)/R_1 = V^*/(R_1||R_2||R_3)$. Meanwhile, in the lower part of the circuit $V_{\text{out}}/R_3 - (V_{\text{in}}/2)/R_1 = V^*/(R_1||R_2||R_3)$. Combining these two relationships yields the gain $V_{\text{out}}/V_{\text{in}} = R_3/R_1$.

factor to be close to 1, we require that $\omega L/R_{\text{in}} \ll 1$.

The signal-to-noise ratio is worse for large ω. Since our digitizers operate at 2MHz, we take the fastest ω of interest to be of order 1MHz. Then the capacitive noise coupling condition implies $R_{\text{in}} \ll 20$ kΩ, while the self-inductance condition implies $R_{\text{in}} \gg 10\Omega$. We therefore choose a value of $R_{\text{in}} = 1$ kΩ. The capacitively coupled electrostatic noise is then reduced by $\omega R_{\text{in}} C_p \sim 1/20$. A further reduction in noise results from the common-mode rejection ratio of the amplifiers, which is better than 1/100. At lower frequencies the signal-to-noise ratio improves further. Another consideration when choosing R_{in} is that it be large enough to prevent dividing the probe signal down due to the wire resistance, which is typically $\sim 30\ \Omega$. The chosen value of 1 kΩ satisfies this condition as well.

A source of systematic error in the magnetic probe signals is the extra magnetic pickup from the central solenoid and reconnection drive. This pickup occurs in the cable that leads from the vacuum feedthrough to the digitizers, and is relatively reproducible. To eliminate it, we record a plasma discharge with the magnetic signals shorted just after the feedthrough. The shorted signals are then subtracted from the signals during an un-shorted discharge. We find that this method successfully eliminates magnetic pickup in the cables.

The loop dimensions are accurate to within about 2 mm [103], but some of these inaccuracies can be calibrated against the known vacuum magnetic fields of the in-vessel coils. Overall, the accuracy in RA_φ is about 2%. This uncertainty does not account for the extra uncertainty due to toroidal asymmetry, which is discussed in Appendix A.

3.2.3 Rogowski Arrays

To accurately measure the current density 2 Rogowski arrays have been constructed, which measure the current density in a poloidal cross-section. Although it is possible to find J_φ from $\nabla^2 A_\varphi$, which is measured by the magnetic arrays, the derivatives involved in this measurement may introduce error. The Rogowski arrays avoid this problem. One of the arrays is shown in Fig. 3-2 at right, and an individual probe is shown in Fig. 3-10. Each square probe is mounted on a grid of G-10 rods. One array is fixed toroidally, while a second array is moved between different toroidal locations. The spatial resolution of these measurements is 8.5 cm in both R and Z.

To calibrate the Rogowski arrays we use the current in the in-vessel coils. Given the capacitance of the bank supplying this current and the voltage across the capacitors before discharge, we calculate the total charge released. The time-integrated signal from the Rogowski probe is then equated to this charge to find the correct calibration factor. The individual Rogowski probes are assumed to be identical to the two calibrated ones. This is a good approximation since the number of windings of the copper wire in each probe is determined only by the diameter of these closely-packed wires.

The choice of resistors in the Rogowski probe circuit is motivated by similar consideration to those applied in the magnetic probe circuits. However, the capacitance between the probe and the plasma, C_p, is larger, and the self inductance of the probe, L, is no longer negligible. The capacitance is estimated from the cross-sectional area of the probe and the HML coating thickness of the copper wires ($\sim 40\ \mu$m) to be $C_p \sim 200$ pF. We require that the input impedance of the amplifiers be $R \ll 1/(\omega C_p)$,

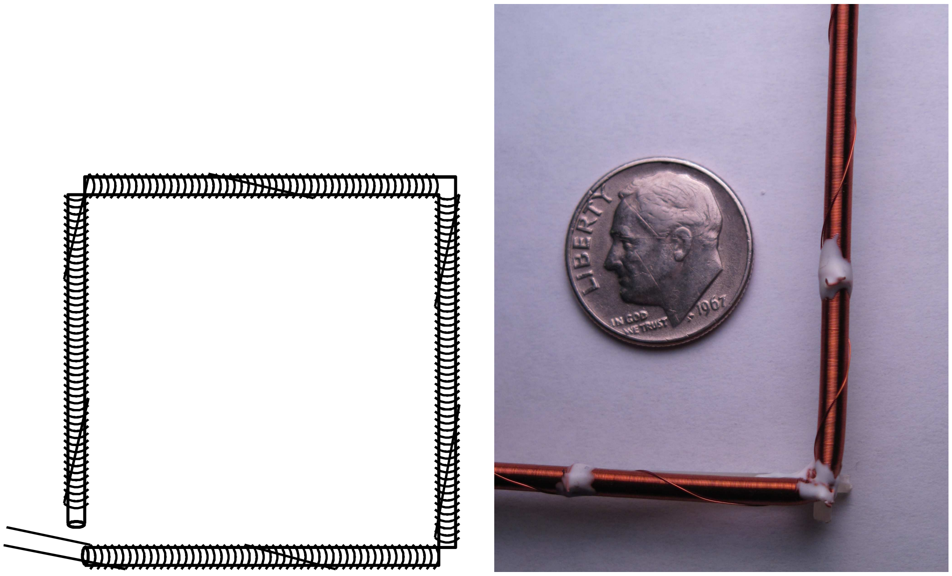

(a) (b)

Figure 3-10: (a) Schematic of Rogowski probe. Each square consists of 4-6 mil copper wire wound on Teflon tube. The squares are mounted on a G-10 grid, shown in Fig. 3-2. (b) Photograph of Rogowski probe corner.

in order for electrostatic noise to be minimally coupled to the probe. For $\omega \sim 10^6$ s^{-1}, this condition is $R \ll 5$ kΩ. Since we use the same amplifier circuits as for the magnetic probes with 1 kΩ input impedance, we add a resistor $R_1 = 140\ \Omega$ by the chamber wall, as shown in Fig. 3-11.

However, we also require that the divider ratio of the Rogowski signal (see Fig. 3-11) be close to 1, to prevent filtering. This ratio is approximately $R_1/(R_1 + i\omega L)$. The solenoidal probe's self inductance is estimated as 1.4×10^{-4} H. The condition that $R_1 \gg \omega L$ is then satisfied for $\omega \sim 10^5\ \mathrm{s}^{-1}$, but not necessarily for $\omega \sim 10^6\ \mathrm{s}^{-1}$. So fluctuations in the current density signals are filtered for short time-scales, but the noise is sufficiently reduced. The common-mode rejection of the amplifiers further suppresses the noise.

The systematic error of magnetic pickup in the cables between the chamber wall and the amplifiers, which affected the magnetic arrays, also affects the Rogowski signals. To remove this spurious signal, a discharge is recorded in which the seed plasma is absent. Since there is no plasma current in this false discharge, the recorded signals represent magnetic pickup. The signals resulting from this vacuum 'discharge'

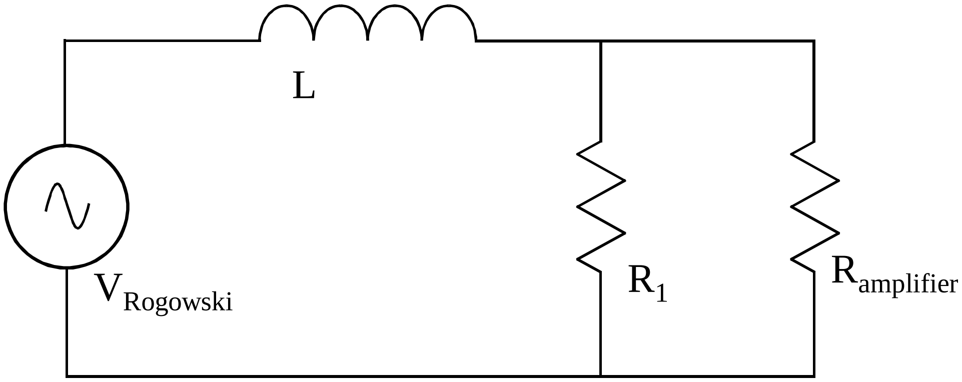

Figure 3-11: Schematic of circuit for Rogowski probes. A small R_1 is added to increase the filtering of capacitively coupled noise from the plasma. However, R_1 must be large enough to prevent the self-inductance of the probe from affecting the signal filtering.

are recorded and subtracted from the actual plasma signals.

3.2.4 Microwave Interferometer

To confirm the Langmuir density measurements, we use a homodyne microwave interferometer. Our source is a mechanically tuned Gunn oscillator from WiseWave Technologies, Inc., operating at 70 GHz. We use a single horn antenna and a reflecting mirror to measure interference fringes. This simple interferometer compares well with Langmuir probe data for early times when the density is building up, but past $n \sim 5 \times 10^{17}$ m^{-3}, the fringes disappear, most likely because of fluctuations in the line-integrated density. Nevertheless, the Langmuir measurements are well-calibrated using this interferometer.

3.2.5 Multi-Tip Langmuir Probe for Electron Temperature Measurement

We measure the electron temperature by recording the current collected by multiple Langmuir probes biased to different voltages. This measurement is done in a single shot. The 16 Langmuir probes, which are shown in Fig. 3-12 are arranged on a grid of dimensions 1 cm × 1 cm, and the bias order is scrambled to avoid systematic errors.

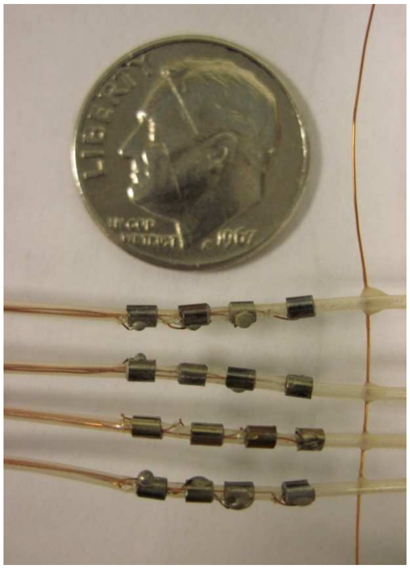

Figure 3-12: 16-tipped Langmuir probe for measuring the I-V characteristic and hence the electron temperature; the bias voltages of the probes are not in order.

The probe tips are cylindrical and are held on a thin Teflon tube, similar to the design in Fig. 3-6. There are 8 such point-measurements of the electron temperature near the x-line, at two separate toroidal angles. All measurements may be recorded in a single discharge.

3.2.6 Fast Camera

We use a fast Phantom v7.1 camera made by Vision Research to record visible light. The camera looks in from a side port at the x-line. The images recorded in these experiments have a resolution of 600×300 pixels and a frame rate of about 12 kHz. The line-integrated nature of these observations limits the quantitative use for the results, but, as will be discussed in Section 4.3, the qualitative results show plasma filamentation.

Chapter 4

Reconnection Results

In this chapter, we show that the spontaneous reconnection is not described by resistive MHD. Specifically, neither the ions nor the neutral atoms in the vacuum vessel provide sufficient resistivity to account for the fast reconnection observed. The role of the neutrals has been more fully investigated in dedicated experiments on the propagation of plasma filaments. These experiments are discussed in Chapter 2. The present chapter proceeds to describe the details of the plasma response during spontaneous magnetic reconnection.

4.1 The Neutral and Spitzer Resistivities

We now show that the reconnection is ‘fast’; that is, not described by resistive MHD. In resistive MHD, electron acceleration due to the parallel electric field at the x-line is balanced by collisional damping, either by ions or by neutral atoms. Stated another way, the toroidal (parallel) electric field at the x-line is completely balanced by the $\eta J_{\parallel}$ term in Eq. 1.5. We calculate the resistivity due to neutral argon atoms and electron-ion collisions and show that these resistivities are insufficient to balance the electric field.

To calculate the effect of the neutrals, we find the Lorentz resistivity, which treats the electron-neutral collisions by ignoring electron-electron and electron-ion collisions. The Lorentz resistivity represents a lower bound on the actual resistivity which includes all interactions. From Eq. VIII-2.14 in Ref. [106], we have

$$(\eta_n^{\mathrm{Lor}})^{-1} = \sigma^{\mathrm{Lor}} = \frac{4\pi}{3}\frac{n_e e^2}{m_e}\int_0^\infty \frac{c^3}{\nu_{en}}\left(-\frac{\partial f_0}{\partial c}\right)dc \tag{4.1}$$

where f_0 is the unperturbed electron distribution function, and the electron-neutral collision frequency is given by $\nu_{en} = n_n \sigma_{en}^m(c)c$, where

$$\sigma_{en}^m(c) = \int (1-\cos\chi) I_{en}(c,\chi)d\Omega \tag{4.2}$$

is the momentum transfer cross-section (Eq. VIII-2.10 and VII-6.25 in Ref. [106]), I_{en} is the differential cross-section, and χ is the scattering angle. Using a Maxwellian distribution function for the unperturbed f_0, and leaving the momentum cross-section unintegrated, we find

$$\sigma_n^{\mathrm{Lor}} = \frac{1}{3}\sqrt{\frac{8}{\pi}}\frac{n}{n_n}\frac{e^2}{m_e}\sqrt{\frac{m_e}{T_e}}\left\langle\frac{1}{\sigma_{en}^m}\right\rangle \tag{4.3}$$

where n is the plasma density, n_n is the neutral argon density, and

$$\left\langle\frac{1}{\sigma_{en}^m}\right\rangle = \int_0^\infty \frac{(\frac{\epsilon}{T})e^{-(\epsilon/T)}d(\frac{\epsilon}{T})}{\sigma_{en}^m(\epsilon)}. \tag{4.4}$$

Equation 4.3 can be explained up to a factor of order unity by a simple estimate: if electron collisions with neutrals provide the drag that opposes the accelerating electric field then $\nu_{en}v_e \sim eE/m_e$. Since $J \sim nev_e$ (assuming stationary ions), then $\eta_n = E/J \sim \nu_{en}m_e/(ne^2)$. Then, with $\nu_{en} \sim n_n\sigma_{en}v_{te}$, where $v_{te} = \sqrt{T_e/m_e}$ is the electron thermal speed and σ_{en} the electron-neutral collision cross-section, we have

$$\eta_n \sim \frac{n_n}{n}\frac{m_e}{e^2}\sqrt{\frac{T_e}{m_e}}\sigma_{en}, \tag{4.5}$$

which is reminiscent of the inverse of Eq. 4.3.

Meanwhile, the Spitzer resistivity [107, 108] is given by

$$\eta_{\mathrm{Spitzer}}^{\|} = \frac{\sqrt{2m_e}Z_{\mathrm{eff}}^2 e^2 \log\Lambda}{12\pi^{3/2}\epsilon_0^2 T_e^{3/2}} \tag{4.6}$$

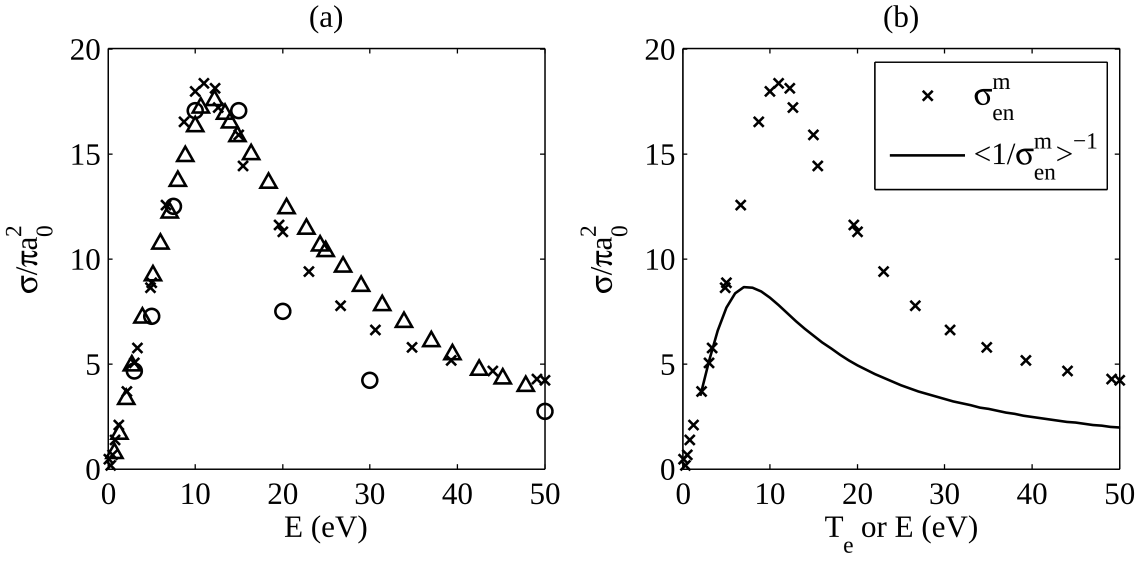

Figure 4-1: (a) Momentum transfer cross-section for electrons impinging on neutral argon (σ^m_{en}) from Mitchner *et al.* [106] (△), Srivastava *et al.* [109] (○), and Dasgupta *et al.* [110] (×). (b) Data from Dasgupta repeated, and result of integral in Eq. 4.4 based on this data. The uncertainty in σ^m_{en} is 20-30% [109].

where $Z_{\text{eff}} \equiv \Sigma_i n_i Z_i^2/\Sigma_j n_j Z_j$ is the effective ion charge (i,j index the different ion species), and $\log\Lambda$ is the coulomb logarithm, approximated by $\log\Lambda \approx 24 - \log\left(\sqrt{n}/T_e\right)$ [27]. For VTF discharges, $\log\Lambda \approx$ 12-13.

Figure 4-1 shows data for the momentum transfer cross-section of electrons impinging on neutral argon atoms. We use several sources for the cross-section data, and the variation among these sources reflects the typical error estimated in [109] to be 20-30%. We choose the data from Dasgupta *et al.* [110] since it extends to $E = 0$ and its values are between the other two references in magnitude. We then use Eq. 4.4 to calculate $\langle 1/\sigma^m_{en}\rangle$ for different electron temperatures. The result is shown in (b) of the figure. If we assume an electron temperature of 15 eV, this sets the integrated cross-section as $6\pi a_0^2$, where a_0 is the Bohr radius.

The neutral and Spitzer resistivities can now be compared to $(\partial A_\varphi/\partial t)/J$ at the x-line, and this comparison is shown in Fig. 4-2. The Spitzer resistivity is plotted in black, while the sum of the Spitzer and neutral resistivities, using the inverse of Eq. 4.3 ($\eta_n = 1/\sigma_n^{\text{Lor}}$) is plotted in blue. We assume $Z_{\text{eff}} = 1$, and $T_e = 15$ eV. The Spitzer and neutral resistivities are much too small to explain the spike of fast

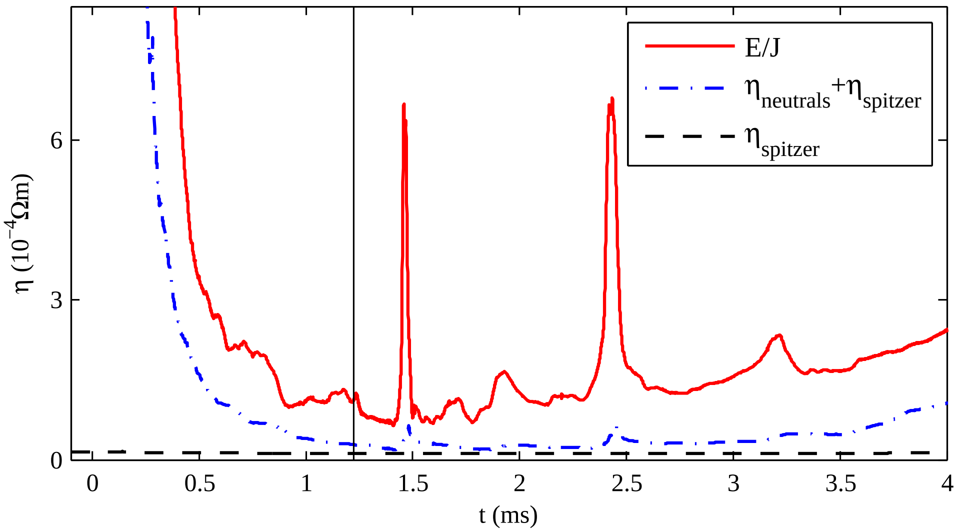

Figure 4-2: $(\partial A_\varphi/\partial t)/J$ is qualitatively consistent with the sum of neutral and Spitzer resistivities at early times, but not during the spontaneous reconnection at $t \sim 1.4$ ms. The vertical line represents the start of the reconnection drive.

reconnection at $t \sim 1.4$ ms (red). The reconnection electric field in the ratio E/J has been toroidally averaged to exclude the electrostatic component of E (see Chapter 5). Although the sum of the neutral and Spitzer resistivities is smaller than the $(\partial A_\varphi/\partial t)/J$ trace, the sum qualitatively reproduces the baseline value of the trace and its behavior at early times. Note that the second spike in E/J is large since the current density is small there (Fig. 4-4b).

To further evaluate the role of the neutrals in Ohm's law, we record several discharges while varying the neutral pressure in the chamber; the results are shown in Fig. 4-3. No spontaneous reconnection events occurred during these discharges. As before, while the magnitude of the resistivity is lower than expected from $(\partial A_\varphi/\partial t)/J$, there is qualitative agreement. Specifically, as the fill pressure in the vacuum vessel is decreased, both $\eta_{\text{Spitzer}} + \eta_{\text{neutrals}}$ and $(\partial A_\varphi/\partial t)/J$ decrease, since fewer neutral collisions result in lower resistivity. The data at the lowest pressure ($P_{\text{fill}} = 0.042$ mTorr) appears to contradict this trend; however, it is possible that a small background of neutrals was injected with the seed plasma, since in these discharges only, a plasma gun is used instead of electron cyclotron resonant heating to initiate the plasma. This background of neutrals may be comparable to the lowest fill pressure in Fig. 4-3.

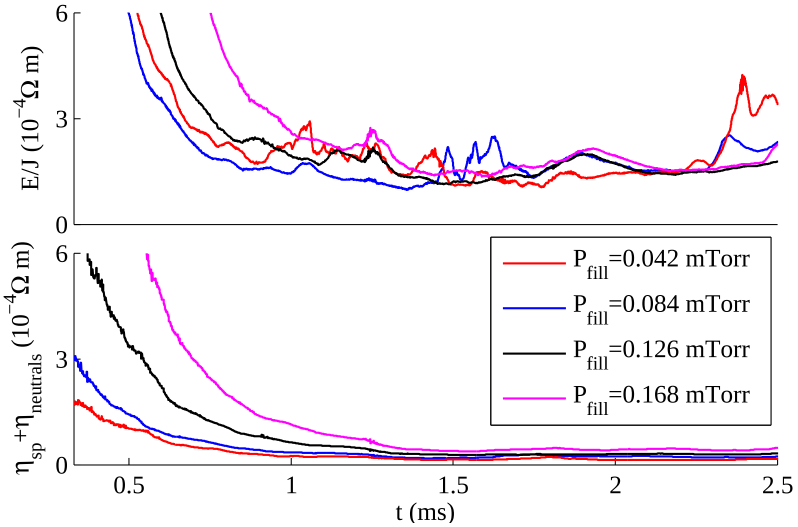

Figure 4-3: Top: E/J; bottom: η from density measurements. As the fill pressure is decreased, both E/J and the total resistivity decrease. However, the curve with $P_{\text{fill}} = 0.168$ mTorr does not follow this trend, and the magnitude does not match between the top and bottom sub-figures.

For $t > 1$ ms, Fig. 4-3 shows that the ratio of $(\partial A_\varphi/\partial t)/J$ decreases with time and then saturates. In addition, the saturated value does not depend on the fill pressure within the measurement errors, which can be estimated from the fluctuations in the figure. As discussed by Fox [102], the saturation may involve the neutral or Spitzer resistivities. If it is the neutral resistivity that is saturating, then the ratio of n_n/n reaches a constant (Eq. 4.3). However, Fox argues that this is unlikely since the ionization cross-section for electron-neutral collisions increases with plasma density, and this effect could lead to full ionization. In the absence of neutral resistivity, the saturated ratio of $(\partial A_\varphi/\partial t)/J$ would have to be balanced by Spitzer resistivity. This resistivity may be larger than shown in Fig. 4-2 if $Z_{\text{eff}} > 1$; that is, if some of the argon ions are multiply-ionized. The first three ionization energies of argon are 15.8 eV, 27.6 eV, and 40.7 eV [111], so it is conceivable for a $T_e = 15$ eV plasma to have $Z_{\text{eff}} > 1$.

Despite the uncertainty regarding the saturation mechanism, it is clear that neither neutral resistivity nor Spitzer resistivity can balance the reconnection electric field at the x-line during spontaneous reconnection. Hence, since resistive MHD is unable to describe the balance of Ohm's law, we describe the spontaneous reconnection as 'fast'. We focus on this fast reconnection event for the remainder of the dissertation.

Although the neutral and Spitzer resistivities are too small to balance the reconnection electric field during the $\sim 20\ \mu$s of the spontaneous reconnection event, the plasma in this time interval cannot be termed completely collisionless. Rather, since thermal electrons travel about 10^6 m/s $\times$ 20 μs $\sim$ 20 m during the event, and the electron mean free path (Table 3.1) is only about 3 m, the reconnection is semi-collisionless.

4.2 Observation of Spontaneous Reconnection

When the current in the in-vessel coils is redistributed (Fig. 4-4a), the plasma current at the x-line increases to compensate for the shift in coil currents. This effect—which is due to Lenz's law—is shown in Fig. 4-4b. However, in some discharges, the plasma current then decreases sharply. This decrease is delayed by about 100-200 μs from the redistribution of coil currents, and it is accompanied by an increase in the toroidal inductive electric field $\partial A_\varphi/\partial t$ at the x-line (Fig. 4-4c). Because of the delay, we interpret this event as a burst of spontaneous magnetic reconnection. Figure 4-4b-c suggests that at the time of spontaneous reconnection the global plasma response is that of an inductor, i.e. that $E_\varphi \propto dJ_\varphi/dt$ (see Fig. 3-4 in Ref. [102]).

The spontaneous reconnection events on VTF have been explored by Egedal *et al.* [101] and the results from this Letter are now summarized. Figure 4-5 shows the various plasma parameters recorded at one toroidal location at various times during the reconnection event. The data in the figure is recorded during a single discharge. Rows 3-4 of Fig. 4-5 show the same quantities as does Fig. 4-4b-c. In the third row, the poloidal cross section of the toroidal current density is plotted with poloidal magnetic field lines superimposed. The current density is evaluated from the Laplacian of the magnetic data ($J_\varphi = -\nabla^2 A_\varphi/\mu_0$), since the Rogowski arrays had not yet been constructed. Row 3 shows a strong current channel developing at the x-line;

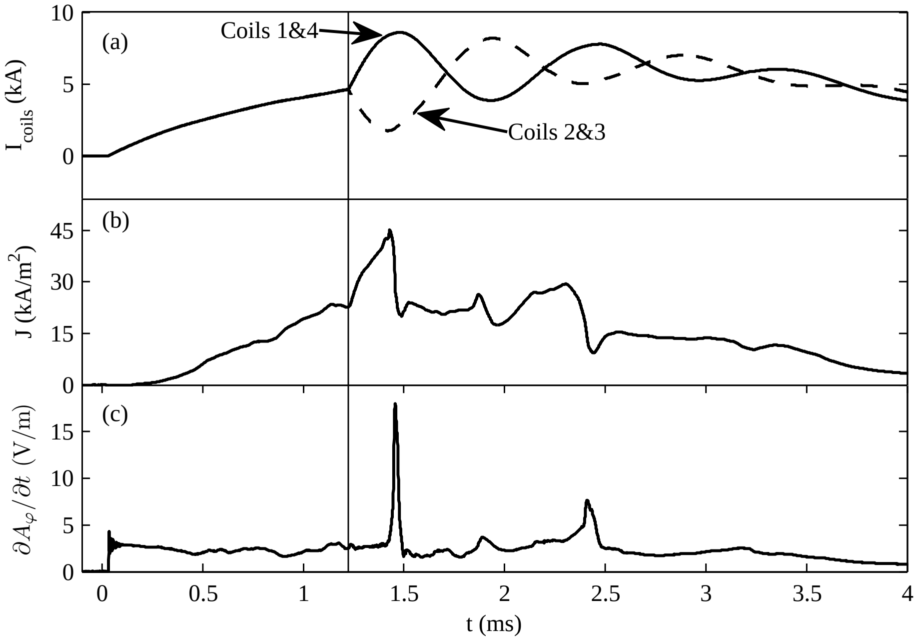

Figure 4-4: (a) Current in the in-vessel coils; (b) toroidal current density J at x-line; (c) toroidal inductive electric field $\partial A_\varphi/\partial t$ at x-line.

as the reconnection begins at $t = 80\ \mu s$, the current decreases, releasing its magnetic energy in the process. Reconnection is triggered when the current channel thickness is on the order of the ion sound gyro-radius $\rho_s = \sqrt{m_i T_e}/(eB) \sim 4$ cm, consistent with predictions by two-fluid models and numerical simulations with a strong guide field [57].

The fourth row shows the reconnection rate $\partial A_\varphi/\partial t$ recorded with one of the magnetic arrays mentioned in Chapter 3. A baseline level of slow reconnection is taking place, for example, at $t = 75\ \mu s$ (see also Fig. 4-4c), but then the reconnection rate increases suddenly to 14 V/m at the x-line for t = 80-90 μs, and spreads to the whole region surrounding the x-line as well. During this time, the field line highlighted in magenta breaks and reconnects in the outflow regions above and below the x-line. Eventually, by $t = 100\ \mu s$, the spontaneous reconnection is over and the rate returns to the baseline rate of 2–4 V/m.

The first row of Fig. 4-5 shows the plasma density in the full cross-section, while

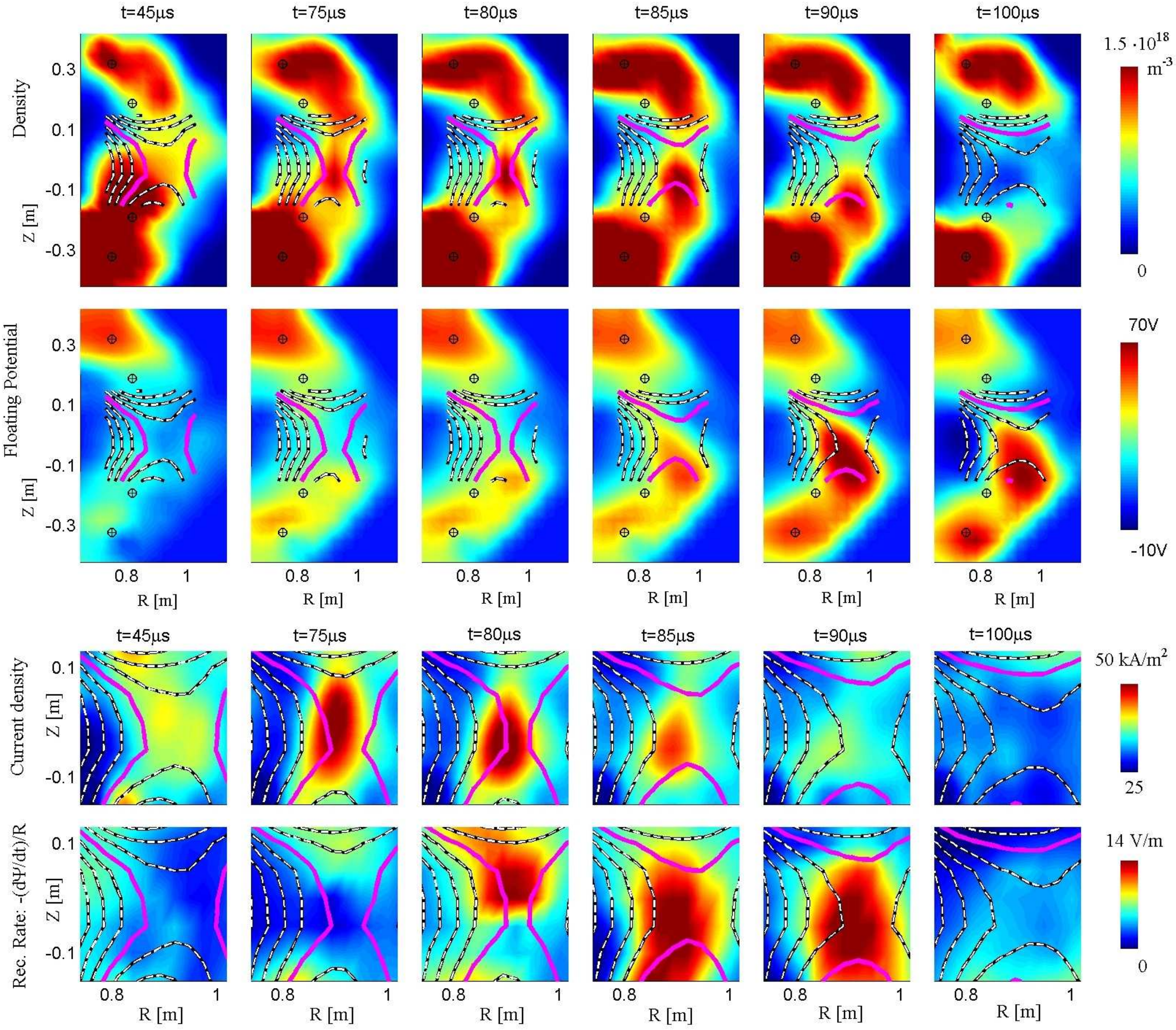

Figure 4-5: Plasma parameters recorded during a single discharge. First row: density; second row: floating potential; third row: current density from magnetic array; fourth row: reconnection rate $\partial A_{\varphi}/\partial t$; note that the time steps are unequal. Reproduced from Ref. [101].

the second row shows the floating potential measured with the Langmuir probe arrays during a single discharge. The plasma density is large near the in-vessel coils and at the x-line, where the induced toroidal current is large. Magnetic reconnection involves the release of magnetically stored energy, which is converted into particle heating and bulk flow energy. This conversion is evident in the density data, which shows how the central density is ejected downwards during the reconnection. The motion of the density filament is consistent with the motion of the highlighted field line and it is estimated to be about $v_{\text{out}} \sim 11$ km/s, corresponding to a flow energy per ion of $m_i v_{\text{out}}^2/2 \sim 24$ eV. We may also estimate this velocity from the floating potential data. To do this, we use the floating potential V_f shown in the second row to estimate the in-plane electric field. Since the plasma potential—with which the electric field should really be calculated—is $V_p = V_f + 5.2T_e/e$ (Eq. 3.6), we are assuming that the spatial variations in the electron temperature are small relative to the large floating potential variations (~ 80 V over 20 cm). We may then compute the radial electric field associated with the downward flow as ~ 80 V/20 cm= 400 V/m. In combination with the toroidal magnetic field in this discharge (44 mT), we get a downward $E \times B$ drift of ~ 9 km/s, which is consistent with the outflow speed v_{out} estimated above.

Figure 4-6 shows the change in the poloidal magnetic field which occurs as a result of the reconnection. The magnetic field shown is the vertical component measured at $Z = 0$ and it is therefore representative of the inflow region. The blue curve represents the magnetic field 10 μs before the reconnection, while the red curve shows the magnetic field 10 μs after the reconnection. The figure contains data from more than 20 discharges, and the results for B_z are very reproducible. The width of the plot line is chosen to be 1 standard deviation from the mean over discharges of B_z. The mean is shown in black in the figure. This measurement shows the relaxation of B_z associated with the disappearance of the current channel of Fig. 4-5. It is the energy released by this relaxation which is converted into the flow energy of the ejected density filament. Recall from Chapter 1 that in a low β plasma, if all the magnetic energy of the inflow is converted into flow energy (Eq. 1.8), the outflow velocity will be the he Alfvén velocity computed with the in-plane, upstream magnetic field $v_{A,\text{upstream}}$. From Fig. 4-6 we

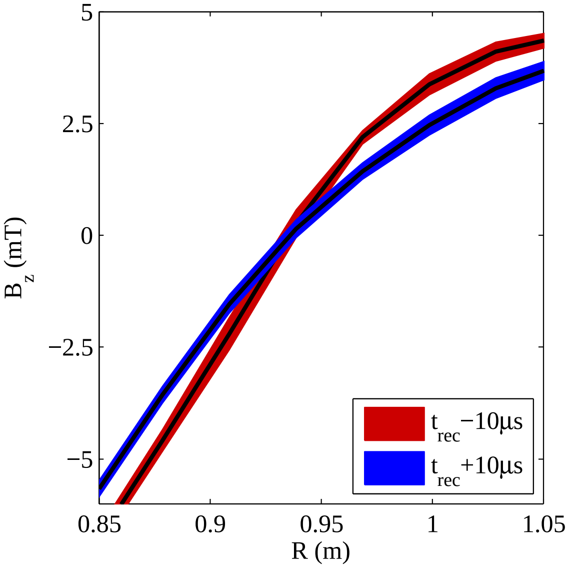

Figure 4-6: Reconnecting magnetic field B_z at the mid-plane ($Z = 0$), before (blue) and after (red) the spontaneous reconnection event. The bar of color around the line represents 1σ uncertainty.

estimate that $B_{z,\text{upstream}} = 4$ mT, which gives $v_{A,\text{upstream}} = B_{z,\text{upstream}}/\sqrt{\mu_0 m_i n} \sim 10$ km/s. This suggests that in this discharge, the outflow is Alfvénic.

In Ref. [101] a rough energy balance for the discharge in Fig. 4-5 is performed. The plasma at the x-line is modeled as a loop of current with self-inductance $L \sim 2\pi R \mu_0 \sim 6$ μH. The current lost during the reconnection event is approximately $I = 500$ A. Therefore the magnetic energy released is approximately $LI^2/2 \sim 0.8$ J. The fraction of this energy that is converted into plasma flow energy is calculated using the energy gained by each ion in the outflow $m_i v_{\text{out}}^2/2 \sim 24$ eV, the density $n \sim 2 \times 10^{18}$ m^{-3}, and the volume of plasma in the ejected filament $V \sim 2\pi R \times (0.1 \text{ m})^2$. The result is $nVm_i v_{\text{out}}^2/2 \sim 0.48$ J, which represents roughly 60% of the magnetic energy released. Other possible outlets for the released energy include ion and electron heating (see Section 4.3 below).

The reconnection event shown in Fig. 4-4 is typical of many of the discharges observed. However, the event is not observed on every shot. On some shots, the reconnection rate remains at its baseline level, while in others it is weaker than the 18 V/m of Fig. 4-4c. We focus in this dissertation on events stronger than ~ 14 V/m, since their reconnection is clearly ‘fast’, as will be shown in the next section.

4.3 Heating and Filamentation During Magnetic Reconnection

The electron temperature is measured with the 16-tip Langmuir probe discussed in Section 3.2.5. Each probe tip is biased to a different voltage and the full I-V characteristic is measured during a single discharge. The resulting electron temperatures are shown in Fig. 4-7a as a function of time. The temperatures were measured in many discharges and the data in (a) represent an average over many such measurements near the x-line. The error bars correspond to 1 standard deviation of these measurements from the mean. Within the measurement error, the electron temperature is toroidally symmetric, as would be expected from the fast equilibration of electrons along magnetic field lines ($\sqrt{T_e/m_e} = 10^6$ m/s).

Two typical I-V characteristics measured at the times shown by the dashed lines in (a) are shown in Fig. 4-7b. The electron temperature increases by about a factor of 2 during the reconnection, in accord with previous measurements by Fox [112] of the electron distribution tail, using a gridded energy analyzer. Egedal *et al.* [101] recorded a somewhat smaller temperature increase of 7 eV.

Errors in the temperature measurement could arise from the finite size over which the 16 probes are distributed (1 cm) and the filamentation which has been observed in the plasma density [112] with a scale size similar to that of the probe. Furthermore, the measurements may sample field lines that map away from the x-line and do not experience the electron acceleration. This last point accounts for the large spread in electron temperature during the reconnection event (Fig. 4-7a). Nevertheless, the electron heating is consistent with past results from VTF [101, 112].

As mentioned above, the plasma density is not uniform in the direction perpendicular to the magnetic field, and some filamentation is observed. This filamentation is shown in Fig. 4-8. The image in (a) is recorded with the fast camera discussed

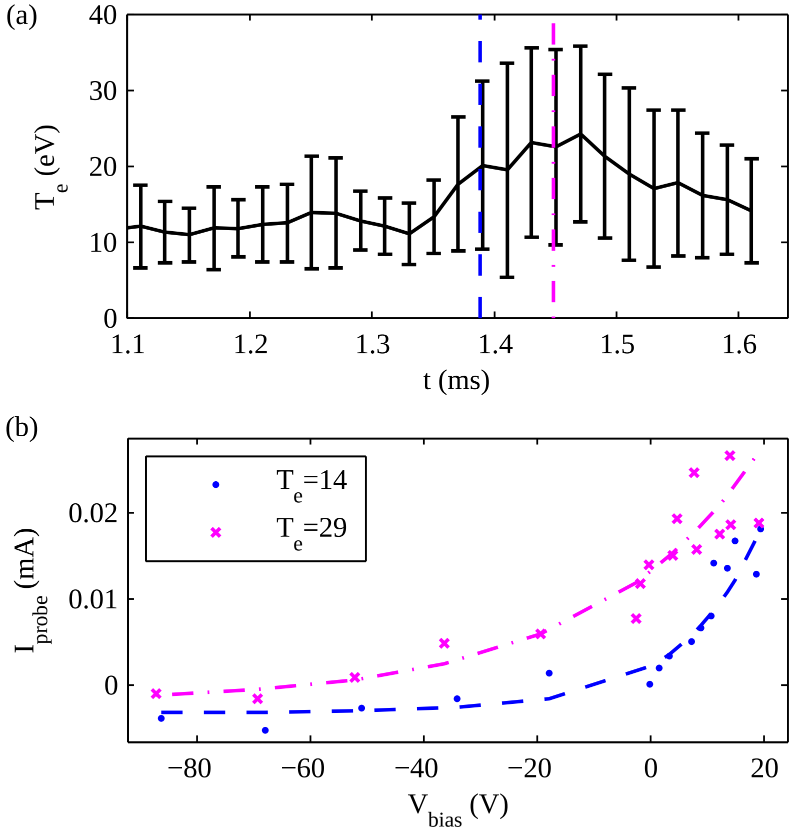

Figure 4-7: (a) electron temperature as a function of time, computed from the average of many discharges; error bars represent the standard deviation; (b) Two typical I-V characteristics measured before and during the reconnection; these times are indicated in (a).

in Section 3.2.6. The frame rate is 11.7kHz, and the exposure is 8 μs. The four in-vessel toroidal coils are at the top and bottom, with a vertical cable for support. Surrounding the coils are loops of plasma, the structures of which are aligned with the magnetic field. (b) shows the same plasma, but with more contrast: the frame in (a) was subtracted from the subsequent frame, and a spatial difference in R and Z was performed. Plasma filamentation is clearly visible.

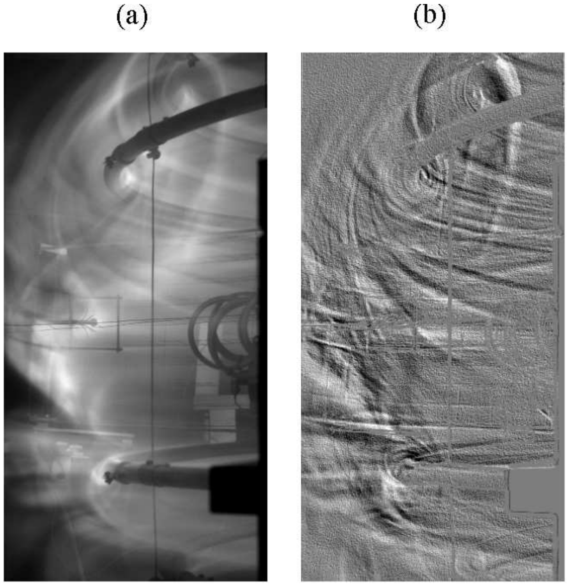

Figure 4-8: (a) Unfiltered light from the plasma just after reconnection drive has been turned on. Image was recorded with 8 μs exposure. Visible are the four in-vessel toroidal coils, several probes, and magnetic field-aligned, filamented structures. (b) Image modified to enhance plasma structures.

Chapter 5

Observation of 3D Effects in Reconnection Onset

In the previous chapter, we did not address whether toroidal symmetry characterizes the plasma dynamics. However, in this chapter, we will show that there are strong toroidal asymmetries in the plasma response. That is, despite the toroidal (2D) symmetry of the experimental geometry, the onset of spontaneous magnetic reconnection in VTF occurs in the presence of strong 3D effects [113].

5.1 Propagation of Toroidal Electric Field

Figure 5-1 shows the toroidal asymmetry in the plasma response for the time interval containing the reconnection event. In (a) the current density at the x-line is shown for two different toroidal angles separated by 120°. In (b), the reconnection rate at those same two angles is shown. The current density is measured by the Rogowski probe arrays (Section 3.2.3) and averaged over a $\Delta R \times \Delta Z$ =15 cm × 25 cm box around the x-line. The reconnection rate is measured at the x-line using the 6 rows of magnetic probes spread around the torus at $Z = 0$ (Section 3.2.2). It is clear that the decrease in the x-line current and the accompanying spike in reconnection rate occur at $\varphi = 40°$ about 5 μs before they are observed at $\varphi = 160°$. This asymmetry shows that the onset of reconnection is toroidally localized in VTF.

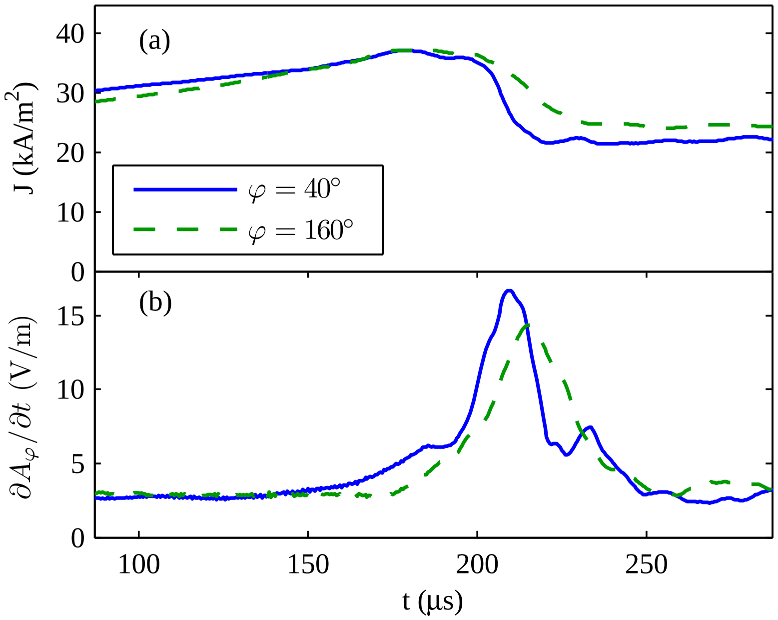

Figure 5-1: Zoom-in on time interval around reconnection event in Fig. 4-4b-c. (a) Current density at two toroidal locations, normalized to the same peak value to more clearly show the time delay; (b) reconnection rate corresponding to same toroidal locations. Both quantities are measured at the x-line. There is a delay of about 5 μs between the peaks in (a), indicating toroidal propagation.

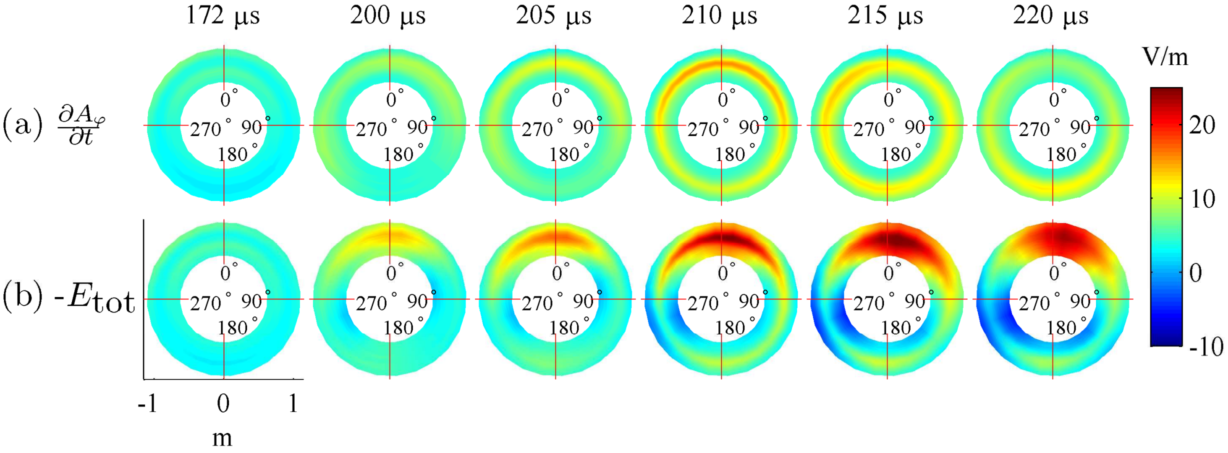

Figure 5-2: (a) $\partial A_\varphi/\partial t$ at $Z = 0$ viewed from above; reconnection onset occurs at $\varphi \simeq 0°$ and propagates to $\varphi \simeq 180°$ in about 5-10 μs. (b) Total electric field $\partial A_\varphi/\partial t + \nabla_\parallel \phi_x$ remains localized throughout. Time is relative to reconnection drive turn-on.

The onset of reconnection is shown in Fig. 5-2, where the reconnection rate $\partial A_\varphi/\partial t$ at $Z = 0$ is shown from above at multiple times. This data is measured with the rows of magnetic probes spread out among 6 toroidal angles. It is evident in (a) of the figure that after the toroidally localized onset, the reconnection propagates around the torus in both directions. The onset angle in this discharge is near $\varphi = 0°$. The data in (a) represent only the inductive component of the electric field, but since 2D symmetry is violated, the toroidal electrostatic field must be taken into account as well.

The sum of the inductive and electrostatic components of the electric field is shown in Fig. 5-2b, and we see that the total electric field remains localized throughout the event. The electrostatic component is computed using the floating potential measured at the x-line and denoted here by ϕ_x. We find it useful to split the potential measured by the Langmuir arrays into $\phi = \phi_x(\varphi) + \phi_{\text{in-plane}}(\mathbf{r})$, so that ϕ_x is poloidally uniform and $\phi_{\text{in-plane}}$ vanishes at the x-line.

The procedure for calculating ϕ_x is shown in Fig. 5-3. The floating potential measured with one of the Langmuir probe arrays is displayed in (a), with a box surrounding the x-line. The interesting mode structure that emerges will be discussed

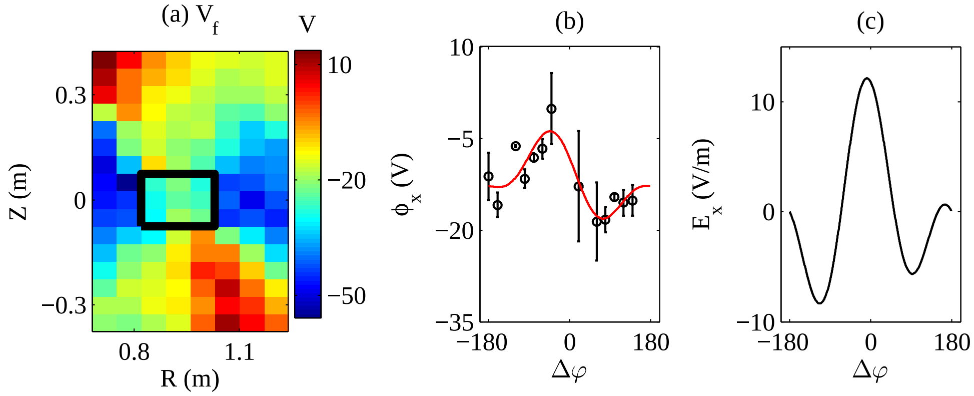

Figure 5-3: (a) Floating potential with box around x-line indicating region for calculating ϕ_x. (b) ϕ_x as a function of toroidal angle $\Delta\varphi = \varphi - \varphi_{\mathrm{onset}}$; error bars are computed as the standard deviation of ϕ_x values at each angle; fit line is constrained to be periodic and mixes first and second harmonics. (c) Negative gradient of fit in (b), representing toroidal electrostatic electric field at the x-line.

below. ϕ_x is computed from the mean of the potential within the box in (a), and the results, combining measurements from many discharges, are shown in (b) as a function of toroidal angle. The error bars represent one standard deviation from the mean computed at each toroidal angle. The red line in (b) represents the best fit, which is forced to be periodic and includes only the first two harmonics. The toroidal electric field E_x computed from this best fit (Fig. 5-3c) is largest at the angle of reconnection onset. This procedure to compute ϕ_x and E_x is repeated for each time sampled. In Fig. 5-2b, it is E_x that is added to $\partial A_\varphi/\partial t$.

The measurement of ϕ_x (and E_x) is subject to errors due to the uncertainty in the exact location of the x-line, and the resultant mixing in of the in-plane potential (see Fig. 5-3a). Furthermore, the strong electric fields at the x-line, $E_\varphi \gtrsim T_e/(eR)$ (Fig. 5-2), may cause toroidal electron trapping and hence toroidal temperature asymmetry during the reconnection event. Such a temperature asymmetry would prevent the use of floating potential as a proxy for the plasma potential (Eq. 3.6).

The measurements of ϕ_x in Fig. 5-3b use only a few fixed Langmuir arrays to map out the potential at many toroidal locations. This calculation is possible because the toroidal angle of reconnection onset varies from shot to shot. We use this observation, as well as data from many discharges, to construct full 3D measurements of the

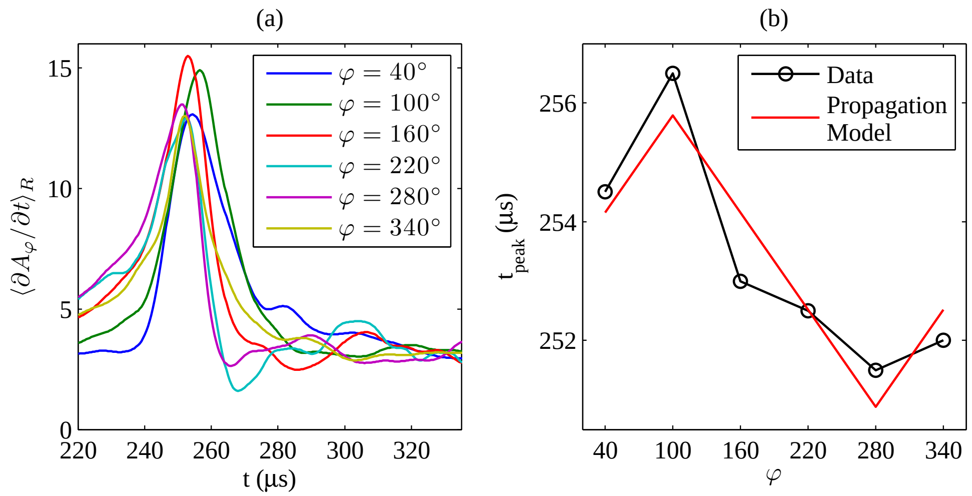

Figure 5-4: (a) Reconnection rate as a function of time at 6 toroidal angles, averaged over radius; (b) time of peak reconnection as a function of toroidal angle, with fit line representing the propagation model (red). The positive and negative slopes of the fit are constrained to be opposite and equal. The onset angle for this discharge is $\varphi = 280° \pm 30°$.

reconnection dynamics.

First, however, we must discuss how the onset angle is measured, a procedure which is shown for the typical discharge in Fig. 5-4. In (a), the reconnection rate is plotted as a function of time for the 6 toroidal angles where the rows of magnetic probes are located. The reconnection rate is averaged over radius and smoothed over 10 μs in time. It is evident that the peaks of the traces do not line up in time. The variation in peak time is plotted in (b) for each toroidal angle, and a line proportional to $|\varphi - \varphi_{\text{onset}}|$ is fit for each possible φ_{onset}. For simplicity the fit is chosen to be linear, and this choice gives reasonable agreement with the data. The line that fits best is used to determine the onset angle, which in the discharge in Fig. 5-4 is $\varphi_{\text{onset}} = 280° \pm 30°$. The uncertainty in onset angle is estimated as half the toroidal distance between neighboring magnetic row arrays. The fit assumes the same propagation velocity in both directions around the torus. Knowing the onset angle, we are now able to combine the data from multiple discharges while recording the relative toroidal angle between the probe arrays and the onset angle. We apply this knowledge towards diagnosing the plasma in full 3D.

Figure 5-5 shows the resulting 3D dataset of the toroidal inductive electric field $\partial A_\varphi/\partial t$. The values are found from averaging the inductive field at each angle over several discharges, with each $\partial A_\varphi/\partial t$ normalized to its shot's peak reconnection rate. The toroidal angle of each discharge has been shifted so that the reconnection onset occurs at $\varphi = 0^\circ \pm 30^\circ$. The reconnection rate peaks at this onset angle at $t = 210$ μs, and by $t = 218$ μs it has propagated to $\varphi = 160^\circ$ and $\varphi = 220^\circ$, on the other side of the torus. Superimposed on the reconnection rate are magnetic field lines projected onto the poloidal cross-section and also measured by the 2 magnetic arrays. One of the field lines at the cross-section near the onset angle is highlighted in gray. The cross-section near the reconnection onset is also the cross-section where the data in Fig. 4-5 is recorded. Another effect evident in Fig. 5-5 is that the x-line at $\varphi = 100^\circ$ moves downward by a few cm just before the onset.

Using many discharges, we determine the propagation time for the inductive electric field to reach the far side of the device (3 m away). This time is computed as shown in Fig. 5-4, using the difference between the times of maximum reconnection rate at φ_{onset} and $\varphi_{\text{onset}} + 180^\circ$. The average time is found to be 5 ± 3 μs; the uncertainty represents 1 standard deviation of the propagation times of the different discharges. This propagation is on the order of the Alfvén time ($\pi R/v_A \sim 15$ μs), although on this time-scale the ions are only marginally magnetized ($1/\omega_{ci} \sim 14$ μs).

The onset location is likely determined by small asymmetries in the in-vessel coils. This location is often the same in different discharges, but as shown in the present section there is also variation in the onset location. The VTF group is currently upgrading the device with new coils, with plans to carry out 'scans' in coil asymmetry and determine the effect of this asymmetry on the reconnection onset.

5.2 Poloidal Potential of the Mode

The reconnection event does not occur on every shot: it occurs only for discrete values of the toroidal magnetic field. Furthermore, when spontaneous reconnection does occur, it is accompanied by a global plasma mode. This mode is evident in

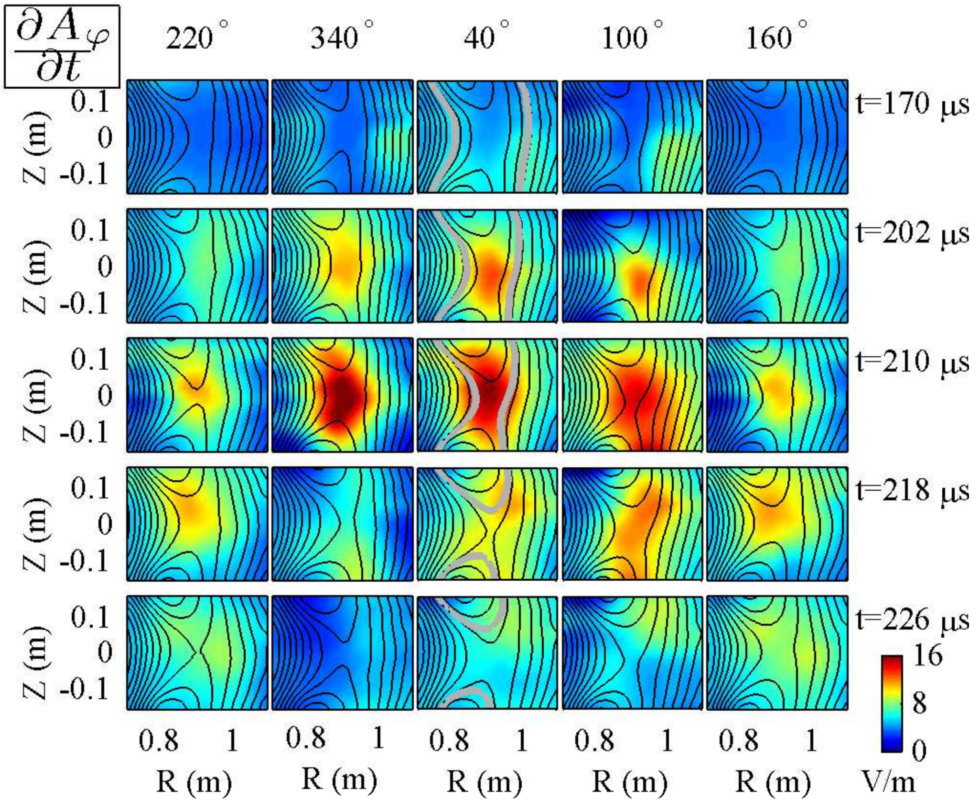

Figure 5-5: Poloidal cross-sections of $\partial A_\varphi/\partial t$ for different toroidal angles and times, averaged over several discharges. The onset angle is $\varphi = 0°$, and the peak reconnection rate occurs at $t = 210$ μs. Superimposed is the poloidal projection of magnetic field lines, one of which at $\varphi = 40°$ is followed in gray. By $t = 218$ μs, $\partial A_\varphi/\partial t$ has propagated to the far side of the torus ($\varphi = 160°$).

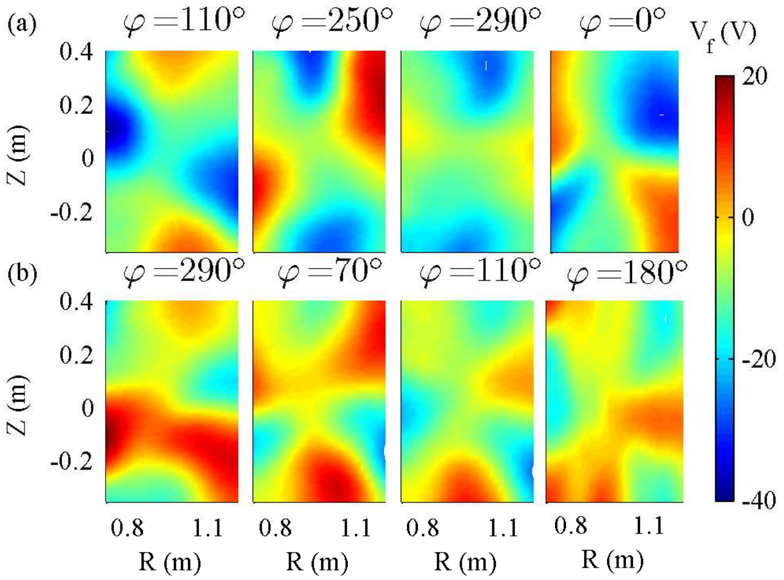

Figure 5-6: Floating potential at different toroidal angles for two shots during a reconnection event: (a) q=2 case with $B_0 = 56$ mT; (b) q=3 case with $B_0 = 72$ mT. The toroidal angles are shifted so that the onset occurs at $\varphi = 0$.

Fig. 5-6, which shows the floating potential for two discharges with different values of the toroidal magnetic field. In (a), $B_0 \equiv B_\varphi(R = 1\text{m}) = 56$ mT, while in (b), $B_0 = 72$ mT; spontaneous reconnection is observed only for these two values of the magnetic field[1]. The discrete values of toroidal field for which spontaneous reconnection is observed are linked to a condition involving the safety factor q, namely that q be rational over a large part of the poloidal cross-section. In this region, q varies slowly with radius.

q is a measure of the number of times a field line goes around toroidally for a single poloidal circuit. Specifically, along the field line we have

$$\frac{R d\varphi}{B_\varphi} = \frac{dR}{B_R} = \frac{dZ}{B_Z} = \frac{dl_{\text{pol}}}{B_{\text{pol}}} \tag{5.1}$$

---

[1] In Ref. [101], spontaneous reconnection in VTF was observed at $B_\varphi(R = 1\text{m}) = 44$ mT. The reason involves the earlier timing of the reconnection drive in that experiment. The plasma current—and therefore B_{poloidal}—was lower at the time of reconnection onset, so that $q \sim B_{\text{poloidal}}/B_\varphi$ was still rational. The plasma response in Ref. [101] is the same as the response to the $q = 2$ case described here.

where $dl_{\text{pol}} = \sqrt{dR^2 + dZ^2}$ and $B_{\text{pol}} = \sqrt{B_R^2 + B_Z^2}$. q is then given by

$$q \equiv \frac{\Delta\varphi}{2\pi} = \frac{1}{2\pi}\int \frac{B_\varphi dl_{\text{pol}}}{RB_{\text{pol}}} \tag{5.2}$$

where the integral follows the field line once around in the poloidal cross-section. When q is rational the field line returns to its starting point in a finite number of toroidal circuits.

The q profile for VTF is shown in Fig. 5-7 for a time just before the reconnection event; we compute q from the measured toroidal current density, which we approximate as toroidally symmetric for this calculation. Although, at the x-line, q is infinite (Fig. 5-7b) in most of the surrounding region, q is close to 2 (for the $B_0 = 56$ mT case). The rationality of q is required for the potential of the mode to develop, since away from the x-line the potential is field-aligned and must map onto itself in one toroidal circuit. In our experiment, both $q = 2$ ($B_0 = 56$ mT) and $q = 3$ ($B_0 = 72$ mT) were attainable, but we focus on the $q = 2$ case unless otherwise noted. Other expected values of q (such as 1 or 4) are not attainable due to the limited experimental range of the toroidal field. This range is set by the requirement that electron cyclotron motion ($eB_0/(m_e R) = 2\pi f$) be resonant with the $f = 2.45$ GHz microwaves inside the vacuum vessel (Section 3.1).

It may be surprising that the ratio of toroidal fields 56 mT/72 mT=1.3 is not 3/2, but this is most likely due to the fact that the toroidal current profile depends on the toroidal magnetic field. Evidence for this claim is shown below in Fig. 5-10 ($q = 2$) and Fig. 5-17 ($q = 3$). Since the toroidal current is different for $q = 2$ and $q = 3$, so is the poloidal magnetic field. In addition, the $q = 3$ reconnection occurs on average 25 ± 60 μs earlier than the $q = 2$ reconnection, and the poloidal field at this earlier time is slightly weaker. Therefore, since the poloidal fields are different for $q = 2$ and $q = 3$, the ratio of toroidal fields is not required to be 3/2.

A 3D dataset of the $q = 2$ potential is presented in Fig. 5-8, which shows poloidal cross-sections of ϕ for each toroidal angle and for several times near the reconnection onset. This dataset is constructed, as in Fig. 5-5, by using fixed Langmuir probe

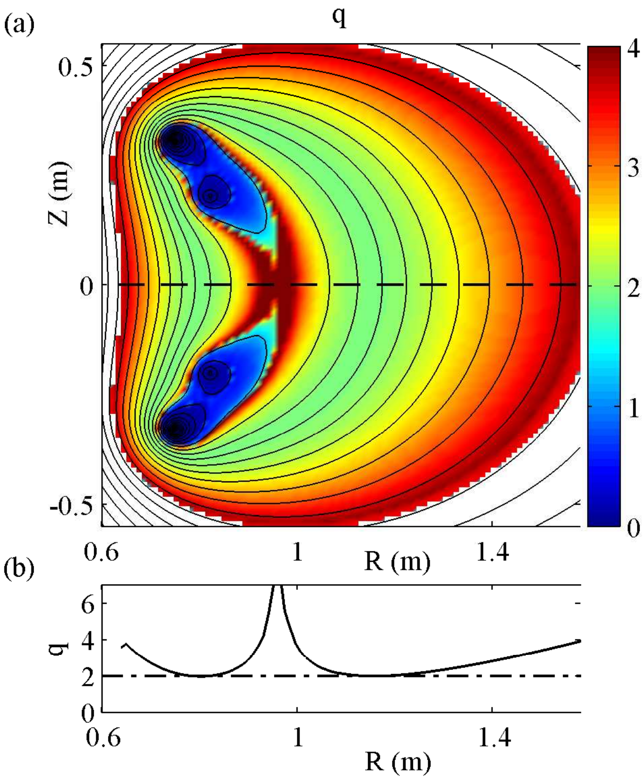

Figure 5-7: (a) q profile just before reconnection event, calculated from measured current density; (b) q at $Z = 0$; $q = 2$ over a large part of the poloidal cross-section.

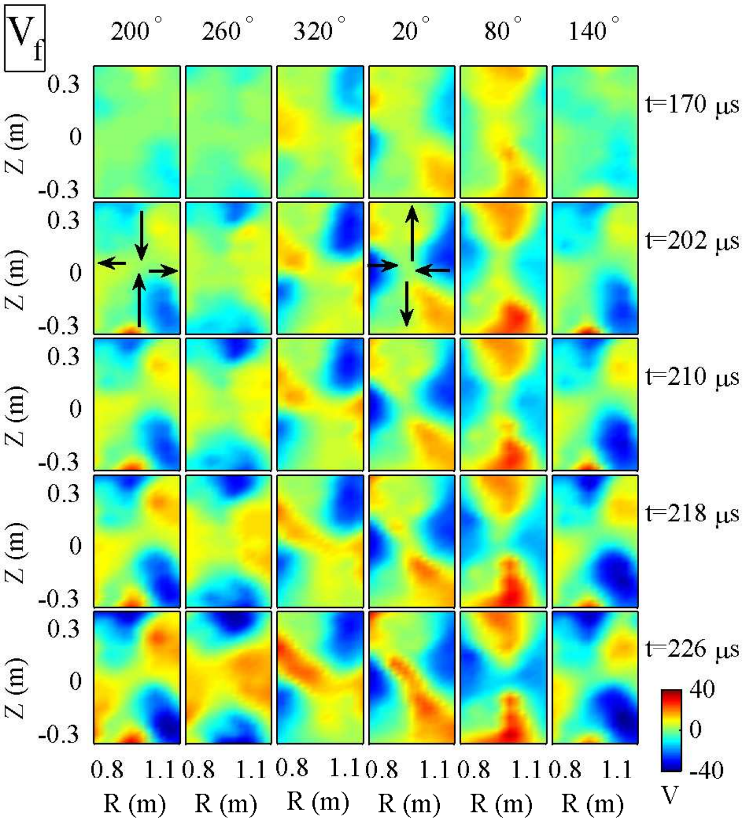

Figure 5-8: Poloidal cross-sections of floating potential for different toroidal angles and times. The black arrows indicate approximate E×B velocity.

arrays from many discharges with different onset angles. We subtract from ϕ the potential from a discharge with no reconnection event, in order to bring out the mode structure clearly. The $q = 2$ potential structure rotates with the magnetic field lines, counter-clockwise for decreasing φ. From the large floating potential of the mode, we may make observations regarding the in-plane electric field. Since the mode lasts at least 50 μs in the figure, while changing only in magnitude, the ions on this longer time-scale are magnetized and respond to the electric field with E×B velocity. This velocity points along contours of constant ϕ, and is shown schematically by black arrows at $t = 202$ μs.

At the location of onset, the E×B velocity matches the motion expected from the reconnection drive (Fig. 3-4), but since the potential structure rotates with the field lines, the E×B velocity arrows rotate as well. On the opposite side of the torus ($\varphi = 200°$) the E×B velocity arrows point opposite to the direction imposed by the reconnection drive.

The form of the potential away from the x-line can be approximated by $\phi \sim \log|Z/R|$, and this log form results from the constraint that $\mathbf{E}\cdot\mathbf{B} = 0$ away from the x-line [114]. To demonstrate this, we consider a more realistic form of the potential. We use the same log form, but rotated counter-clockwise by 45° and reduced in magnitude within $\delta \sim 3$ cm from the x-line, similar to the measured potential

$$\phi = \phi_0 \log\left|\frac{(Z-R)^2+\delta^2}{(Z+R)^2+\delta^2}\right|. \tag{5.3}$$

Figure 5-9 shows the measured potential at the onset location (a), as well as the modeled potential of this equation, normalized to the same amplitude (b). The magnetic field is modeled for simplicity as a linear cusp: $\mathbf{B}_{\text{poloidal}} = R\hat{Z} + Z\hat{R}$. Then $\mathbf{E}_{\text{poloidal}} \cdot \mathbf{B}_{\text{poloidal}}$ is poloidally uniform except along the separatrix (Fig. 5-9d), and can balance a toroidal electric field $E_\varphi B_\varphi$ away from the x-line (e). This toroidal component is plotted in (c); indeed, away from the x-line the toroidal part (c) and poloidal part (d) of $\mathbf{E}\cdot\mathbf{B}$ are approximately equal and opposite. The data is recorded 8 μs before the peak reconnection.

It is instructive to discuss this form of the potential in the context of previous experiments on VTF, which had a magnetic cusp with 'open' boundary conditions [114]. A dominant toroidal magnetic field was also applied, and the electrons followed trapped orbits, because of the boundary conditions [115]. In comparison, in the present experiments trapping is reduced since the magnetic field lines are 'closed' and electrons are able to circulate. In the open configuration, a potential structure similar to that in Fig. 5-9a extended around the torus without rotating, as did the reconnection electric field. Reconnection in the open configuration was toroidally symmetric. The electrostatic component of $E_\parallel$ balanced the inductive part away from the x-line, maintaining $\mathbf{E}\cdot\mathbf{B} \simeq 0$ as in Fig. 5-9c-e.

In the present, closed configuration, with a rotating potential, we find that a similar balance occurs at the onset angle. The phase of the mode relative to the poloidal magnetic field orientation is the same at both the onset angle and the open

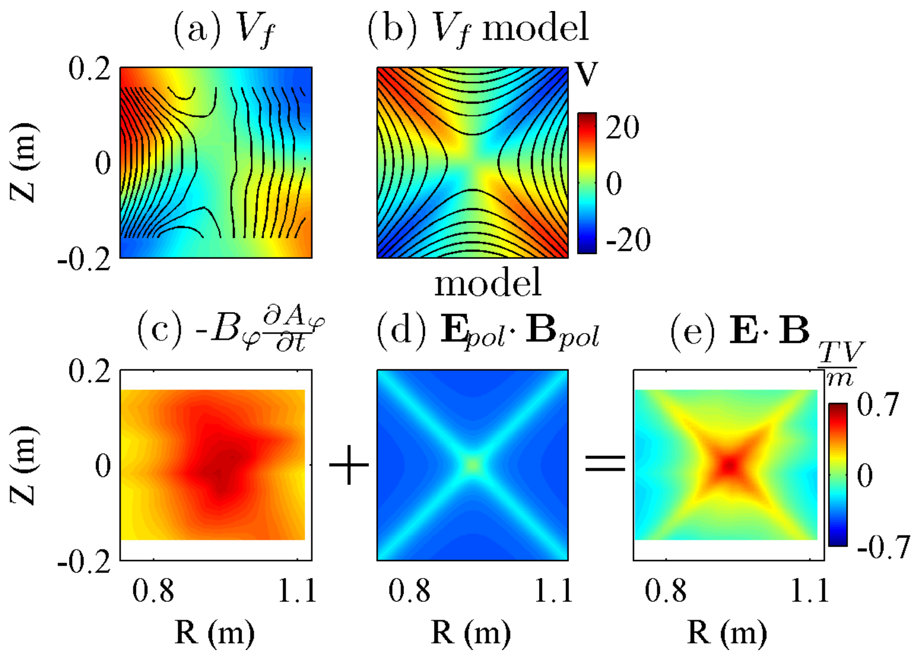

Figure 5-9: (a) Electrostatic potential at onset location, with in-plane magnetic field lines; (b) model potential and magnetic field; (c) measured -$B_\varphi \partial A_\varphi / \partial t$; (d) model $\mathbf{E}_{\text{poloidal}} \cdot \mathbf{B}_{\text{poloidal}}$; (e) sum of (c) and (d) showing total $\mathbf{E} \cdot \mathbf{B}$ is close to 0 away from the x-line. The Data is recorded 8 μs before the time of fastest reconnection.

configuration. In addition, the inductive electric field is largest at the onset angle (at the time of onset). Therefore, at the onset angle, $\mathbf{E} \cdot \mathbf{B} \simeq 0$ is maintained away from the x-line as described in Fig. 5-9c-e. At toroidal angles away from the onset location, we still expect that $\mathbf{E} \cdot \mathbf{B} \simeq 0$ away from the x-line. It is possible that at the moment of onset, both inductive and electrostatic components are small away from the onset angle; however, the detailed balance is not known.

On the opposite side of the torus, where the potential of the mode is reversed, and $\mathbf{E}_{\text{pol}} \cdot \mathbf{B}_{\text{pol}}$ has the opposite sign, we expect the toroidal $E_\varphi B_\varphi$ to have the opposite sign as well. When the electrostatic part of E_φ is taken into account (see Fig. 5-2b), it opposes the inductive electric field on the opposite side of the torus, and may be large enough to make $E_{\varphi,\text{total}}$ negative there. However, more experimental data is still required to determine the detailed structure of the electric fields at this location.

If rational q is required for spontaneous reconnection, we may expect to observe reconnection for $q = 5/2$ for example, or even $q = 20/7$ for that matter. Both values are attainable in the experiment. The in-plane potential of these modes would be highly structured and may not couple strongly to the x-line current channel. This may be the reason that reconnection at these values of q is not observed.

5.3 Plasma and Current Densities

Figure 5-10 shows a 3D dataset of the toroidal current density, constructed similarly to the data in Fig. 5-5 using multiple discharges with different onset locations. At each time and toroidal angle, however, only a single discharge is used for the poloidal cross-section. The onset angle in the figure is set to $\varphi = 0°$, and the current density is clearly not toroidally symmetric. The asymmetry becomes more pronounced between $t = 170$ μs and $t = 202$ μs, 8 μs before the reconnection onset. The current channel at the x-line, which is most prominent at $\varphi = 340°$, peaks and thins just before the onset (by Lenz's law). The thickness of the thin current channel is on the order of the ion sound gyro-radius ρ_s, and after the onset, the current density falls to about half its previous value, or 20 kA/m^2. After the onset, a plasma filament is emitted, as can be seen at $\varphi = 220°$ and $\varphi = 160°$ for $t = 210$-226 μs. This filament appears to be emitted backwards into the inflow region. This observation does not contradict the observation of plasma flows in the outflow region (Fig. 4-5), because the E×B velocity is opposite at the onset location ($\varphi = 0°$) and the far side ($\varphi = 180°$). This is due to the rotating potential (Fig. 5-8), which reverses sign at $\varphi = 180°$. The flow speed can be approximated from the $\varphi = 160°$ data in the figure as $v \sim 0.06$ m/8 μs$\sim$ 8 km/s, similar in magnitude to the ejection speed of the outflow filament of Section 4.2.

It is instructive also to subtract the background current density in order to see the toroidal variation more clearly. The background current is computed as the spatially-smoothed average current at $t = 202$ μs, and it is shown in Fig. 5-11. Note that the current density presented in Figs. 5-10 and 5-11 includes only the plasma current, not the current in the in-vessel conductors.

When this background current is subtracted from the current density in Fig. 5-10,

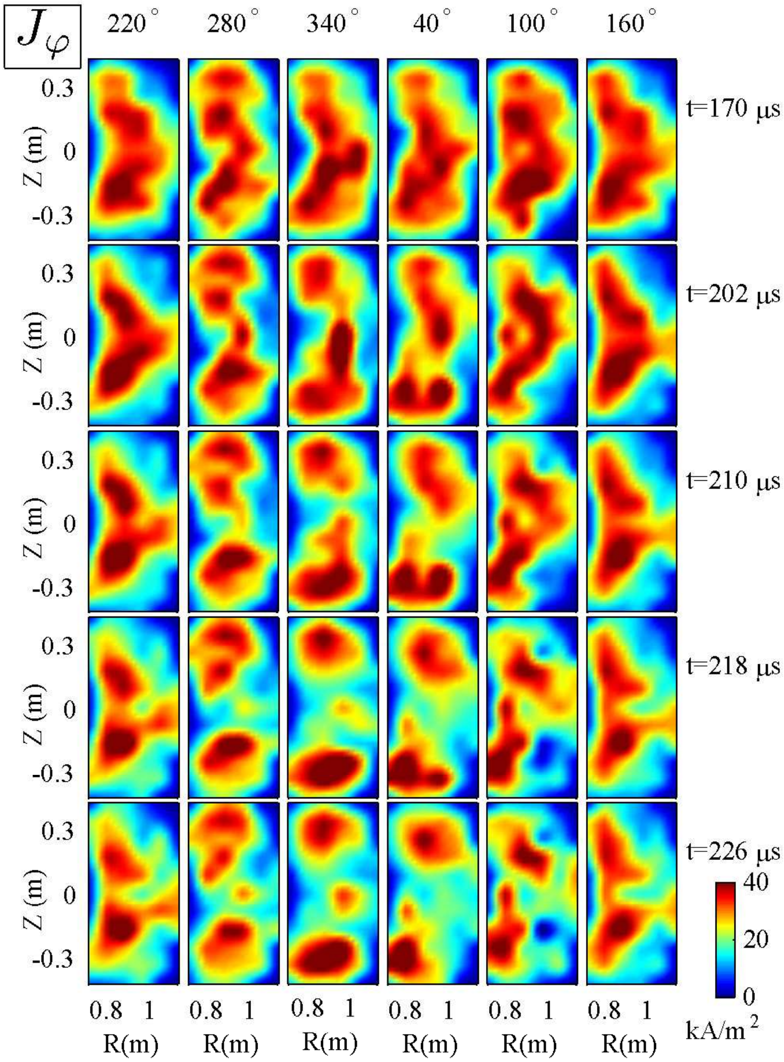

Figure 5-10: Poloidal cross-sections of current density for different toroidal angles and times. Near the onset angle, $\varphi = 0°$, the x-line current is seen to decrease sharply.

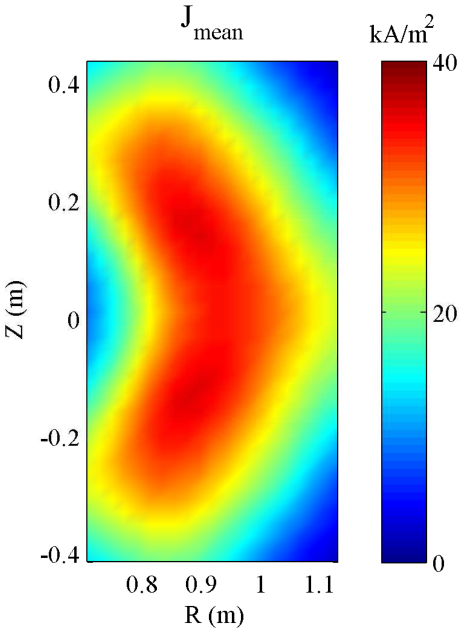

Figure 5-11: Background, toroidally symmetric current density, computed as the spatially smoothed average current at $t = 202\ \mu$s in Fig. 5-10.

we obtain the current density deviation in Fig. 5-12. A similar $q = 2$ mode structure to that in the potential is observed, for example, at $t = 202\ \mu$s. The mode also rotates clockwise for increasing φ, following the magnetic field lines. The mode appears to converge onto the x-line ($\varphi = 340°$ at $t =$ 210-218 μs), and the current at the x-line decreases suddenly.

The plasma density response is qualitatively consistent with the E×B flow imposed by the potential of Fig. 5-8. Figure 5-13 shows the density at three toroidal locations, at multiple times. The density is measured by the high-resolution Langmuir probe array biased to collect ion saturation current. At each time and toroidal angle, we combine several discharges recorded as the array was scanned in major radius. Following the peak reconnection at $t = 210\ \mu$s, the density lines up in oppositely oriented diagonals at $\varphi = 280°$ and $\varphi = 100°$. This can be understood by considering the potential of Fig. 5-8 at $\varphi = 260°$ and $\varphi = 80°$, respectively. The E×B streamlines correspond to contours of constant potential. Since the toroidal magnetic field points into the page, the plasma flows from the lower-right and upper-left quadrants into the lower-left and upper-right quadrants at $\varphi = 80°$ and vice versa at $\varphi = 260°$. This

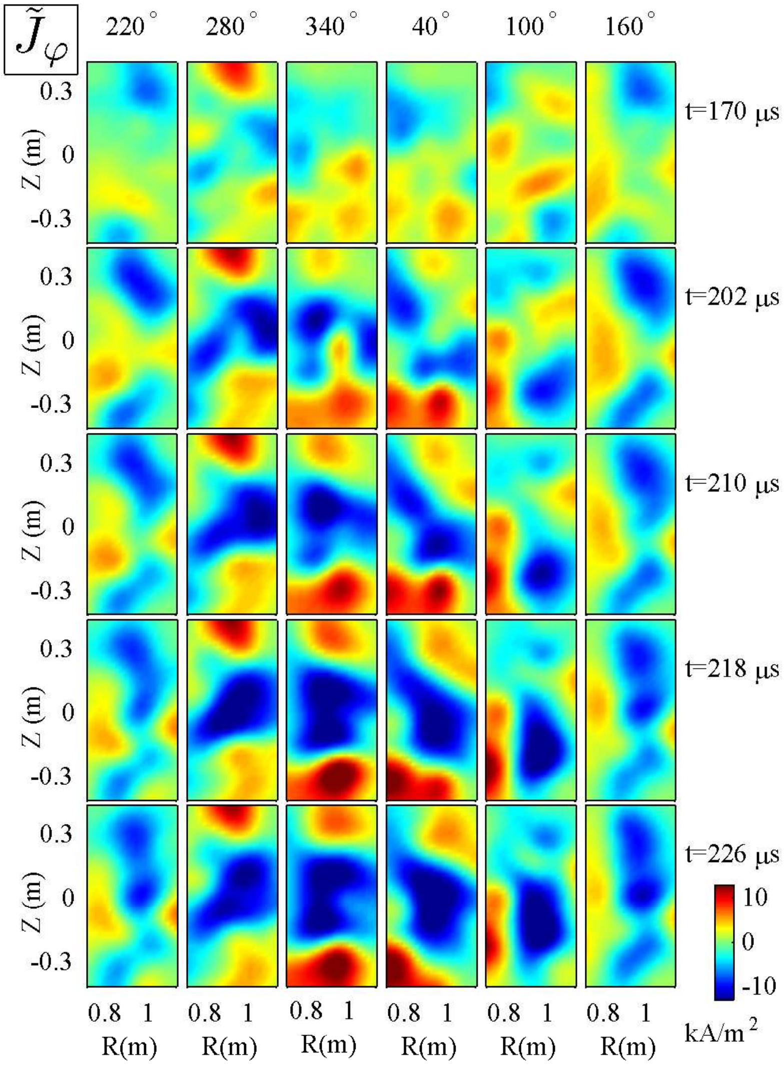

Figure 5-12: Poloidal cross-sections of $J_\varphi - J_{\text{background}}$ for different toroidal angles and times. A field-aligned $q = 2$ mode structure emerges.

flow pattern can account for the diagonal density perturbation.

At the onset angle ($\varphi = 0°$), the x-line density decreases approximately by half during the reconnection, just as the current density does. In addition, at $\varphi = 100°$, a filament of plasma is ejected into the inflow, as discussed above regarding Fig. 5-10.

5.4 Ohm's Law at the X-Line

A central question regarding magnetic reconnection is what the important terms are in Ohm's law at the x-line. We have shown in Section 4.1 that electron collisions with ions and neutrals are important in balancing the toroidal electric field. This is the case at early times as the density is building up and at most other times when the ratio of E/J at the x-line is at its baseline level. However, during the spontaneous reconnection event, the collisional resistivity is insufficient to balance the electric field at the x-line. As discussed in Sections 1.2.2-1.2.3, there are other terms besides collisional resistivity which may be important in Ohm's law. Neglecting electron inertia, we may write one version of Ohm's law as

$$-\frac{\partial A_\varphi}{\partial t} - \nabla_\parallel \phi = -\frac{(\nabla \cdot \overleftrightarrow{p})_\parallel}{ne} + (\eta + \eta_{\text{anomalous}})J_\parallel \tag{5.4}$$

where $\eta_{\text{anomalous}}$ is the effective resistivity felt by current-carrying electrons due to waves or plasma turbulence.

The exact balance of this equation in VTF and whether other terms are important is not yet known. In Ref. [112], Fox suggests that anomalous resistivity due to lower-hybrid turbulence is too small to balance the reconnection electric field at the x-line. We may estimate the magnitude of some of the other terms in Eq. 5.4. If we assume a uniform field-aligned electron temperature of 15 eV, and a scalar pressure, then the pressure term is $(\nabla_\parallel p)/ne \sim (T_e/e)\nabla_\parallel \log n \sim 15\ V \times 1/1\ m \sim 15$ V/m, where $\nabla_\parallel \log n$ at the x-line was estimated from Fig. 5-13. Similarly, the electrostatic component can be estimated from Fig. 5-3 as -10-10 V/m. It appears then that both the pressure term and the electrostatic electric field are important in Ohm's law,

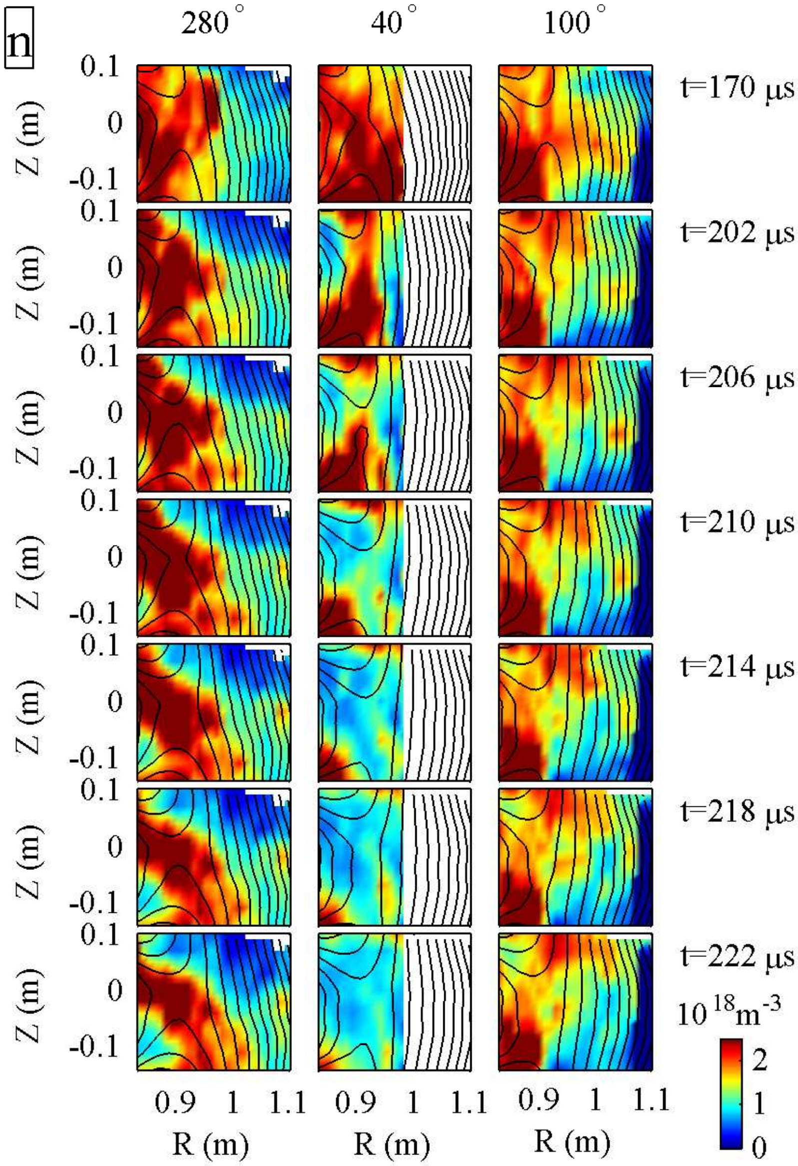

Figure 5-13: Poloidal cross-sections of plasma density (m^{-3}) for different toroidal angles and times, with superimposed poloidal projection of magnetic field lines.

since the toroidal inductive electric field is $\partial A_\varphi/\partial t \sim 15-25$ V/m. Furthermore, recall that the inclusion of the pressure term introduces the ion sound Larmor radius $\rho_s = \sqrt{m_i T_e}/(qB) \sim 4$ cm, and the spontaneous reconnection occurs just as the current channel width (see Fig. 5-10) approaches ρ_s [101]. Because of the 3D nature of the reconnection, the pressure term and the electrostatic field do not vanish at the x-line. However, in the toroidally integrated version of Eq. 5.4 these terms do vanish. Therefore, some other effect, such as field line stochasticity or off-diagonal terms in $\nabla \cdot \overleftrightarrow{p}$, must play a role in Ohm's law.

5.5 Observation of $q = 3$ Reconnection

When the toroidal magnetic field is increased, the spontaneous reconnection event disappears at first, but then reappears at $B = 72$ mT. We show that this new event is associated with a $q = 3$ plasma mode similar to the $q = 2$ reconnection mode.

As in the $q = 2$ case, toroidal asymmetry is observed in the reconnection rate. This is shown in Fig. 5-14, where the reconnection rate at $Z = 0$ is shown for multiple times. (a) and (b) show two separate discharges. Although the asymmetry is clear, Fig. 5-14 suggests that the onset angle in $q = 3$ discharges is more uncertain than that in the $q = 2$ case of Fig. 5-2. For example, in Fig. 5-14a, the onset angle appears to be $\varphi \sim 145^\circ$. However, the subsequent time series does not show clear evidence of bi-directional toroidal propagation and peaking on the opposite side of the torus (as in Fig. 5-2). Hence, the fitting routine of Fig. 5-4, which relies on propagation to find the onset angle, fails for $q = 3$.

The poloidal cross-sections of reconnection rate $\partial A_\varphi/\partial t$ are shown in Fig. 5-15. The time of the spontaneous reconnection event is later than the event time in Fig. 5-14. Superimposed on $\partial A_\varphi/\partial t$ are poloidal projections of the magnetic field lines. The reconnection occurs at $\varphi = 90^\circ$ (b) before it reaches $\varphi = 260^\circ$, shown in (a). The x-line at $\varphi = 90^\circ$ moves downward by several cm during the reconnection event and then returns to its starting height. This x-line displacement is not as pronounced in the $q = 2$ case.

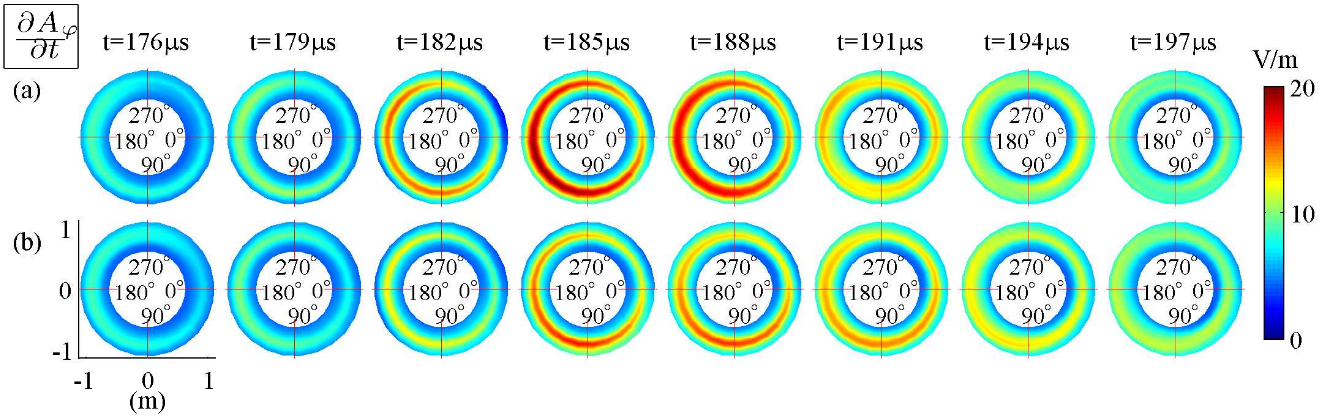

Figure 5-14: $\partial A_\varphi/\partial t$ at $Z = 0$ for two discharges at multiple times.

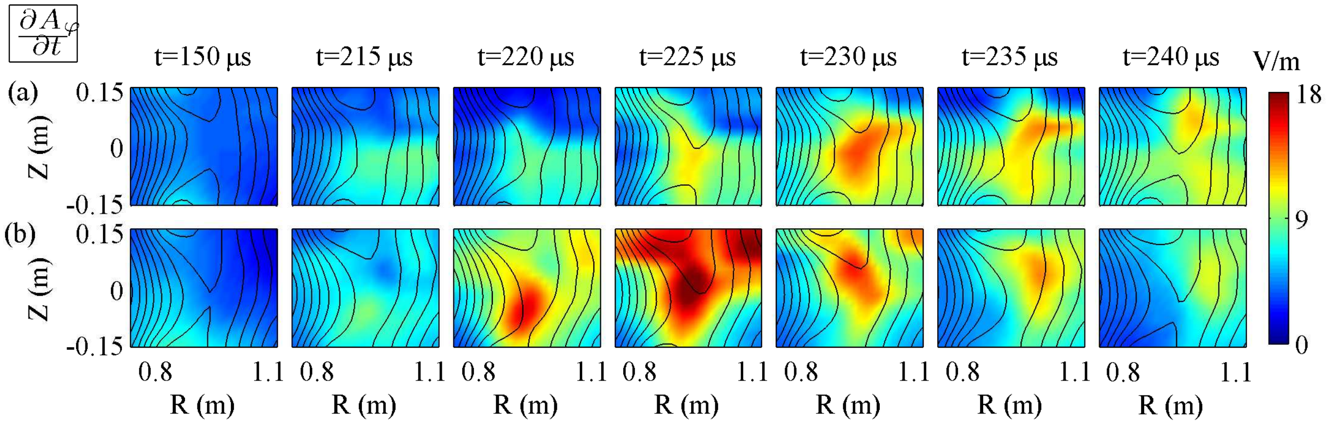

Figure 5-15: Poloidal cross-sections of reconnection rate $\partial A_\varphi/\partial t$ at different times. (a) $\varphi = 260°$; (b) $\varphi = 90°$.

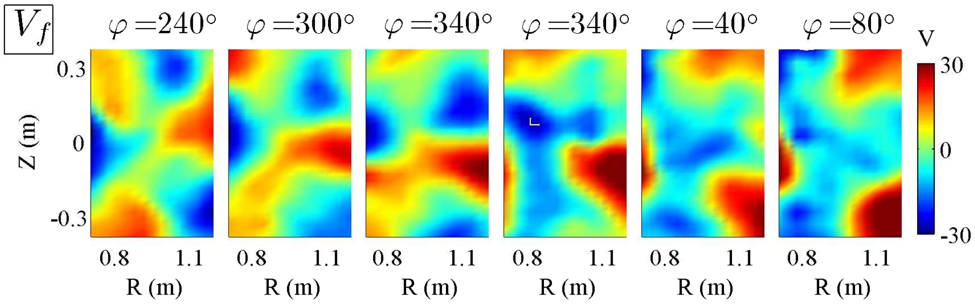

Figure 5-16: Floating potential at different toroidal cross-sections. The first three cross-sections are from a different discharge than the last three. A $q = 3$ mode is evident in the potential.

The $q = 3$ structure of the mode is most clearly seen in the floating potential, shown in Fig. 5-16. The potential is recorded at the time of fastest reconnection, and combined from two discharges. The three poloidal cross-sections at left are from one discharge, while the three at right are from another. The relative toroidal angles in the two discharges are lined up by matching the potential structure. The potential is seen to rotate with magnetic field lines and the fact that $q = 3$ allows the potential to map onto itself self-consistently in one toroidal circuit.

Figure 5-17 shows the current density at two different toroidal angles at multiple times. The toroidal current averaged over 10 discharges with similar current. The current at the x-line is seen to decrease suddenly, as a plasma filament is ejected radially outward ($t = 176 - 196$ μs). The $q = 3$ mode structure is also evident in the toroidal current density, when the background current is subtracted. This toroidally symmetric background current is calculated similarly to that in Fig. 5-11. The toroidally asymmetric component of the current density is shown in Fig. 5-18 for the same toroidal angles and times as J in Fig. 5-17.

The plasma density is shown in Fig. 5-19 for two toroidal angles at multiple times with superimposed poloidal magnetic field lines. The data is combined from several discharges using the high-resolution Langmuir array. During the reconnection, which peaks at $t = 210$ μs, strong flows are observed to reorganize the plasma. These flows are likely related to the large poloidal electric fields associated with the spontaneous reconnection.

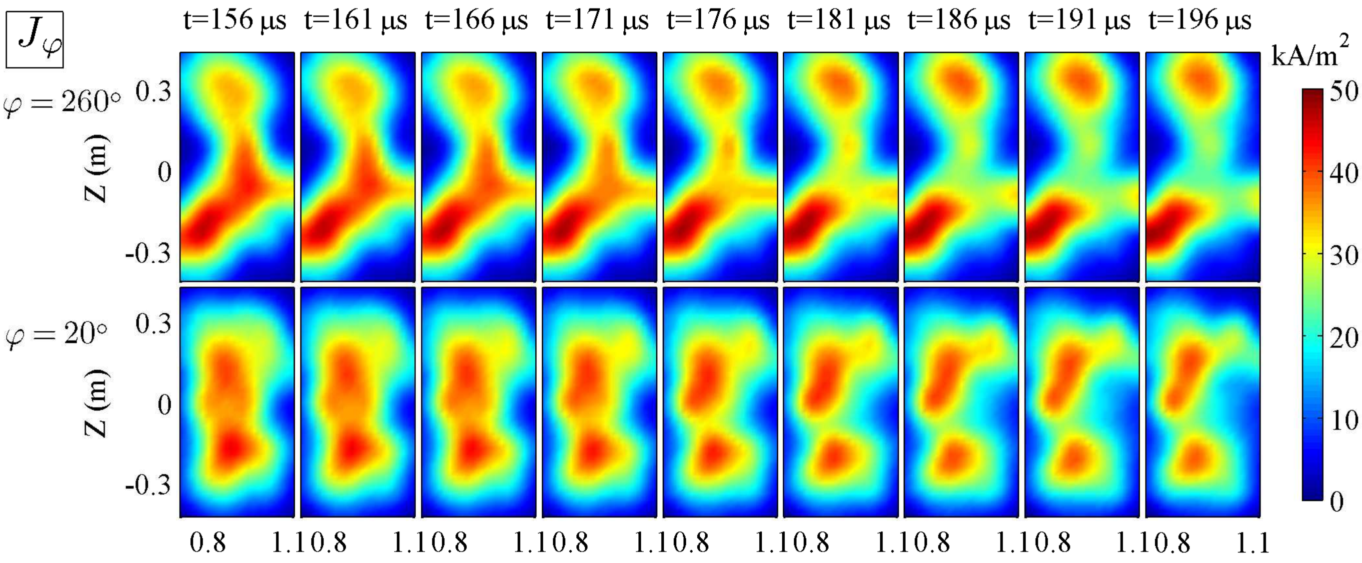

Figure 5-17: Current density for $q = 3$ at two cross-sections at various times. Spontaneous reconnection occurs at $t = 176$ μs.

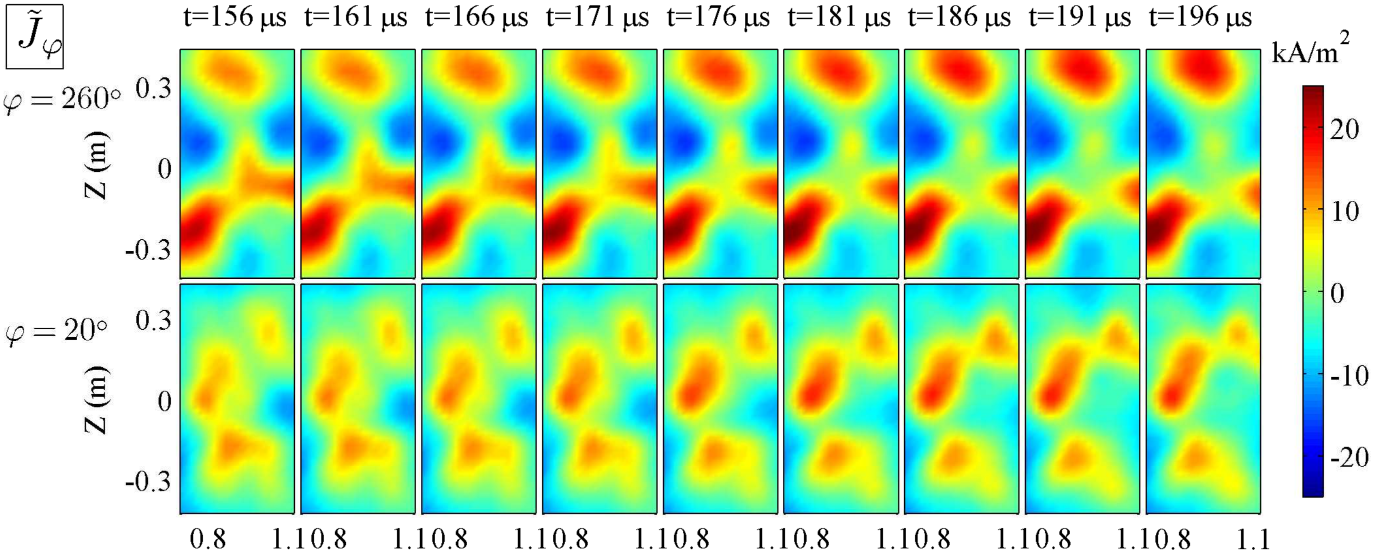

Figure 5-18: Mode structure in current density for $q = 3$, computed by subtracting average background current from Fig. 5-17. Spontaneous reconnection occurs at $t =$ 176 μs.

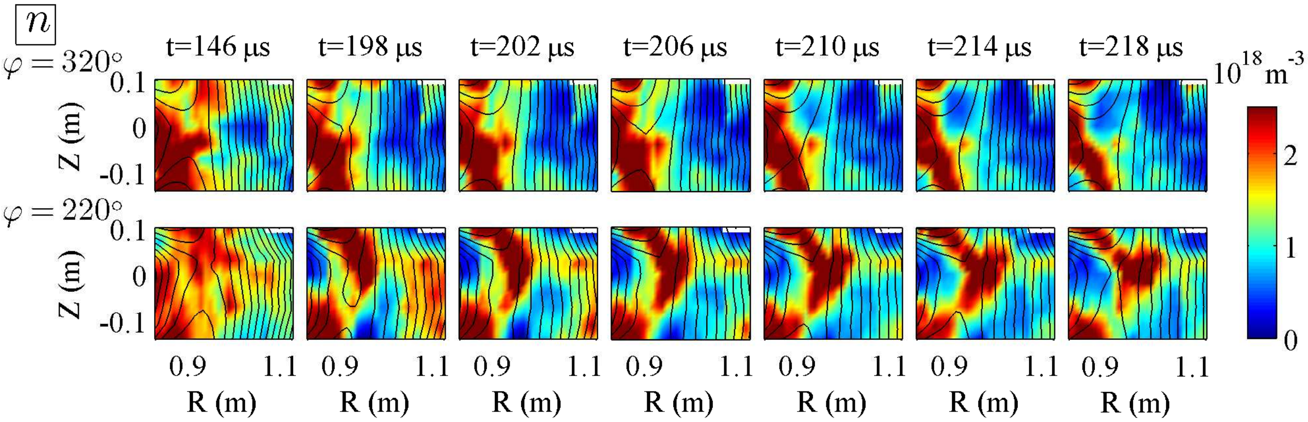

Figure 5-19: Plasma density at two toroidal angles for multiple times for a $q = 3$ discharge. Spontaneous reconnection occurs at $t = 210$ μs.

Chapter 6

Model for Spontaneous Reconnection Onset

We find that the global plasma mode plays a key role in breaking axisymmetry and enabling the spontaneous reconnection event to occur. In this chapter, we will show that the time-dependent structure of the measured floating potential results in ion polarization currents which divert parallel current from the x-line, thus providing current continuity. We focus throughout on the $q = 2$ case, and show that the current diversion is not axisymmetric. We then introduce a model for the onset and the growth rate. The model relates the parallel current density, reconnection rate, and electrostatic potential. We find good agreement with the experimentally measured growth rate of $\partial A_\varphi/\partial t$ during the onset of reconnection.

6.1 Toroidal Asymmetry in Current Density at the X-Line

We have shown in Section 5.1 that the onset of fast reconnection is toroidally localized, and that the onset is followed by a propagation of the reconnection around the torus. The localized onset of reconnection is linked to the behavior of the parallel current at the x-line, since the magnetic vector potential A_φ is related to the toroidal current density by

$$A_\varphi(\mathbf{r}) \simeq \frac{\mu_0}{4\pi} \int \frac{J_\parallel}{|\mathbf{r}' - \mathbf{r}|} d^3\mathbf{r}'. \tag{6.1}$$

At the x-line, the toroidal current density is identical to the parallel current density. Although the local value of the reconnection rate $-\partial A_\varphi/\partial t$ is affected by current dynamics everywhere around the torus, the strongest influence of $\dot{J}_\parallel$ on the reconnection rate is local, because of the $1/r$ weighting in the integral. Therefore, a local reconnection onset corresponds to a localized decrease in parallel current at the x-line.

Before the reconnection event, the parallel current density at the x-line flows in toroidal loops. Immediately after the onset, the toroidal current decreases sharply at one toroidal angle and $\nabla \cdot (J_\parallel \mathbf{B}/B) \neq 0$. However, in a quasineutral plasma, there cannot be charge accumulation, and other currents must be present to close the current loops and maintain current continuity. These cross-field currents turn out to be ion polarization currents due to the time-dependence of the potential. The equation for current continuity is given by

$$\nabla_\parallel J_\parallel + \nabla_\perp \cdot \mathbf{J}_\perp = 0, \tag{6.2}$$

while the ion polarization current is given by[1]

$$\mathbf{J}_\perp = \frac{m_i n}{B^2} \frac{d\nabla_\perp \phi}{dt}. \tag{6.3}$$

To find the relationship between parallel currents and ion polarization currents, we integrate up $\nabla_\perp \cdot \mathbf{J}_\perp$ along field lines from some reference point—the 'edge'—which the field lines cross

$$J_\parallel(\mathbf{r}) = J_{\text{edge}} + \int_{\text{edge}}^{\mathbf{r}} \frac{mn}{B^2} \nabla_\perp^2 \frac{\partial \phi}{\partial t} dl \tag{6.4}$$

---

[1] We assume that the poloidal electric field $\mathbf{E}_{\text{pol}} \simeq \mathbf{E}_\perp$ is electrostatic. This assumption can be motivated as follows. We write $\mathbf{E}_{\text{pol}} = -\nabla_{\text{pol}}\phi - \partial A_{\text{pol}}/\partial t$ and we wish to show that the ratio $\mathcal{R} = |\nabla \times \mathbf{E}_{\text{pol}}|/|\nabla_{\text{pol}} E_{\text{pol}}| \ll 1$. We neglect $\nabla_\varphi \times \mathbf{E}_{\text{pol}}$ relative to $\nabla_{\text{pol}} \times \mathbf{E}_{\text{pol}}$ because of the large toroidal aspect ratio $R/a \sim 10$ (where a is the poloidal scale length), and write: $\mathcal{R} = |\nabla_{\text{pol}} \times \mathbf{E}_{\text{pol}}|/(E_{\text{pol}}/a) \sim (\Delta B_\varphi/\tau)/(E_{\text{pol}}/a)$ where τ is the characteristic time scale. In Appendix A, we note that $\Delta B_\varphi < 0.1|\mathbf{B}_{\text{pol}}|$. Therefore, the ratio becomes $\mathcal{R} < (0.1 B_{\text{pol}} a)/(E_{\text{pol}}\tau) \sim (0.1 B_{\text{pol}}/B_\varphi) \times (B_\varphi/E_{\text{pol}})(a/\tau) \sim 0.1 B_{\text{pol}}/B_\varphi \sim 0.01$. Hence $\mathcal{R} \ll 1$ and $\mathbf{E}_{\text{pol}} \simeq -\nabla_{\text{pol}}\phi$ and $\mathbf{E}_\perp \simeq -\nabla_\perp \phi$.

where we have assumed uniform density, and the nonlinear part of the time derivative was dropped in order to focus on the initial linear potential perturbation ($d/dt \equiv \partial/\partial t - \nabla\phi \times (\mathbf{B}/B^2) \cdot \nabla \rightarrow \partial/\partial t$).

To proceed quantitatively, we model the magnetic field near the x-line by a linear cusp, with finite current:

$$\mathbf{B} = b_0(z\hat{r}/\alpha + \alpha r\hat{z} + l_0\hat{\varphi}). \tag{6.5}$$

The parameters $b_0 = 0.035$ T/m and $l_0 = 1.7$ m are found from matching this model to the experimentally measured magnetic field. The parameter α controls the current density $J_\varphi = b_0(\alpha - 1/\alpha)$, and hence the angle of the cusp. An angle of 90° where $\alpha = 1$ gives $J_\varphi = 0$. To match the experimentally measured current density, we choose $\alpha = 1.7$.

We model the potential of the mode using a log form similar to that in Fig. 5-9, but with a few modifications:

$$\begin{aligned} \phi &= \phi_0 \log\left[\frac{z'^2 + \delta^2}{r'^2 + \delta^2}\right] \qquad (6.6) \\ r' &= \cos(\Delta\varphi/2)r\sqrt{\alpha} + \sin(\Delta\varphi/2)z/\sqrt{\alpha} \\ z' &= -\sin(\Delta\varphi/2)r\sqrt{\alpha} + \cos(\Delta\varphi/2)z/\sqrt{\alpha}. \end{aligned}$$

The field line coordinates have a period of 4π, appropriate for $q = 2$, while the resulting potential maps onto itself in just 2π, as it must. The parameter α is used to make the mode line up with the angle of the magnetic separatrix. In addition, $\Delta\varphi \equiv \phi - \phi_{\text{onset}}$, and $\phi_0 = 6$ V is chosen to match the experiment. The parameter δ is the poloidal distance of the mode from x-line, and we take it to depend on φ: $\delta = \delta_0(1 - \frac{2}{3}\cos(2\Delta\varphi))$, where $\delta_0 = 0.12$ m. This form for δ is consistent with the measured potential (see Fig. 5-8). The model potential is plotted at different toroidal angles in Fig. 6-1a.

In Section 5.2, we discussed how the log form of the potential arises to maintain $\mathbf{E} \cdot \mathbf{B} \simeq 0$ away from the x-line, where $q \simeq 2$. For the potential in Eq. 6.6, with

$\Delta\varphi = \pi/2$ and $r, z \gg \delta$, the quantity $\nabla\phi \cdot \mathbf{B}$—with $\mathbf{B}$ given by Eq. 6.5—is spatially uniform and is balanced by $E_\varphi = 4\phi_0/l_0$. This observation justifies the use of the $\sqrt{\alpha}$ factors in Eq. 6.6. At other toroidal angles, the condition that $\mathbf{E} \cdot \mathbf{B} = 0$ is relaxed in order to have a relatively simple analytic expression for ϕ. Nevertheless, Eq. 6.6 matches the experimentally measured potential, and is qualitatively consistent with the ideal Ohm's law away from the x-line.

Next [113], we evaluate the integral along field lines in Eq. 6.4 using the modeled ϕ and $\mathbf{B}$. We focus on a box of dimensions 0.5 m × 0.5 m surrounding the x-line, and compute $\nabla_\perp^2 \dot{\phi}$, where the time derivative is replaced by the growth rate of the mode, which is evaluated in Section 6.2 below. Figure 6-1b shows this term at different toroidal angles, and (d) shows the result of the integral in Eq. 6.4 for $J_\parallel$. The current density at the boundary is assumed to be evenly distributed at the two edges of each field line. The calculated $J_\parallel$ represents the change in magnetic field-aligned current due to perpendicular ion polarization currents associated with the growing mode in the electrostatic potential. The toroidal asymmetry in $\Delta J_\parallel$ is related to the asymmetry in the potential.

The current density in Fig. 6-1d is assumed to be unchanged on the opposite side of the torus, since the reconnection at onset is localized to one toroidal region. A toroidally symmetric background current is added in (d) to make the current density 0 on the far side where $\Delta\varphi = 180°$. The experimentally measured change in $J_\parallel$ over the 8 μs leading up to peak reconnection is shown in (c) of the figure. The model and experiment agree at the x-line in magnitude, sign and toroidal dependence, if not in the details of the poloidal cross-sectional profile. The disagreement along the separatrix may be due to the assumptions of uniform density, linear geometry, or the simplified potential model. Alternatively, it is possible that slight magnetic stochasticity affects the separatrix specifically because of its long integration paths in Eq. 6.4.

The reason for the asymmetry in parallel current has to do with the different signs of the potential sampled by the field lines along which Eq. 6.4 is integrated. Consider the two field lines in Fig. 6-1a-b. The gray field line passes near the x-line

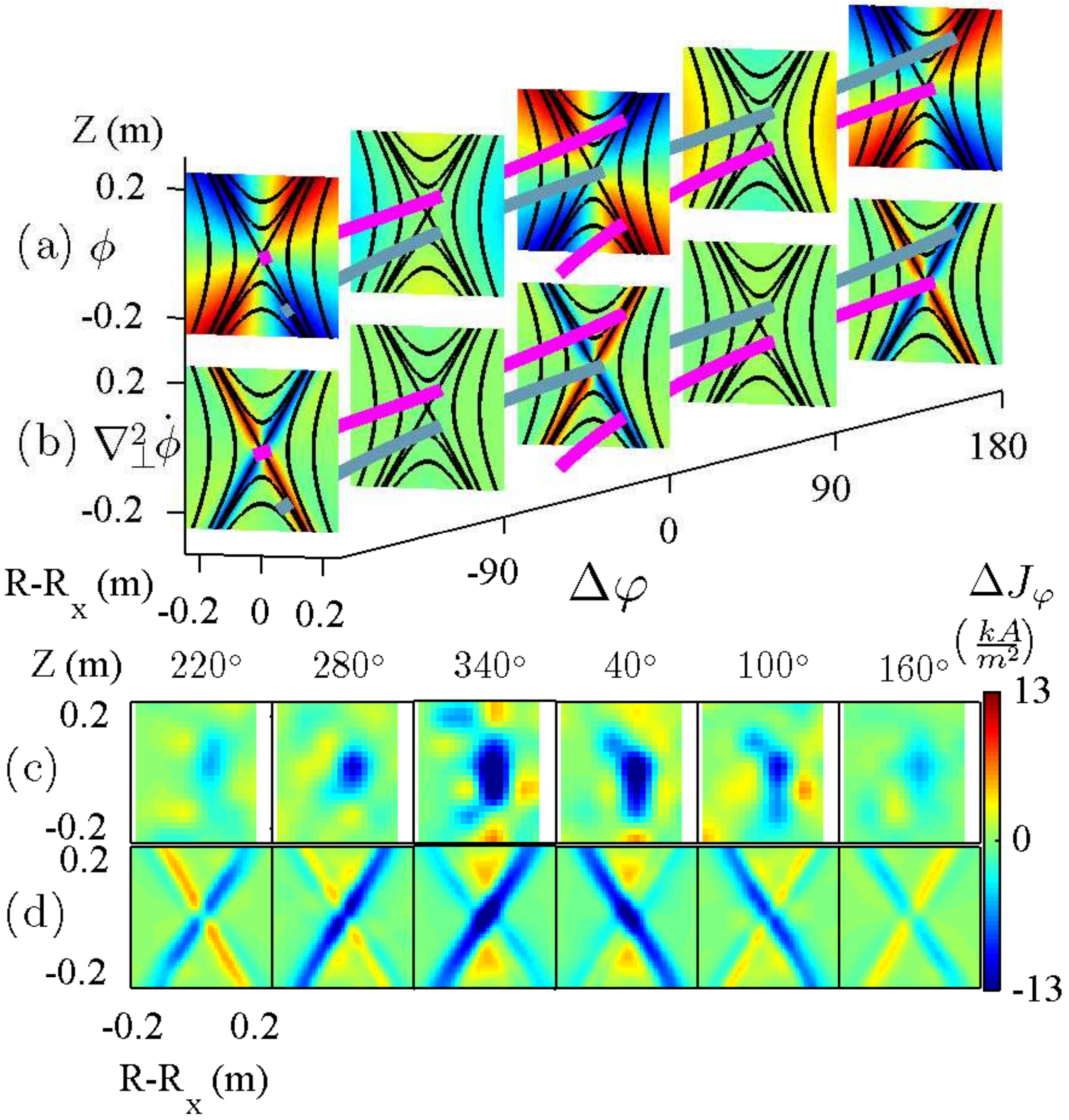

Figure 6-1: (a) 3D potential of Eq. 6.6; the magenta field line passes by the x-line on the opposite side of the torus from the reconnection onset; the gray field line passes by x-line at the onset angle; (b) divergence of ion polarization currents $\propto \nabla_\perp^2\dot{\phi}$; (c) experimentally measured change in J_φ during the 8 μs leading up to peak reconnection; (d) integrating (b) along field lines (Eq. 6.4) gives asymmetric parallel current.

at the onset location ($\Delta\varphi = 0$), while the magenta field line passes near the x-line at $\Delta\varphi = 180°$. The quantity $\nabla_\perp^2 \dot{\phi}$ in Fig. 6-1b represents the amount of charge due to perpendicular ion polarization currents which must be drained by parallel currents. As φ increases from $-180°$ to $180°$, the gray field line sees first a buildup of charge (red) and then an outflow of charge (blue), and hence there must be parallel current in the $\hat{\varphi}$ direction, which prevents charge build-up and maintains current continuity. This parallel current turns out to be opposite the background current. The reverse is true for the magenta field line. This field line first samples an outflow of perpendicular current (blue) and then an accumulation (red) as φ is increases. Therefore, the parallel current along this field line is in the $-\hat{\varphi}$ direction and enhances the background current. We are free, however, to add a toroidally symmetric current which maintains the parallel current at $\Delta\varphi = 180°$ at 0.

The importance of the $q = 2$ mode is revealed by comparison with previous reconnection experiments on VTF by Egedal *et al.* [116, 114], with open magnetic field boundary conditions. These experiments found a toroidally symmetric potential structure, similar to the one observed at the onset angle here. The similarity is due to the $\mathbf{E} \cdot \mathbf{B} = 0$ condition in a magnetic cusp geometry (see Section 5.2), but there is a crucial difference between the symmetric-potential experiments and the present experiments. To show this difference, we apply current continuity to the symmetric case. As before, the time dependence of the potential gives ion polarization currents, and these perpendicular currents are balanced by parallel currents, whose change is related to the magnetic reconnection. The results for the symmetric case are shown in Fig. 6-2. (a) shows the symmetric potential, in which the magenta and gray field lines now sample the same values of ϕ. (b) shows the quantity $\nabla_\perp^2 \dot{\phi}$, which is proportional to the divergence of the ion polarization currents associated with the potential in (a). The integral along field lines is computed (Eq. 6.4), and the result is shown in (c) of the figure. The major difference in the toroidally symmetric case is that the x-line current is enhanced, as opposed to being reduced in the asymmetric case. As the potential oscillates in time (Ref. [114]), so does the resulting toroidal current. Meanwhile, the $q = 2$ potential, which rotates with the field lines, is necessary not

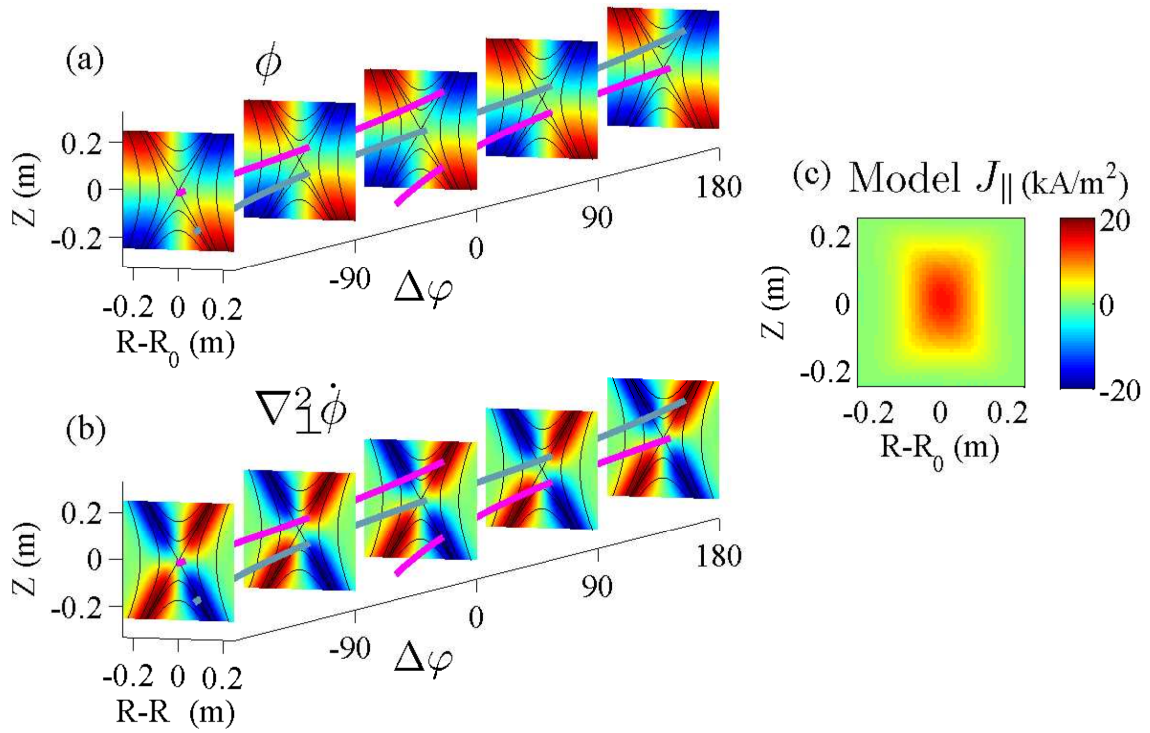

Figure 6-2: (a) axisymmetric potential with similar form to Eq. 6.6; (b) $\nabla_\perp^2\dot{\phi}$; (c) $\Delta J_\parallel$ that results from integrating the symmetric potential in Eq. 6.4; note that $\Delta J_\parallel$ at the x-line has the opposite sign from the case of rotating potential (Fig. 6-1)c.

only for the toroidal localization of reconnection, but also for the spontaneous onset.

From the current density computed and displayed in Fig. 6-1, we may calculate the reconnection rate for the non-axisymmetric case. We use the relation $\nabla^2\mathbf{A} = -\mu_0\mathbf{J}$ and apply the time-scale computed in the next section to find $\partial A_\varphi/\partial t$. The results are shown in Fig. 6-3, where the resulting reconnection rate is compared against the experimental measurement. At the x-line, the reconnection rate is largest at the onset location and the magnitude agrees as well.

6.2 Model of the Spontaneous Reconnection

We have argued that the potential structure of the mode at the onset angle arises to maintain $\mathbf{E}\cdot\mathbf{B} \simeq 0$ away from the x-line. This condition links the potential with

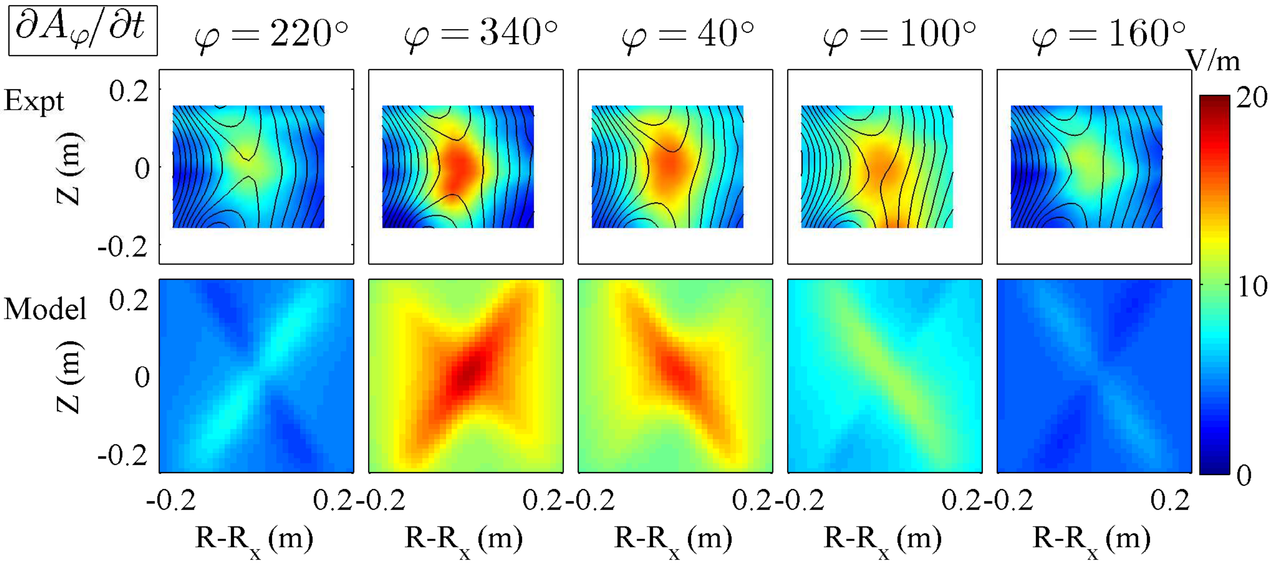

Figure 6-3: (Non-axisymmetric results) Top row: experimental $\partial A_\varphi/\partial t$ reproduced from Fig. 5-5 at t=210 μs. Bottom row: model $\partial A_\varphi/\partial t$ computed from the current density in Fig. 6-1. Although the detailed cross-sections are not identical, the toroidal dependence at the x-line agrees well.

the reconnection rate. We show this quantitatively in Fig. 6-4, where the correlation between mode amplitude and reconnection rate is shown for many discharges, including both shots with and without a spontaneous reconnection event. The amplitude of the potential is computed as the root mean square of deviations from the mean of the floating potential. These deviations are evaluated in a box around the x-line (20 cm × 30 cm) at the time of fastest reconnection. The values of $\partial A_\varphi/\partial t$ are computed as the average reconnection rate in that same box, at the toroidal angle of fastest reconnection. A best-fit line, which is constrained to pass through the origin, is shown in the figure as well. The two quantities are well-correlated ($r = 0.76$), and this correlation can be thought of as an empirical Ohm's law which balances the inductive and electrostatic components of the electric field away from the x-line. We use this Ohm's law with the results of Section 6.1 to model the onset.

We wish to calculate the growth rate associated with the spontaneous reconnection event, a process which is shown conceptually in Fig. 6-5a. We relate the current density to the potential by current continuity (Eq. 6.4), the current density to the magnetic vector potential by Ampère's law (Eq. 6.1), and the potential and mag-

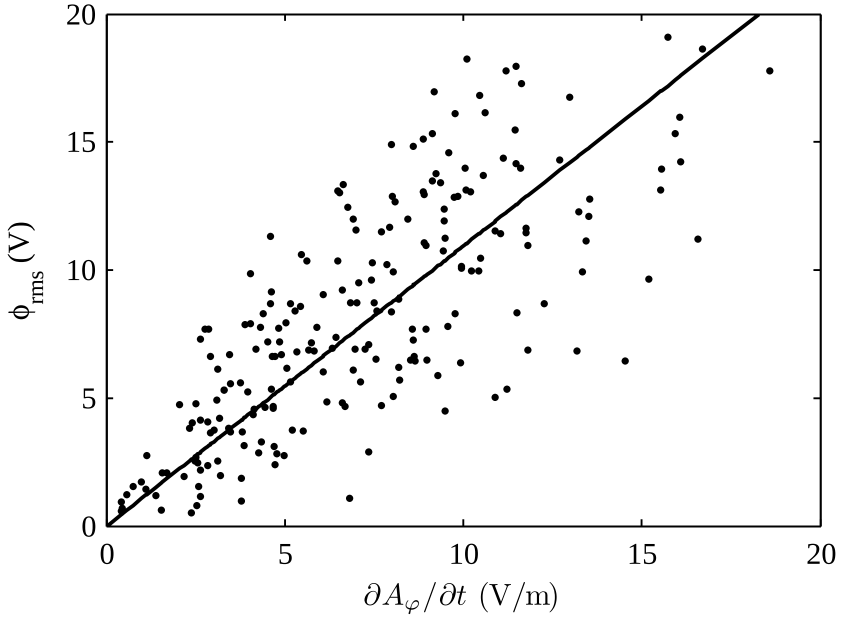

Figure 6-4: Correlation between mode strength and reconnection rate, at the time that this rate is maximized; the fit is constrained to pass through the origin.

netic vector potential by the empirical version of Ohm's law discussed above. These relations give three equations for three unknowns and are combined to give a differential equation for the potential. From this equation, we predict the growth rate. To implement the model of Fig. 6-5a, we combine Eqs. 6.1 and 6.4 to obtain

$$A_\varphi \simeq \frac{\mu_0}{4\pi}\int\left(\int\frac{mn}{B^2}\nabla_\perp^2\dot{\phi}dl\right)\frac{d^3\mathbf{r}'}{|\mathbf{r}-\mathbf{r}'|}, \tag{6.7}$$

where J_{edge} was dropped because we want the magnetic vector potential associated only with the electrostatic potential.

The empirical relation between ϕ and $\dot{A}_\varphi$—which is basically Ohm's law away from the x-line—is shown in Fig. 6-5b. We assume that $\partial A_\varphi(\mathbf{r},t)/\partial t = \tilde{A}(\mathbf{r})\dot{\bar{a}}(t)$ and $\phi(\mathbf{r},t) = \tilde{\Phi}(\mathbf{r})\bar{\phi}(t)$, where $\dot{\bar{a}}$ and $\bar{\phi}$ vary between 0 and 1; the amplitude of the potential is again computed as the root mean square at each time point, while the reconnection rate is averaged over major radius for the toroidal angle of peak reconnection. The

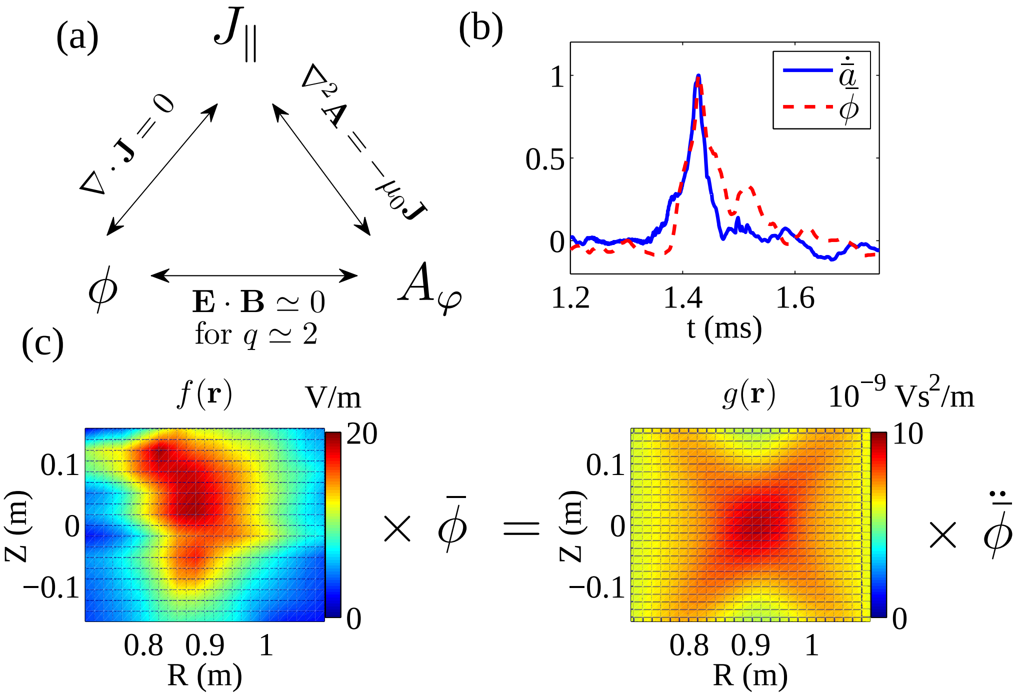

Figure 6-5: (a) Schematic of the model for the exponential growth; $\mathbf{E} \cdot \mathbf{B} \simeq 0$ is an empirical observation which does not apply everywhere, but rather as shown in (b) where the amplitude of the potential and the reconnection rate are plotted. (c) Graphic representation of Eq. 6.8.

empirical observation is then $\dot{\bar{a}} = \bar{\phi}$. We use this observation to rewrite Eq. 6.7 as

$$\tilde{A}\bar{\phi} \simeq \left[\frac{\mu_0}{4\pi}\left(\int^{\mathbf{r}'} \frac{mn}{B^2}\nabla_\perp^2\tilde{\Phi}dl\right)\frac{d^3\mathbf{r}'}{|\mathbf{r}'-\mathbf{r}|}\right]\ddot{\bar{\phi}}. \tag{6.8}$$

This equation has the form $f(\mathbf{r})\bar{\phi}(t) = g(\mathbf{r})\ddot{\bar{\phi}}(t)$, which—if $f(\mathbf{r}) \propto g(\mathbf{r})$ and $f/g > 0$—gives exponential growth for ϕ. For $f(\mathbf{r})$, *i. e.* $\tilde{A}$, we use the experimentally measured profile at its time of maximum, while for $g(\mathbf{r})$ we use the model magnetic field and potential (Eqs. 6.5 and 6.6) to compute the integral along field lines. The result is shown in Fig. 6-5c, where Eq. 6.8 is shown graphically. We see that $f(\mathbf{r})$ and $g(\mathbf{r})$ have similar forms and the same sign. The positive signs—which give an exponentially growing solution—are due to the asymmetry in the potential. Recall that, in contrast, the symmetric potential of Fig. 6-2a changed the sign of $\Delta J_\parallel$ (Fig. 6-2c). Indeed, in Ref. [114], where the potential was toroidally symmetric, oscillatory behavior was observed, as opposed to the exponentially growing spontaneous reconnection seen here.

We substitute $\bar{\phi} \propto \exp(\gamma t)$ into Eq. 6.8 and use the typical peak values in Fig. 6-5c for $f(\mathbf{r})$ and $g(\mathbf{r})$, to find a growth rate of $(22\mu\mathrm{s})^{-1}$. To compare to the experimental value, we use exponential fitting as shown in Fig. 6-6. The average value of $\partial A_\varphi/\partial t$ is computed as it was in Fig. 6-4 for the same box size. The result is a growth rate of $(20 \pm 6\mu\mathrm{s})^{-1}$, where the uncertainty represents the standard deviation of the growth rates in all discharges. The result depends somewhat on the size of the box over which the average of $\partial A_\varphi/\partial t$ is computed, but this variation is within the aforementioned uncertainty.

The growth rate for the $q = 3$ spontaneous reconnection may also be computed using the same method, and we find it to be 22 ±8 μs. This value is the same as the $q = 2$ growth rate within the uncertainty.

In order for ions to respond to a time-varying potential, they must be well-magnetized. In VTF, the ions are magnetized, but only marginally so: $\omega_{ci} = eB/m \sim 1.4 \times 10^5\ \mathrm{s}^{-1}$, or 1 radian per 7 μs, while the mode grows in approximately $\gamma \sim 20\ \mu$s. We compare γ to ω_{ci} instead of f_{ci} because of the way ion polarization current is cal-

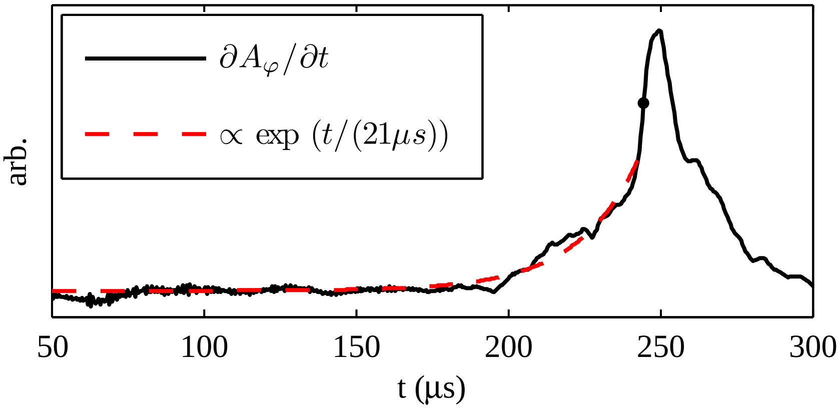

Figure 6-6: Growth rate calculation procedure: an exponential function is fit to the toroidal inductive electric field up to the point indicated, where the derivative of $\partial A_\varphi/\partial t$ begins to decrease.

culated. The ion inertia term in the ion momentum equation, $md\mathbf{v}/dt = e(E+\mathbf{v}\times\mathbf{B})$, must be small compared to the other two terms. Since for well magnetized ions the inertia term scales like $(\gamma/\omega_{ci})eE$, this means that $\gamma/\omega_{ci} \ll 1$ is the relevant condition. Furthermore, in Ref. [114], it is shown that for experiments with similar time-scales the ions are sufficiently magnetized that the use of $J_\perp \sim (mn/B^2)\nabla_\perp\dot{\phi}$ for the ion currents in $\nabla\cdot\mathbf{J} = 0$ gives good agreement with the experimental data.

6.3 Summary

We have shown how a rational q mode appears in the floating potential when the toroidal magnetic field is set to one of two discrete values ($q = 2$ and $q = 3$). This mode is important for maintaining current continuity in non-axisymmetric reconnection. We have modeled the ion polarization currents associated with the $q = 2$ mode and shown that these cross field currents can account for the toroidal dependence of the parallel current density at the x-line.

As shown in Fig. 6-5, we have used current continuity and Ohm's law in the $q = 2$ regions where $\mathbf{E}\cdot\mathbf{B} \simeq 0$ to derive a differential equation for the spontaneous reconnection. This equation gave exponential growth for the amplitude of the potential and the reconnection rate. The growth rate computed from this equation agreed well with the experimentally measured growth rate. The differential equation applies only to the linear stage of the growth and does not account for the saturation of the reconnection rate or the toroidal propagation observed, for example, in Fig. 5-2. The model accounts instead for the toroidally localized onset.

We emphasize that reconnection is not merely a consequence of the current flow pattern; rather, the magnetic energy released during the reconnection is essential for driving the ion polarization currents associated with the strong in-plane potential that develops. This can be seen from the energy balance in Section 4.2, and the fact that the ions attain their E×B outflow velocity by being accelerated in ion polarization currents. Meanwhile, the ion currents enable the reconnection by diverting field-aligned current away from the x-line. Therefore the external q=2 potential and the reconnection grow in time together, and one does not cause the other.

Chapter 7

Discussion and Conclusions

7.1 Summary

We began in Chapter 2 by discussing the propagation of plasma filaments through neutral gas. The experiments described in that Chapter are relevant to the edge of tokamak devices and other laboratory plasmas, but also to the ionosphere, photosphere, and interstellar medium where neutral density is not negligible. We showed how the blob (filament) propagation speed depends on neutral density and blob size, and fully characterized the internal structure and mushroom shape of the blob. The cooling of the blob was also discussed. We speculated regarding applications to reconnection in the photosphere, suggesting that that interaction with neutrals in the outflow reconnection region could reduce the reconnection rate.

We then turned to collisionless plasmas to describe the experimental observation of 3D effects in the onset of spontaneous reconnection events. Magnetic reconnection was induced in a toroidal plasma with an embedded x-line. The plasma was diagnosed by arrays of Langmuir and magnetic probes among other diagnostics, in order to fully characterize the 3D plasma dynamics during each discharge. After a delay of $\sim$100 μs from the reconnection drive, a burst of fast spontaneous reconnection was observed. The reconnection rate could not be explained by a resistive Ohm's law.

A closer investigation of the plasma at multiple toroidal locations showed that the reconnection onset is not toroidally symmetric. The toroidal inductive electric field propagates around the device in both directions. The onset was observed in conjunction with a global rational q mode, seen in both the floating potential and the current density. Fast reconnection was observed for both $q = 2$ and $q = 3$, and therefore only at discrete values of the toroidal magnetic field. The asymmetry in the reconnection rate was also observed in the current density at the x-line, which decreased first at the onset location. Although the onset location varied from discharge to discharge, these variations were not randomly spread around the torus. Rather, they were likely due to small toroidal asymmetries in the experiment that favor one location over another.

We modeled the potential of the mode as uniformly growing in time, and reproduced the localized decrease in current density at the x-line. The decrease occurs at the toroidal angle corresponding to the 'correct' experimentally observed phase of the mode. The ion polarization currents associated with the mode growing in time balanced the toroidally asymmetric field-aligned currents. We use this current continuity, and a version of Ohm's law that applies away from the x-line to predict the growth rate associated with the spontaneous reconnection onset. This growth rate agreed well with the experimentally measured growth rate. We showed also how the toroidal asymmetry of the mode was necessary for the localized decrease in current density at the x-line, by comparing to a toroidally symmetric potential, which gave an enhancement in current at the x-line.

While we have shown that parallel pressure and potential gradients may be important in Ohm's law, the question of how Ohm's law is satisfied at the x-line has not yet been settled. Nevertheless, we were able to use the ideal Ohm's law, which is satisfied away from the x-line, to complete a model for the onset of localized reconnection in VTF. This model shows the importance of 3D effects (toroidal asymmetry) in the onset of fast reconnection.

7.2 Applications to Tokamak Plasmas

Given the results presented regarding 3D effects in magnetic reconnection, as well as the experiments by Park *et al.* [64, 65, 66], which show that the sawtooth onset is toroidally and poloidally localized, it is clear that 2D theories of the sawtooth are insufficient. Specifically, the theories by Kadomtsev [17] and Wesson [117], which are often used to frame the sawtooth problem, require modification to reflect the new observations of toroidal localization.

Strong potential gradients, which we observe here, are not often discussed in relation to the sawtooth instability. An exception is the observation of Hamada *et al.* [118], who used a high energy ion beam to measure potential spikes near the inversion radius during a sawtooth crash. The observed potential was in partial agreement with single-fluid MHD theory, but further measurements are needed.

In the presence of strong 3D effects, the magnetic field may become stochastic, and this effect is sometimes suggested as a mechanism for fast reconnection in sawteeth. In a stochastic magnetic field, electrons could flow along the field into the core, thus cooling it rapidly. However, Wesson [50] describes experiments in JET, which show that impurity nickel ions are also observed to rapidly move into the core during a sawtooth crash. In contrast to the electrons, the nickel is much too heavy to follow stochastic field lines into the core on the timescale of the sawtooth crash. Hence, the nickel must have a cross-field velocity. Hastie [119] suggests that the electrons do move into the core along stochastic field lines, which then builds up a potential difference between the core and the outer plasma which is of order T_e. Hastie suggests that this potential difference may enable E×B convection of ions, impurities and magnetically trapped electrons into the core, even with $q < 1$ inside the inversion radius. Hastie does not mention ion polarization currents, but it is also possible that these are responsible for the inward transport of ions and impurities during the sawtooth crash. Although the q profile in tokamaks is not as flat as in VTF, our results suggest that future investigations of tokamak sawteeth should more fully investigate the internal potential structure.

7.3 Suggested Future Work

The VTF experiment is currently being upgraded with new internal coils, capable of supporting higher toroidal current and of better controlling the toroidal asymmetry. In the experiments discussed here, the onset angle varied from discharge to discharge; the variation was not random, probably due to small toroidal asymmetries in the experimental setup. The new coils will improve the symmetry of the setup, as well as support toroidally asymmetric current configurations. The coils will be more robust, and support stronger currents in order to investigate reconnection at other values of q, which were unobtainable in the present configuration. To this end, a plasma gun has been constructed by Arturs Vrublevskis, which will create a seed plasma without the limitations on toroidal magnetic field associated with having electron cyclotron resonance in the vacuum vessel.

Appendix A

Applicability of 2D Calculation of Magnetic Vector Potential

In Section 3.2.2, we described the magnetic arrays, which are used to characterize the reconnection rate and magnetic vector potential in the poloidal cross-section. The measurement of A_φ at one toroidal location is appropriate in the case of 2D symmetry, since then

$$\mathbf{B}_{\mathrm{pol}}(R, Z) = \nabla \times (A_\varphi(R, Z)\mathbf{e}_\varphi) \tag{A.1}$$

and A_φ can be line-integrated using Eq. 3.7. However, Chapters 5-6 showed the presence of 3D effects in the onset of magnetic reconnection. These observations call into question the accuracy of A_φ, which is determined from magnetic measurements at just one toroidal cross-section. In this Appendix, we show that for VTF plasmas, the approximation is valid to within 2%.

To show that the magnetic vector potential A_φ is accurately measured by our magnetic arrays, we follow the argument in Ref. [103]. Consider the general poloidal magnetic field given by

$$\mathbf{B}_{\mathrm{pol}}(R, \varphi, Z) = \nabla \times (A_\varphi \mathbf{e}_\varphi) + \tilde{\mathbf{B}}_{\mathrm{pol}} \tag{A.2}$$

where $\tilde{\mathbf{B}}_{\mathrm{pol}}$ is the part of the poloidal magnetic field that is caused by toroidally asymmetric poloidal currents; it is related to the φ derivatives of A_R and A_Z. We use Eq. A.2 and $\nabla \cdot \mathbf{B} = 0$ to write

$$|\tilde{\mathbf{B}}_{\text{pol}}| \approx |\Delta B_\varphi| \frac{\Delta_{RZ}}{\pi R} \tag{A.3}$$

where ΔB_φ is the characteristic magnitude of toroidal variations in B_φ due to toroidally asymmetric poloidal currents. $\Delta_{RZ} \sim 0.1$ m is the poloidal scale length, and hence, $\Delta_{RZ}/\pi R \sim 0.03$. For VTF reconnection experiments, we observe by direct measurement that $\Delta B_\varphi < 0.1|\mathbf{B}_{\text{pol}}|$, and therefore $|\tilde{\mathbf{B}}_{\text{pol}}| < |\mathbf{B}_{\text{pol}}|/300$. This calculation justifies the neglect of $\tilde{\mathbf{B}}_{\text{pol}}$ in Eq. A.2, which becomes

$$\mathbf{B}_{\text{pol}}(R, \varphi, Z) = \nabla \times (A_\varphi(R, \varphi, Z)\mathbf{e}_\varphi). \tag{A.4}$$

Equation A.3 can also be differentiated with respect to time yielding $|\partial\tilde{\mathbf{B}}_{\text{pol}}/\partial t| \approx |\Delta\partial B_\varphi/\partial t|\Delta_{RZ}/(\pi R)$. We then directly measure $|\Delta\partial B_\varphi/\partial t|$ and find that it is smaller than $\sim 0.1|\partial\mathbf{B}_{\text{pol}}/\partial t|$. This was implied, but not explicitly spelled out in Ref. [103].

To double-check the negligibility of $\tilde{\mathbf{B}}_{\text{pol}}$, and show that the reconnection rate is accurately measured by the magnetic arrays, we compute $\partial A_\varphi/\partial t$ from a simplified model of asymmetric current density.

First, we estimate the error in A_φ due to toroidally asymmetric poloidal currents, which produce magnetic fields $\tilde{\mathbf{B}}_{\text{pol}}$. These magnetic fields are related to the φ derivatives of A_R and A_Z, but they can erroneously contribute to the evaluation of A_φ that uses a magnetic array at 1 toroidal angle. The likeliest source for these poloidal currents is the time-dependent $q = 2$ potential structure. We model a simplified $q = 2$ potential with the log form of Eq. 5.3, shown in Fig. A-1 at different toroidal angles. Superimposed are arrows indicating the ion polarization currents computed from this potential. These currents are toroidally asymmetric and we compute their effect on the measurement of $\partial A_\varphi/\partial t$. We find that the maximum value of erroneous reconnection rate measured from these poloidal currents—assuming a 30 μs growth rate for ϕ—is 0.06 V/m, which is only 0.4% of the 15 V/m typical of the actual reconnection rate due to variation in the toroidal current.

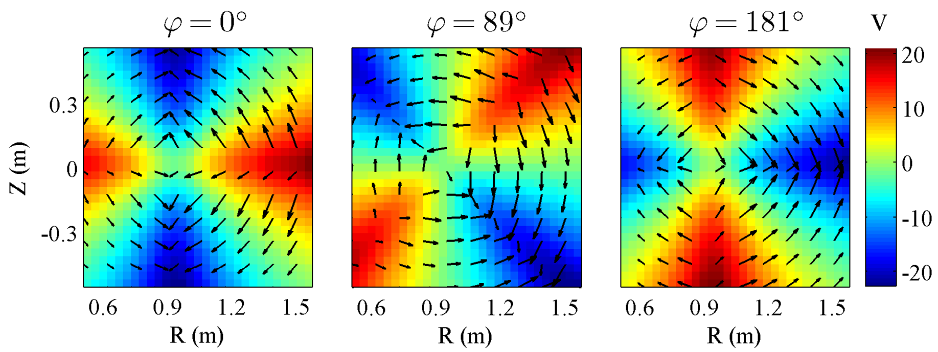

Figure A-1: Simplified potential structure with superimposed ion polarization current arrows. The toroidally asymmetric poloidal currents from this potential are used to estimate the false component of $\partial A_\varphi/\partial t$ measured by the magnetic arrays.

Next, we check the error in the reconnection rate measurement due to toroidal asymmetry in the toroidal current density. We use a simplified model for the toroidal current based on the measured asymmetry in Fig. 6-1c. This toroidal asymmetry is reproduced in Fig. A-2a, and for simplicity the same poloidal profile of J_φ is used at all toroidal angles, with amplitude shown in Fig. A-2b. In (c), we show the reconnection rate evaluated from

$$A_\varphi = \frac{\mu_0}{4\pi}\int \frac{J_\varphi d^3\mathbf{r}'}{|\mathbf{r}' - \mathbf{r}|} \tag{A.5}$$

using information about J_φ everywhere, while in (d), we evaluate the reconnection rate using B_R and B_Z values at only one toroidal cross section. This approximation is within 2% of the 'actual' reconnection rate. In Fig. A-3, we use a different model for the toroidal current density, and find the same small error in the reconnection rate.

These simple estimates and the argument from Ref. [103] confirm the validity of the magnetic measurements for reconnection experiments in VTF.

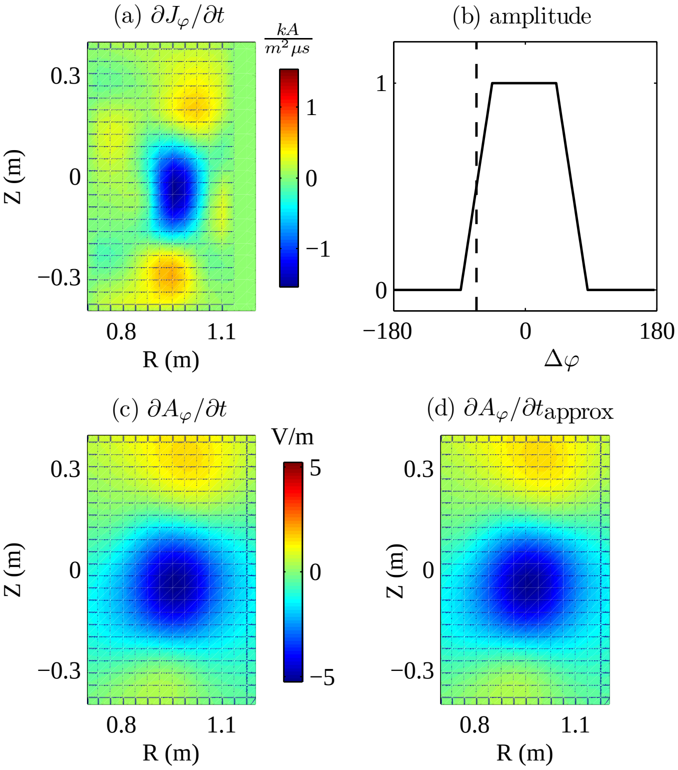

Figure A-2: (a) Asymmetric current at onset location; the 3D asymmetric current is modeled simply with the poloidal structure of (a), but with amplitude (b) which depends on φ. (c) $\partial A_\varphi/\partial t$ computed directly from this model; (d) $\partial A_\varphi/\partial t$ computed as in the experiment only from B_R and B_Z, with a line integral. (c) and (d) are evaluated for the toroidal angle corresponding to the dashed line in (b).

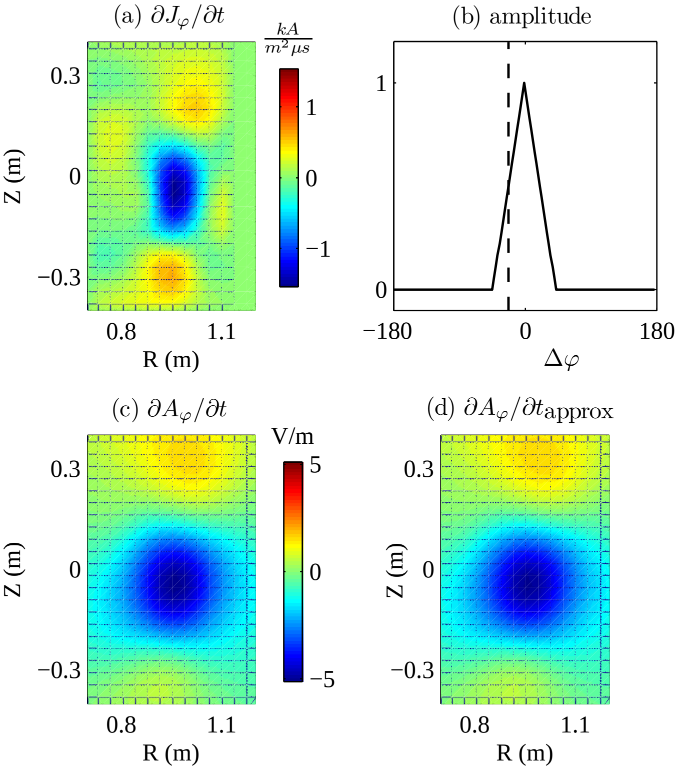

Figure A-3: Alternate model for checking error in reconnection rate: (a) Asymmetric current at onset location; the 3D asymmetric current is modeled simply with the poloidal structure of (a), but with amplitude (b) which depends on φ. (c) $\partial A_\varphi/\partial t$ computed directly from this model; (d) $\partial A_\varphi/\partial t$ computed as in the experiment only from B_R and B_Z, with a line integral. (c) and (d) are evaluated for the toroidal angle corresponding to the dashed line in (b).

Bibliography

[1] J. W. Dungey, “Interplanetary magnetic field and the auroral zones,” *Physical Review Letters*, vol. 6, pp. 47–48, Jan 1961.

[2] M. J. Aschwanden, *Physics of the Solar Corona. An Introduction.* Praxis Publishing Ltd, August 2004.

[3] A. T. Y. Lui, “Current disruption in the earth’s magnetosphere: Observations and models,” *J. Geophys. Res.*, vol. 101, pp. 13067–13088, June 1996.

[4] S. von Goeler, W. Stodiek, and N. Sauthoff, “Studies of internal disruptions and m=1 oscillations in tokamak discharges with soft-x-ray tecniques,” *Physical Review Letters*, vol. 33, pp. 1201–1203, November 1974.

[5] E. Priest and T. Forbes, *Magnetic Reconnection: MHD Theory and Applications.* Cambridge University Press, June 2000.

[6] R. L. Moore, A. C. Sterling, H. S. Hudson, and J. R. Lemen, “Onset of the magnetic explosion in solar flares and coronal mass ejections,” *Astrophys. J.*, vol. 552, pp. 833–848, May 2001.

[7] M. G. Kivelson and C. T. Russell, eds., *Introduction to Space Physics (Cambridge Atmospheric & Space Science Series).* Cambridge University Press, 1st ed., January 1995.

[8] V. Angelopoulos, J. P. McFadden, D. Larson, C. W. Carlson, S. B. Mende, H. Frey, T. Phan, D. G. Sibeck, K. Glassmeier, U. Auster, E. Donovan, I. R. Mann, I. J. Rae, C. T. Russell, A. Runov, X. Zhou, and L. Kepko, “Tail reconnection triggering substorm onset,” *Science*, vol. 321, pp. 931–935, August 2008.

[9] S. Masuda, T. Kosugi, H. Hara, and Y. Ogawaray, “A loop top hard x-reay source i a compact solar-flare as evidence for magnetic reconnection,” *Nature*, vol. 371, pp. 495–497, OCT 6 1994.

[10] J. Heyvaerts, E. R. Priest, and D. M. Rust, “Emerging flux model for solar-flare phenomenon,” *Solar Physics*, vol. 216, no. 1, pp. 123–137, 1977.

[11] L. Li and J. Zhang, “On the brightening propagation of post-flare loops observed by trace,” *The Astrophysical Journal*, vol. 690, no. 1, pp. 347–357, 2009.

[12] C. T. Russell and R. C. Elphic, "Isee observations of flux transfer events at the dayside magnetopause," *Geophysical Research Letters*, vol. 6, no. 1, pp. 33+, 1979.

[13] M. Oieroset, T. Phan, M. Fujimoto, R. P. Lin, and R. P. Lepping, "In situ detection of collisionless reconnection in the earth's magnetotail," *Nature*, vol. 412, pp. 414–417, JUL 26 2001.

[14] M. Oieroset, R. Lin, and T. Phan, "Evidence for electron acceleration up to similar to 300 kev in the magnetic reconnection diffusion region of earth's magnetotail," *Physical Review Letter*, vol. 89, p. 195001, NOV 4 2002.

[15] B. Coppi, G. Laval, and R. Pellat, "Dynamics of the geomagnetic tail," *Physical Review Letter*, vol. 16, pp. 1207–1210, Jun 1966.

[16] T. D. Phan, J. T. Gosling, M. S. Davis, R. M. Skoug, M. Oieroset, R. P. Lin, R. P. Lepping, D. J. McComas, C. W. Smith, H. Reme, and A. Balogh, "A magnetic reconnection x-line extending more than 390 earth radii in the solar wind," *Nature*, vol. 439, pp. 175–178, January 2006.

[17] B. B. Kadomtsev, "Disruptive instability in tokamaks," *Soviet Journal of Plasma Physics*, vol. 1, no. 5, pp. 389–391, 1975.

[18] J. Wesson, *Tokamaks (International Series of Monographs on Physics)*. Oxford University Press, USA, 3rd ed., January 2004.

[19] R. G. Watt and R. A. Nebel, "Sawteeth, magnetic disturbances, and magnetic flux regeneration in the reversed-field pinch," *Physics of Fluids*, vol. 26, no. 5, pp. 1168–1170, 1983.

[20] C. K. Li, F. H. Séguin, J. A. Frenje, J. R. Rygg, R. D. Petrasso, R. P. J. Town, O. L. Landen, J. P. Knauer, and V. A. Smalyuk, "Observation of megagauss-field topology changes due to magnetic reconnection in laser-produced plasmas," *Physical Review Letters*, vol. 99, pp. 055001+, Aug 2007.

[21] T. R. Jarboe, "Review of spheromak research," *Plasma Physics and Controlled Fusion*, vol. 36, no. 6, p. 945, 1994.

[22] C. Thompson, M. Lyutikov, and S. R. Kulkarni, "Electrodynamics of magnetars: Implications for the persistent x-ray emission and spin-down of the soft gamma repeaters and anomalous x-ray pulsars," *The Astrophysical Journal*, vol. 574, no. 1, p. 332, 2002.

[23] M. B. Niedner and J. C. Brandt, "Interplanetary gas. xxii - plasma tail disconnection events in comets - evidence for magnetic field line reconnection at interplanetary sector boundaries," *Astrophys. J.*, vol. 223, pp. 655–670, July 1978.

[24] D. J. Griffiths, *Introduction to Electrodynamics*. Benjamin Cummings, 3rd ed., January 1999.

[25] P. A. Sweet, "The neutral point theory of solar flares," in *Electromagnetic Phenomena in Cosmical Physics* (B. Lehnert, ed.), vol. 6 of *IAU Symposium*, 1958.

[26] E. N. Parker, "Sweet's mechanism for merging magnetic fields in conducting fluids," *Journal of Geophysical Research*, vol. 62, no. 4, pp. 509–520, 1957.

[27] J. D. Huba, U. States., and N. R. L. (U.S.), *NRL plasma formulary*. Naval Research Laboratory, Washington, DC, 2009.

[28] R. G. Kleva, J. F. Drake, and F. L. Waelbroeck, "Fast reconnection in high temperature plasmas," *Physics of Plasmas*, vol. 2, pp. 23–34, January 1995.

[29] A. Le, J. Egedal, W. Daughton, J. F. Drake, W. Fox, and N. Katz, "Magnitude of the hall fields during magnetic reconnection," *Geophysical Research Letters*, vol. 37, pp. L03106+, February 2010.

[30] D. A. Uzdensky and R. M. Kulsrud, "Physical origin of the quadrupole out-of-plane magnetic field in hall-magnetohydrodynamic reconnection," *Physics of Plasmas*, vol. 13, no. 6, pp. 062305+, 2006.

[31] M. A. Shay, J. F. Drake, B. N. Rogers, and R. E. Denton, "Alfvénic collisionless magnetic reconnection and the hall term," *Journal of Geophysical Research*, vol. 106, no. A3, pp. 3759+, 2001.

[32] A. Vaivads, Y. Khotyaintsev, M. André, A. Retinò, S. C. Buchert, B. N. Rogers, P. Décréau, G. Paschmann, and T. D. Phan, "Structure of the magnetic reconnection diffusion region from four-spacecraft observations," *Physical Review Letters*, vol. 93, August 2004.

[33] Y. Ren, M. Yamada, S. Gerhardt, H. Ji, R. Kulsrud, and A. Kuritsyn, "Experimental verification of the hall effect during magnetic reconnection in a laboratory plasma," *Physical Review Letters*, vol. 95, pp. 055003+, July 2005.

[34] M. R. Brown, C. D. Cothran, and J. Fung, "Two fluid effects on three-dimensional reconnection in the swarthmore spheromak experiment with comparisons to space data," *Physics of Plasmas*, vol. 13, no. 5, pp. 056503+, 2006.

[35] J. Birn, J. F. Drake, M. A. Shay, B. N. Rogers, R. E. Denton, M. Hesse, M. Kuznetsova, Z. W. Ma, A. Bhattacharjee, A. Otto, and P. L. Pritchett, "Geospace environmental modeling (GEM) magnetic reconnection challenge," *Journal of Geophysical Research - Space Physics*, vol. 106, pp. 3715–3719, March 2001.

[36] A. Y. Aydemir, "Nonlinear studies of m=1 modes in high-temperature plasmas," *Physics of Fluids B: Plasma Physics*, vol. 4, no. 11, pp. 3469–3472, 1992.

[37] A. Le, J. Egedal, W. Fox, N. Katz, A. Vrublevskis, W. Daughton, and J. F. Drake, "Equations of state in collisionless magnetic reconnection," *Physics of Plasmas*, vol. 17, no. 5, pp. 055703+, 2010.

[38] P. Ricci, J. U. Brackbill, W. Daughton, and G. Lapenta, "Collisionless magnetic reconnection in the presence of a guide field," *Physics of Plasmas*, vol. 11, no. 8, pp. 4102–4114, 2004.

[39] J. Egedal, M. Øieroset, W. Fox, and R. P. Lin, "In situ discovery of an electrostatic potential, trapping electrons and mediating fast reconnection in the earth's magnetotail," *Physical Review Letters*, vol. 94, pp. 025006+, Jan 2005.

[40] J. Egedal, W. Fox, N. Katz, M. Porkolab, M. Øieroset, R. P. Lin, W. Daughton, and J. F. Drake, "Evidence and theory for trapped electrons in guide field magnetotail reconnection," *Journal of Geophysical Research*, vol. 113, December 2008.

[41] J. Egedal, W. Daughton, J. F. Drake, N. Katz, and A. Lê, "Formation of a localized acceleration potential during magnetic reconnection with a guide field," *Physics of Plasmas*, vol. 16, no. 5, pp. 050701+, 2009.

[42] A. Le, J. Egedal, W. Daughton, W. Fox, and N. Katz, "Equations of state for collisionless guide-field reconnection," *Physical Review Letters*, vol. 102, February 2009.

[43] G. F. Chew, M. L. Goldberger, and F. E. Low, "The boltzmann equation and the one-fluid hydromagnetic equations in the absence of particle collisions," *Royal Society of London Proceedings Series A*, vol. 236, pp. 112–118, July 1956.

[44] W. Daughton, J. Scudder, and H. Karimabadi, "Fully kinetic simulations of undriven magnetic reconnection with open boundary conditions," *Physics of Plasmas*, vol. 13, no. 7, pp. 072101+, 2006.

[45] F. L. Waelbroeck, "Onset of the sawtooth crash," *Phys. Rev. Lett.*, vol. 70, pp. 3259–3262, May 1993.

[46] X. Wang and A. Bhattacharjee, "Nonlinear dynamics of the m=1 instability and fast sawtooth collapse in high-temperature plasmas," *Phys. Rev. Lett.*, vol. 70, no. 11, pp. 1627–1630, 1993.

[47] A. J. Lichtenberg, K. Itoh, S. I. Itoh, and A. Fukuyama, "The role of stochasticity in sawtooth oscillations," *Nuclear Fusion*, vol. 32, no. 3, pp. 495–512, 1992.

[48] V. Igochine, O. Dumbrajs, H. Zohm, A. Flaws, and t. A. U. Team, "Stochastic sawtooth reconnection in asdex upgrade," *Nuclear Fusion*, vol. 47, pp. 23–32, January 2007.

[49] V. Igochine, O. Dumbrajs, H. Zohm, and the ASDEX Upgrade Team, "Transition from quasiperiodicity to chaos just before sawtooth crash in the asdex upgrade tokamak," *Nuclear Fusion*, vol. 48, pp. 062001+, June 2008.

[50] J. A. Wesson, B. Alper, A. W. Edwards, and R. D. Gill, "Transport in the sawtooth collapse," *Physical Review Letters*, vol. 79, pp. 5018–5021, Dec 1997.

[51] S. Choi, D. Craig, F. Ebrahimi, and S. C. Prager, "Cause of sudden magnetic reconnection in a laboratory plasma," *Physical Review Letters*, vol. 96, no. 14, p. 145004, 2006.

[52] P. L. Pritchett, "Onset and saturation of guide-field magnetic reconnection," *Physics of Plasmas*, vol. 12, no. 6, p. 062301, 2005.

[53] P. Ricci, J. U. Brackbill, W. Daughton, and G. Lapenta, "Influence of the lower hybrid drift instability on the onset of magnetic reconnection," *Physics of Plasmas*, vol. 11, no. 9, pp. 4489–4500, 2004.

[54] M. Scholer, I. Sidorenko, C. H. Jaroschek, R. A. Treumann, and A. Zeiler, "Onset of collisionless magnetic reconnection in thin current sheets: Three-dimensional particle simulations," *Physics of Plasmas*, vol. 10, no. 9, pp. 3521–3527, 2003.

[55] H. Karimabadi, W. Daughton, and K. B. Quest, "Role of electron temperature anisotropy in the onset of magnetic reconnection," *Geophysical Research Letters*, vol. 31, pp. L18801+, September 2004.

[56] P. A. Cassak, M. A. Shay, and J. F. Drake, "Catastrophe model for fast magnetic reconnection onset," *Phys. Rev. Lett.*, vol. 95, no. 23, p. 235002, 2005.

[57] P. A. Cassak, J. F. Drake, and M. A. Shay, "Catastrophic onset of fast magnetic reconnection with a guide field," *Physics of Plasmas*, vol. 14, May 2007.

[58] P. A. Cassak, J. F. Drake, M. A. Shay, and B. Eckhardt, "Onset of fast magnetic reconnection," *Physical Review Letters*, vol. 98, pp. 215001+, May 2007.

[59] P. F. Chen and K. Shibata, "An emerging flux trigger mechanism for coronal mass ejections," *The Astrophysical Journal*, vol. 545, no. 1, pp. 524–531, 2000.

[60] E. E. Lawrence and W. Gekelman, "Identification of a quasiseparatrix layer in a reconnecting laboratory magnetoplasma," *Physical Review Letters*, vol. 103, no. 10, p. 105002, 2009.

[61] S. Servidio, W. H. Matthaeus, M. A. Shay, P. A. Cassak, and P. Dmitruk, "Magnetic reconnection in two-dimensional magnetohydrodynamic turbulence," *Physical Review Letters*, vol. 102, pp. 115003+, Mar 2009.

[62] A. Retino, D. Sundkvist, A. Vaivads, F. Mozer, M. Andre, and C. J. Owen, "In situ evidence of magnetic reconnection in turbulent plasma," *Nature Physics*, vol. 3, pp. 236–238, March 2007.

[63] A. Lazarian and E. T. Vishniac, “Reconnection in a weakly stochastic field,” *Astrophys. J.*, vol. 517, pp. 700–718, June 1999.

[64] H. K. Park, Jr, A. J. H. Donné, I. G. J. Classen, C. W. Domier, E. Mazzucato, T. Munsat, M. J. van de Pol, and Xia, “Observation of high-field-side crash and heat transfer during sawtooth oscillation in magnetically confined plasmas,” *Physical Review Letters*, vol. 96, no. 19, p. 195003, 2006.

[65] H. K. Park, E. Mazzucato, Jr, C. W. Domier, Z. Xia, T. Munsat, A. J. H. Donné, I. G. J. Classen, M. J. van de Pol, and T. Team, “Self-organized t[sub e] redistribution during driven reconnection processes in high-temperature plasmas,” *Physics of Plasmas*, vol. 13, no. 5, p. 055907, 2006.

[66] T. Munsat, H. K. Park, I. G. J. Classen, C. W. Domier, A. J. H. Donne, N. C. Luhmann, E. Mazzucato, M. J. van de Pol, and the TEXTOR team, “Localization of the magnetic reconnection zone during sawtooth crashes in tokamak plasmas,” *Nuclear Fusion*, vol. 47, no. 11, pp. L31–L35, 2007.

[67] H. K. Park, A. J. H. Donné, Jr, I. G. J. Classen, C. W. Domier, E. Mazzucato, T. Munsat, M. J. van de Pol, and Xia, “Comparison study of 2d images of temperature fluctuations during sawtooth oscillation with theoretical models,” *Physical Review Letters*, vol. 96, no. 19, p. 195004, 2006.

[68] J. F. Drake, M. Swisdak, C. Cattell, M. A. Shay, B. N. Rogers, and A. Zeiler, “Formation of electron holes and particle energization during magnetic reconnection,” *Science*, vol. 299, pp. 873–877, February 2003.

[69] W. Daughton. private communication, 2009.

[70] P. Demoulin, L. G. Bagala, C. H. Mandrini, J. C. Henoux, and M. G. Rovira, “Quasi-separatrix layers in solar flares. II. Observed magnetic configurations.,” *aap*, vol. 325, pp. 305–317, September 1997.

[71] D. Tripathi, H. Isobe, and H. E. Mason, “On the propagation of brightening after filament/prominence eruptions, as seen by soho-eit,” *Astronomy and Astrophysics*, vol. 453, pp. 1111–1116, July 2006.

[72] F. Heitsch and E. G. Zweibel, “Fast reconnection in a two-stage process,” *The Astrophysical Journal*, vol. 583, pp. 229+, January 2003.

[73] N. Katz, J. Egedal, W. Fox, A. Le, and M. Porkolab, “Experiments on the propagation of plasma filaments,” *Physical Review Letters*, vol. 101, no. 1, p. 015003, 2008.

[74] S. Krasheninnikov, “On scrape off layer plasma transport,” *Physics Letters A*, vol. 283, pp. 368–370, May 2001.

[75] K. Otsuji, K. Shibata, R. Kitai, S. Ueno, S. Nagata, T. Matsumoto, T. Nakamura, H. Watanabe, S. Tsuneta, Y. Suematsu, K. Ichimoto, T. Shimizu, Y. Katsukawa, T. D. Tarbell, B. Lites, R. A. Shine, and Title Alan M., "Small-scale magnetic-flux emergence observed with hinode solar optical telescope," *Pub. Astron. Soc. Japan*, vol. 59, November 2007.

[76] A. A. Pimenta, Y. Sahai, J. A. Bittencourt, and F. J. Rich, "Ionospheric plasma blobs observed by oi 630 nm all-sky imaging in the brazilian tropical sector during the major geomagnetic storm of april 67, 2000," *Geophysical Research Letters*, vol. 34, pp. L02820+, January 2007.

[77] J. Park, K. W. Min, J.-J. Lee, H. Kil, V. P. Kim, H.-J. Kim, E. Lee, and D. Y. Lee, "Plasma blob events observed by kompsat-1 and dmsp f15 in the low latitude nighttime upper ionosphere," *Geophysical Research Letters*, vol. 30, pp. 2114+, November 2003.

[78] G. Le, C. S. Huang, R. F. Pfaff, S. Y. Su, H. C. Yeh, R. A. Heelis, F. J. Rich, and M. Hairston, "Plasma density enhancements associated with equatorial spread f: Rocsat-1 and dmsp observations," *Journal of Geophysical Research*, vol. 108, pp. 1318+, August 2003.

[79] J. A. Boedo, D. L. Rudakov, R. A. Moyer, G. R. McKee, R. J. Colchin, M. J. Schaffer, P. G. Stangeby, W. P. West, S. L. Allen, T. E. Evans, R. J. Fonck, E. M. Hollmann, S. Krasheninnikov, A. W. Leonard, W. Nevins, M. A. Mahdavi, G. D. Porter, G. R. Tynan, D. G. Whyte, and X. Xu, "Transport by intermittency in the boundary of the diii-d tokamak," *Physics of Plasmas*, vol. 10, no. 5, pp. 1670–1677, 2003.

[80] J. L. Terry, S. J. Zweben, K. Hallatschek, B. LaBombard, R. J. Maqueda, B. Bai, C. J. Boswell, M. Greenwald, D. Kopon, W. M. Nevins, C. S. Pitcher, B. N. Rogers, D. P. Stotler, and X. Q. Xu, "Observations of the turbulence in the scrape-off-layer of alcator c-mod and comparisons with simulation," *Physics of Plasmas*, vol. 10, no. 5, pp. 1739–1747, 2003.

[81] A. H. Nielsen, H. L. Pécseli, and J. J. Rasmussen, "Turbulent transport in low-beta plasmas," *Physics of Plasmas*, vol. 3, no. 5, pp. 1530–1544, 1996.

[82] T. A. Carter, "Intermittent turbulence and turbulent structures in a linear magnetized plasma," *Physics of Plasmas*, vol. 13, no. 1, pp. 010701+, 2006.

[83] S. J. Zweben, J. A. Boedo, O. Grulke, C. Hidalgo, B. LaBombard, R. J. Maqueda, P. Scarin, and J. L. Terry, "Edge turbulence measurements in toroidal fusion devices," *Plasma Physics and Controlled Fusion*, vol. 49, pp. S1+, July 2007.

[84] B. LaBombard, M. V. Umansky, R. L. Boivin, J. A. Goetz, J. Hughes, B. Lipschultz, D. Mossessian, C. S. Pitcher, J. L. Terry, and A. Group, "Cross-field

plasma transport and main-chamber recycling in diverted plasmas on alcator c-mod," *Nuclear Fusion*, vol. 40, pp. 2041+, December 2000.

[85] S. J. Zweben, D. P. Stotler, J. L. Terry, B. LaBombard, M. Greenwald, M. Muterspaugh, C. S. P. A. C. M. Group, K. Hallatschek, R. J. Maqueda, B. Rogers, J. L. Lowrance, V. J. Mastrocola, and G. F. Renda, "Edge turbulence imaging in the alcator c-mod tokamak," *Physics of Plasma*, vol. 9, no. 5, pp. 1981–1989, 2002.

[86] J. R. Myra and D. A. D'Ippolito, "Edge instability regimes with applications to blob transport and the quasicoherent mode," *Physics of Plasmas*, vol. 12, no. 9, pp. 092511+, 2005.

[87] O. E. Garcia, N. H. Bian, V. Naulin, A. H. Nielsen, and J. J. Rasmussen, "Mechanism and scaling for convection of isolated structures in nonuniformly magnetized plasmas," *Physics of Plasmas*, vol. 12, no. 9, pp. 090701+, 2005.

[88] R. J. D'Arcy, "Dielectric impurities and surface instability in langmuir probe plasma measurements," *Journal of Physics D: Applied Physics*, vol. 7, no. 10, pp. 1391–1401, 1974.

[89] W. E. Amatucci, P. W. Schuck, D. N. Walker, P. M. Kintner, S. Powell, B. Holback, and D. Leonhardt, "Contamination-free sounding rocket langmuir probe," *Review of Scientific Instruments*, vol. 72, no. 4, pp. 2052–2057, 2001.

[90] J. E. Allen, R. L. F. Boyd, and P. Reynolds, "The collection of positive ions by a probe immersed in a plasma," *Proceedings of the Physical Society. Section B*, vol. 70, pp. 297+, March 1957.

[91] G. Q. Yu, S. I. Krasheninnikov, and P. N. Guzdar, "Two-dimensional modelling of blob dynamics in tokamak edge plasmas," *Physics of Plasmas*, vol. 13, no. 4, pp. 042508+, 2006.

[92] D. A. D'Ippolito, J. R. Myra, and S. I. Krasheninnikov, "Cross-field blob transport in tokamak scrape-off-layer plasmas," *Physics of Plasmas*, vol. 9, no. 1, pp. 222–233, 2002.

[93] A. V. Phelps, "Cross sections and swarm coefficients for nitrogen ions and neutrals in n_2 and argon ions and neutrals in ar for energies from 0.1 ev to 10 kev," *Journal of Physical and Chemical Reference Data*, vol. 20, no. 3, pp. 557–573, 1991.

[94] P. Banks, "Collision frequencies and energy transfer ions," *Planetary and Space Science*, vol. 14, pp. 1105–1122, November 1966.

[95] J. E. Leake and T. D. Arber, "The emergence of magnetic flux through a partially ionised solar atmosphere," *Astronomy and Astrophysics*, vol. 450, no. 2, pp. 805–818, 2006.

[96] H. S. Ji, M. T. Song, and G. L. Huang, "Exact solutions for two-dimensional steady state magnetic reconnection in partially ionized plasmas," *The Astrophysical Journal*, vol. 548, no. 2, p. 1087, 2001.

[97] E. G. Zweibel and A. Brandenburg, "Current sheet formation in the interstellar medium," *The Astrophysical Journal*, vol. 478, pp. 563+, April 1997.

[98] Y. E. Litvinenko and J. Chae, "Signatures of sweet-parker magnetic reconnection in the solar chromosphere," *Astron. Astrophys.*, vol. 495, pp. 953–957, March 2009.

[99] E. G. Zweibel, "Magnetic reconnection in partially ionized gases," *Astrophys. J.*, vol. 340, pp. 550–557, May 1989.

[100] J. Egedal, A. Fasoli, D. Tarkowski, and A. Scarabosio, "Collisionless magnetic reconnection in a toroidal cusp," *Physics of Plasmas*, vol. 8, no. 5, pp. 1935–1943, 2001.

[101] J. Egedal, W. Fox, N. Katz, M. Porkolab, K. Reim, and E. Zhang, "Laboratory observations of spontaneous magnetic reconnection," *Physical Review Letters*, vol. 98, no. 1, p. 015003, 2007.

[102] W. Fox, *Experimental Study of Current-Driven Turbulence During Magnetic Reconnection.* PhD dissertation, MIT, Department of Physics, June 2009.

[103] A. Kesich, J. Bonde, J. Egedal, W. Fox, R. Goodwin, N. Katz, and A. Le, "Magnetic flux array for spontaneous magnetic reconnection experiments," *Review of Scientific Instruments*, vol. 79, no. 6, p. 063505, 2008.

[104] I. H. Hutchinson, *Principles of Plasma Diagnostics.* Cambridge University Press, 2nd ed., July 2005.

[105] H. F. Dylla, "Glow discharge techniques for conditioning high-vacuum systems," *Journal of Vacuum Science & Technology A: Vacuum, Surfaces, and Films*, vol. 6, no. 3, pp. 1276–1287, 1988.

[106] M. Mitchner and C. H. Kruger, *Partially Ionized Gases (Wiley series in plasma physics).* John Wiley & Sons Inc, 1973.

[107] L. Spitzer, *Physics of Fully Ionized Gases.* Interscience, 2nd ed., 1962.

[108] A. Kuritsyn, M. Yamada, S. Gerhardt, H. Ji, R. Kulsrud, and Y. Ren, "Measurements of the parallel and transverse spitzer resistivities during collisional magnetic reconnection," *Physics of Plasmas*, vol. 13, no. 5, pp. 055703+, 2006.

[109] S. K. Srivastava, H. Tanaka, A. Chutjian, and S. Trajmar, "Elastic scattering of intermediate-energy electrons by ar and kr," *Physical Review A*, vol. 23, pp. 2156–2166, May 1981.

[110] A. Dasgupta and A. K. Bhatia, "Scattering of electrons from argon atoms," *Physical Review A*, vol. 32, pp. 3335–3343, Dec 1985.

[111] D. R. Lide, ed., *CRC Handbook of Chemistry and Physics*. CRC Press, 90th ed., 2002.

[112] W. Fox, M. Porkolab, J. Egedal, N. Katz, and A. Le, "Laboratory observations of electron energization and associated lower-hybrid and trivelpiece-gould wave turbulence during magnetic reconnection," *Accepted by Physics of Plasmas*, 2010.

[113] N. Katz, J. Egedal, W. Fox, A. Le, J. Bonde, and A. Vrublevskis, "Laboratory observation of localized onset of magnetic reconnection," *Accepted by Physical Review Letters*, 2010.

[114] J. Egedal, W. Fox, M. Porkolab, and A. Fasoli, "Eigenmode response to driven magnetic reconnection in a collisionless plasma," *Physics of Plasmas*, vol. 12, no. 5, p. 052107, 2005.

[115] J. Egedal, W. Fox, M. Porkolab, and A. Fasoli, "Experimental evidence of fast reconnection via trapped electron motion," *Physics of Plasmas*, vol. 11, no. 5, pp. 2844–2851, 2004.

[116] J. Egedal, A. Fasoli, and J. Nazemi, "Dynamical plasma response during driven magnetic reconnection," *Physical Review Letters*, vol. 90, p. 135003, Apr 2003.

[117] J. A. Wesson, "Sawtooth oscillations," *Plasma Physics and Controlled Fusion*, vol. 28, no. 1A, pp. 243–248, 1986.

[118] Y. Hamada, A. Nishizawa, Y. Kawasumi, K. Kawahata, K. Itoh, A. Ejiri, K. Toi, K. Narihara, K. Sato, T. Seki, H. Iguchi, A. Fujisawa, K. Adachi, S. Hidekuma, S. Hirokura, K. Ida, M. Kojima, J. Koong, R. Kumazawa, H. Kuramoto, R. Liang, T. Minami, H. Sakakita, M. Sasao, K. N. Sato, T. Tsuzuki, J. Xu, I. Yamada, and T. Watari, "Fast potential change during sawteeth in JIPP T-IIU tokamak plasmas," *Nuclear Fusion*, vol. 36, no. 4, pp. 515–520, 1996.

[119] R. J. Hastie, "Sawtooth instability in tokamak plasmas," *Astrophysics and Space Science*, vol. 256, no. 1-2, pp. 177–204, 1998.